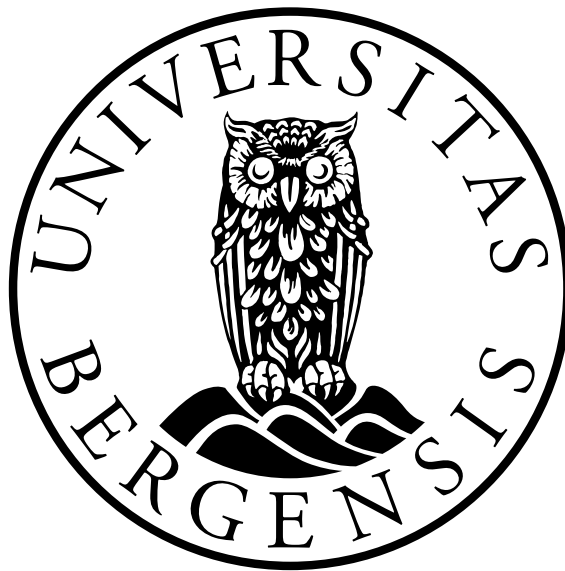# Airborne field measurements and model simulations of boundary layer properties over the Iceland Sea

Heidi Midtgarden Golid

Master's thesis in Meteorology

University of Bergen
Geophysical Institute

June 2019

Abstract

The spatial and temporal distributions of a cold air outbreak (CAO) event over the Iceland- and southern Greenland Seas have been investigated during the Iceland-Greenland Seas project (IGP) in February and March 2018. This area is arguably the least studied region of the North Atlantic sub-polar seas, and several observing platforms were therefore utilized in investigating the critical processes in the region. The focus of this study is on increasing the understanding of how the thermodynamic properties within the atmospheric boundary layer develop during a CAO. This is done by analysing observational data from a research aircraft and radiosondes. A distinct boundary layer deepening was observed over the marginal ice zone (MIZ), in the off-ice direction, as the ocean transferred large amounts of heat and moisture to the atmosphere.

In addition to providing in-situ measurements over the Iceland-Greenland Seas, the observational data are compared to the high-resolution regional $COSMO_{iso}$ model in order to determine an optimal model setup for accurate simulations of the atmospheric water cycle. The accuracies of the model forecasts appeared to increase with decreasing lead time and finer resolution. A simulation with relatively long spin-up time included large biases of surface temperature and humidity due to the development of an instability in the study area. These errors are reduced for the simulations with shorter spin-up time, at which a combination of fine resolution and 9–18 hours spin-up time is deemed optimal.

Contents

1 Introduction

Cold air outbreaks (CAOs) are characteristic weather phenomena at high latitudes, and they are of high interest and relevance due to their rapid impact on air-sea interactions and the atmospheric boundary layer (Brümmer, 1996). Considerable amounts of heat and moisture are transferred from the ocean to the atmosphere during CAOs, making them significant in Arctic climate studies. Additionally, strong Arctic CAOs can extend more than 1000 km southwards and may even influence the weather in northern Europe (Wacker et al., 2005).
The Iceland-Greenland Seas project (IGP) took place in February and March 2018, focusing on a moderate CAO event in the region of the densest waters of the Atlantic Meridional Overturning Circulation (Renfrew et al., 2019). The campaign was executed over the Iceland- and southern Greenland Seas (Fig. 1.1), and was a coordinated atmosphere-ocean experiment. A long-lasting CAO was present during the campaign, giving rise to a continuous convection in the atmospheric boundary layer over the ocean. Since CAOs are often associated with rapid modifications in various boundary layer properties, their effects are difficult to predict. The primary objective of this study is therefore to obtain a better understanding of CAOs and their effects over the Iceland Sea by means of frequent aircraft- and radiosonde measurements in a relatively unexplored area. Subsequently, this research will contribute to improve future model simulations and enhance predictability in the sub-arctic seas.

As large amounts of heat and moisture are transferred from the ocean to the atmosphere, convection is induced and the atmospheric boundary layer is believed to get warmer, deeper and more humid in the downwind direction. In most CAO events, the convection is typically organized into rolls accompanied with cloud streets stretching several hundred km downstream of the ice edge (e.g. Hartmann et al. (1997), Renfrew and Moore (1999) and Wacker et al. (2005)). Note that these convective cloud processes will not be emphasized in this study due to lack of observational data within the clouds.

Furthermore, the retrieved observational data from the IGP campaign are applied to a larger study on the characterization of the atmospheric water cycle. For this investigation, the high-resolution regional COSMO$_{iso}$ model (Steppeler et al., 2003) is applied over the study area for the purpose of simulating accurate isotope ratios in precipitation and water vapour. Accordingly, the second aim of this study is to find a setup of the COSMO model that complies with the aircraft- and radiosonde observations, so that high-resolution stable isotope simulations can be made. The following objective is to compare various model simulations with measurements from aircraft and radiosondes, noting how the different lead times and grid spacings influence the sensitivity of the bulk properties. A long spin-up time is primarily believed to be advantageous since the model has time to adapt to the initial conditions and to detect more detailed structures. It is also worth considering that an excessive spin-up time may reinforce potential erroneous initial conditions, which can result in the development of various severe weather systems.
Finding an optimal model setup for a CAO situation is quite challenging as several characteristic processes, such as moist convection and cloud microphysics, are parametrised in the COSMO$_{iso}$ model (Pfahl et al., 2012). The available observations are also limited both temporally and spatially.
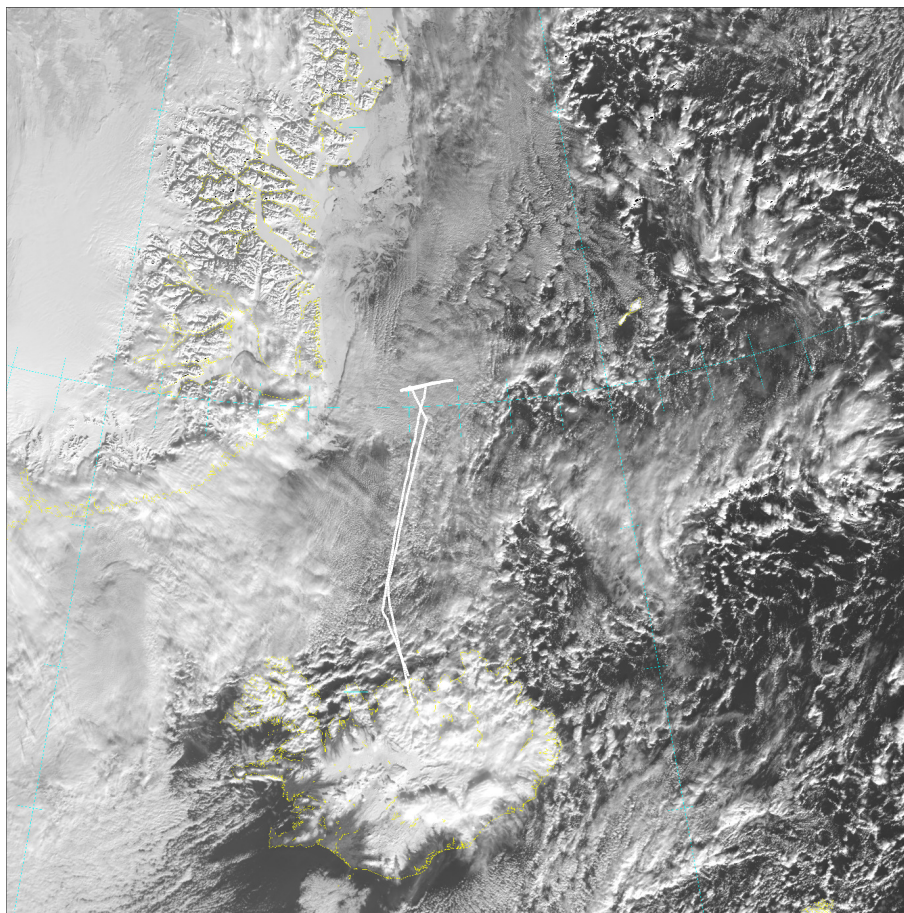
Figure 1.1: Visible Infrared Imaging Radiometer Suite (VIIRS) satellite image from the Dundee satellite (visible: 0.67 µm) from 4 March 2018, 11:37 UTC over Iceland and the Iceland Sea. The flight pattern of flight 295 is sketched in white.

Some background and results from previous similar field experiments are introduced in Section 2. An outline of the IGP campaign is then given together with the weather situation during the analysis period (4–9 March) in Section 3. Section 4 includes the applied method and a brief description of the simulation set-up. The results are then presented and discussed in Section 5, and finally, a summary of the major findings is presented in Section 6.

2   Background

2.1   The Iceland-Greenland Seas

The Iceland-Greenland Seas lies north of Iceland on the eastern side of Greenland. This region is crucial for the global climate system since it is associated with the sinking branch of the Atlantic Meridional Overturning Circulation, driven by strong air-sea buoyancy fluxes (Buckley and Marshall, 2015). The ocean and atmosphere are constantly interacting, and considerably large amounts of various thermodynamic bulk properties are transferred from the ocean to the atmosphere. Despite such essential interactions, few measurements have previously been obtained over the domain. Renfrew et al. (2019) state that the Iceland-Greenland Seas arguably are the least studied region of the North Atlantic's sub-polar seas, which makes the IGP campaign significantly more relevant.

Climate models are observed to have the largest mean surface temperature errors along the marginal ice zone (MIZ) near the coast of Greenland (Davy and Esau, 2014). This large departure from observations is mainly related to the lack of observations in the area, and poor representation of the sea-ice extent, which affects the heat fluxes and thus the surface air temperatures (Fig. 2.1). Additionally, the boundary layer over the Greenland MIZ tends to be substantially shallower than over the ocean. This contributes to enlarged errors in surface air temperature (SAT) variability since temperatures are most sensitive to forcing within shallow boundary layers. An area of considerably large errors in SAT variability is observed in the Iceland Sea just north of Iceland (Fig. 2.1c).
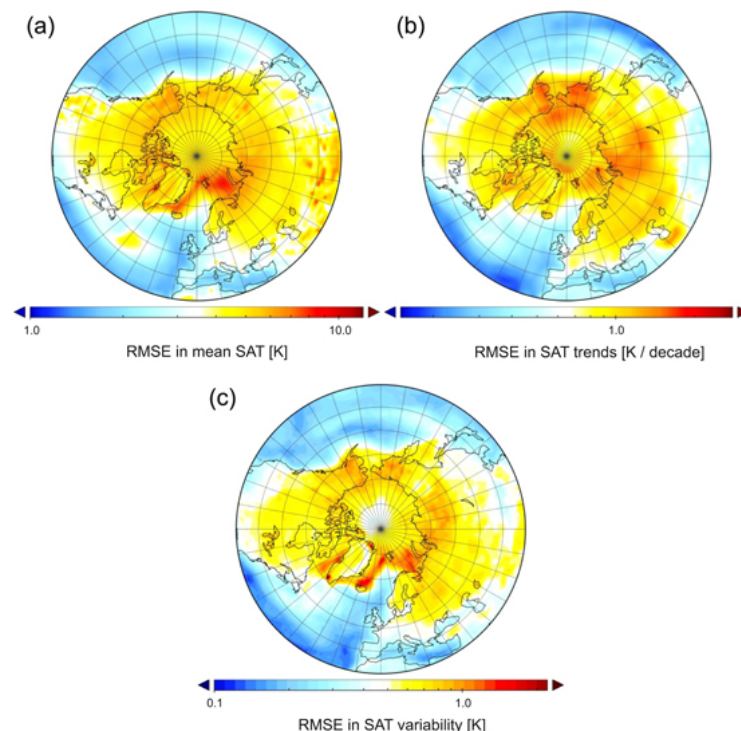

Figure 2.1: Geospatial root mean square error (RMSE) in a) mean, b) trend and c) variability of the surface air temperature (SAT) for the 36-member-ensemble of the CMIP5 model. The errors represent the degree to which the models exhibit the climatological mean (from Davy and Esau (2014)).

The simulated surface temperatures at high latitudes are generally quite erroneous compared to the extra-tropics and subtropics, especially in the northern seas. The largest errors are found along the east coast of Greenland and in the western Barents Sea (Fig. 2.1a). Such areas are generally characterized by intense intermittent heat fluxes, and are therefore particularly susceptible to a peculiar weather phenomenon that may abruptly change the boundary layer properties, namely cold air outbreaks.

2.2 Cold air outbreaks

The term "cold air outbreak" is commonly used to describe a large scale departure of cold air masses over a relatively warm surface, a phenomenon that typically occurs near polar caps or ice-covered continents during wintertime. Due to relatively high sea surface temperatures in the North Atlantic, CAOs are about 70% more common during Northern Hemisphere winter than Southern Hemisphere winter (Fletcher et al., 2016). Additionally, intense surface heat fluxes are typically associated with these outbreaks, which makes the frequent occurrence of CAOs during wintertime of large climatological relevance (Brümmer, 1996). A typical index used for identifying CAOs is the vertical potential temperature gradient between sea level (skin temperature, SKT) and 700/800 hPa; $\theta_{\mathrm{SKT}} - \theta$ (Kolstad et al., 2009; Fletcher et al., 2016). This index is in many studies not imposed as a threshold, but it is required to be positive. Papritz and Spengler (2017) state that strong CAOs ($12 < \theta_{\mathrm{SKT}} - \theta$) typically occur over the Fram Strait and the western Barents Sea (Fig. 2.2d). As a consequence, most CAO studies are being conducted in these areas.
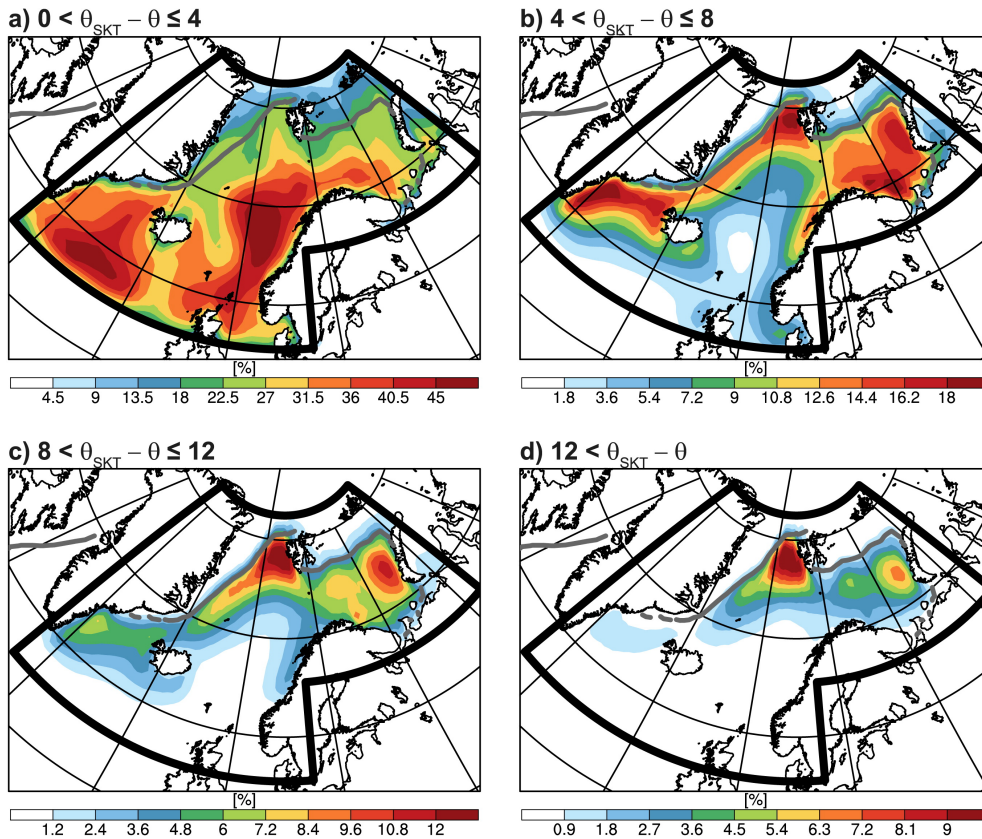

Figure 2.2: Mean frequencies of CAOs, categorized by intensity. The mean sea ice boundary (50% sea ice concentration) is shown by the gray contour (from Papritz and Spengler (2017)).

The process of cold and dry air flowing from cold continents or sea ice over a relatively warmer ocean surface immediately results in large amounts of heat being transferred from the ocean to the atmosphere. Consequently, a convective boundary layer develops, playing an important role in various mesoscale weather systems in the North Atlantic area.

Cold air outbreaks also contribute significantly to the energy exchange between ocean and atmosphere with sensible heat fluxes of several hundreds Wm^{-2}, compared with the climatological heat flux of 15 Wm^{-2} (averaged over the entire ocean surface on Earth (Brümmer et al., 1992)). The largest sensible heat fluxes are found in the Greenland Sea and the Barents Sea, with average fluxes of more than 50 Wm^{-2} according to Budyko (1961) and Brümmer et al. (1992). The strong heat fluxes in these areas lead to continuously warmed and moistened air masses as they flow over the ocean. Consequently, they are convected upwards, contributing to a well-mixed and increasingly deep boundary layer (Hartmann et al., 1997; Liu et al., 2004).

2.3   Convection during CAOs

CAOs provide favourable conditions for the development of a unique type of convection, organized into long two-dimensional rolls. This roll convection results in the occurrence of an organized convective cloud structure, coordinated in street-like patterns oriented in the downwind direction from the continent or ice pack (Liu et al., 2004) (Fig.1.1). This ubiquitous feature has been frequently observed in the North Atlantic during various field campaigns investigating CAOs, such as over the Labrador Sea (Renfrew and Moore, 1999), the Greenland Sea and in the Spitsbergen region (Brümmer et al., 1992; Hartmann et al., 1997). Since this convective behaviour have been investigated to such an extent in previous field experiments, it was decided to not be emphasized during the IGP campaign. It is, however, a characteristic feature during cold air outbreaks and will be briefly explained.

High surface wind speeds and large temperature- and humidity contrasts over the ocean are often responsible for an inflection-point instability of the cross-roll wind profile or convective instability in the presence of vertical wind shear (Etling and Brown, 1993; Renfrew and Moore, 1999). These instabilities result in the development of roll convection, where cloud streets typically form above the updraft part of the circulation and are oriented more or less in the downwind direction (Etling and Brown, 1993).

The roll wavelength appears to increase in the downwind direction as the boundary layer becomes warmer, deeper and more stable. Typically observed wavelengths are 2–20 km, while the boundary layer height is 1–2 km (Etling and Brown, 1993). Usually, the roll wavelength increases at a higher rate than the BL height. Hence, the aspect ratio (i.e. the ratio between wavelength and BL height) also appears to increase downwind as the roll convection eventually evolves into cellular convection (Hartmann et al., 1997).

2.4   Boundary layer development

Due to the large magnitudes of sea-air fluxes involved in a CAO event, the boundary layer structure transforms with respect to temperature, humidity, wind and vertical extent. The thermodynamic properties are also typically well-mixed throughout the entire boundary layer during a CAO event due to gradual heating from below.
Findings from the field experiments ARKTIS 1993 by Brümmer (1996) and ARTIST 1998

by Hartmann et al. (1999) show that a typical boundary layer thickness is 100–300 m over the ice while it reaches 900–2200 m over the ocean (Fram Strait in this case).

Besides air-sea temperature differences, the boundary layer is mainly influenced by the stability in the inversion on top of the layer, which generally decreases downwind due to latent heat release in the cloud layer. The inversion stability also influences the cloud pattern, as weaker stability allows more variability in the height of the cloud tops (Brümmer, 1999).

During a CAO, the air masses just off the ice edge are strongly destabilized by the strong sensible heat fluxes from the ocean. Accordingly, as the boundary layer is deepening, warming and mixing, the stability increases. On average, the stability is found to be twice as large in the cell region as in the roll region closer to the continent (Brümmer, 1999).

The strong instability and intense surface heat fluxes near the ice edge are often associated with strong surface winds (Papritz and Spengler, 2017). The wind speeds are found to be largest near the ice edge due to strong thermal contrasts, but an acceleration downstream is also often apparent as a result of the typical pressure distribution with high pressure over the ice and low pressure over the ocean (Brümmer, 1996). Kolstad (2017) proposes that wind speeds during CAOs are higher than during normal conditions due to a downward mixing of momentum from the low-level jet. The intense surface heat fluxes are also typically accompanied by strong winds since the heat from the ocean results in a considerable amount of movement of the air molecules.

These strong surface winds are important in the research on boundary layer development during CAOs. However, they appear spatially small in scale and are thus not always able to be by weather forecast models, in particular reanalysis data. Several studies have shown that reanalyses do not fully resolve polar lows associated with CAOs (Zappa et al., 2014; Pezza et al., 2015), and Kolstad (2017) states that *reanalyses with a grid spacing of 50 km or more underestimate the actual relationship between CAOs and wind speeds* in his paper on ocean winds during marine CAOs.

Reanalysis is an important tool for CAO modelling, and several field experiments have applied mesoscale prediction models for simulating the characteristics of the event. However, high resolution is crucial for resolving severe features associated with CAOs, such as high wind speeds, convection and air-sea interactions, since these can be difficult to capture accurately, especially over the MIZ during a CAO. Fortunately, the development of forecast models is constantly improving, with higher resolutions and more accurate parametrizations. Consequently, weather forecast models used during field experiments today are substantially more accurate than 10–20 years ago.

2.4.1 Previous field experiments

Brümmer (1996) investigated ten cold air outbreak events near Spitsbergen in wintertime during the field experiment ARKTIS 1993. The study mainly focused on modifications of the boundary layer properties, which were observed and measured by radiosondes, two research ships, one icebreaker and two research aircrafts. The temperature was observed to increase in the downwind direction due to sensible heat fluxes near the surface and heat exchange on top of the boundary layer. The surface sensible and latent heat fluxes were found to be the governing terms in the surface energy budget, with magnitudes between 200 and 700 Wm^{-2} over open water. Furthermore, the moisture stratification at the top of the boundary layer was always negative over the ocean as the boundary layer was

moistened by the ocean. In six out of ten cases, a moisture inversion was observed over the sea ice.

Wacker et al. (2005) presented observations from the ARTIST field campaign (Arctic Radiation and Turbulence Interaction STudy, by Hartmann et al. (1999)), which took place during a CAO episode in April 1998, also over the Fram Strait. During the campaign, the boundary layer structure was observed to be stretching approximately 300 km downwind from the ice edge, where the thickness of this convective layer increased gradually to about 1500 m at a distance of 200 km from the ice. Wacker et al. (2005) also applied a mesoscale weather prediction model 'Lokal Model' (LM) to simulate the arctic CAO during the study period. The model results were compared with the observations from the ARTIST campaign for validation. As the model LM was developed for mid-latitude meteorological situations, a few basic problems arose concerning sea-ice parameters, stability and underestimation of surface heat fluxes. Nevertheless, the model simulated the overall propagation of the cold air masses reasonably well, and it was proven useful for typical polar weather conditions provided available high-resolution sea-ice data.

Additionally, as a part of the Labrador Sea Deep Convection Experiment, Renfrew and Moore (1999) investigated an extreme cold air outbreak event associated with the passage of a low pressure system over the Labrador Sea in February 1997. The campaign focused on the structures of the roll convection and the air-sea interactions, utilizing a research aircraft and a research vessel. Such coordination between aircraft and ship was also implemented during the IGP campaign.
Both temporal and spatial evolution of the boundary layer was analysed by studying cross-sections of various thermodynamic parameters from two separate aircraft missions ten hours apart. Sharp horizontal gradients of both temperature and specific humidity were apparent at the edge of the marginal ice zone, and the boundary layer was found to be increasing, warming and moistening downwind and with time. Consistent peaks of specific humidity were collocated with the updrafts of the roll vortices with typical wavelengths of 4–5 km, associated with boundary layer heights of 1–1.2 km.

Like the aforementioned case studies, the flight campaign during the Iceland-Greenland Seas project (IGP) was an aircraft-based project which focused on cold air outbreaks and the related boundary layer modifications. Additionally, LM's successor model, COSMO, was applied for simulating the atmospheric conditions during the study period, in the same manner as LM was used for the ARTIST campaign. COSMO is, like LM, a non-hydrostatic, high-resolution model introduced at the German weather service DWD (Steppeler et al., 2003). It is an updated version of LM with more flexibility and a finer spatial resolution of ∼5.5 km.
By frequently measuring the boundary layer in this domain and implementing a well-functioning regional model, the IGP experiment contributes to higher model precision over the Iceland-Greenland Seas.

3   IGP field project

During February and March 2018, the Iceland-Greenland Seas project (IGP) took place over the Iceland- and southern Greenland Seas. The campaign was a coordinated atmosphere-ocean research program, which utilized both a research aircraft and a research vessel that simultaneously sampled the atmosphere, ocean and their interactions.

The flight campaign was based in Akureyri in Iceland. It was a cooperation between scientists of University of Eastern Anglia (UEA) and University of Bergen (UiB), pilots and aircraft coordinators from British Antarctic Survey (BAS) and forecasters from Icelandic Met Office (IMO). The instrumented aircraft flew across the Iceland Sea in different patterns and altitudes depending on the scientific aims and weather conditions (ex. Fig 1.1). In total, 14 flight missions were conducted during the period from 28 February to 19 March, mostly over the Iceland Sea and the MIZ near the Greenland coast (Table 3.1). Flight 296 on 5 March is not counted as a mission since it was only a transit flight from Reykjavik to Akureyri.

Table 3.1: Flight dates, times, flight number, flight track and instrumentation remarks for each flight during the period 28 Feb–19 Mar 2018. A = Akureyri, Re = Reykjavik, CP = Constable Point, MIZ = Marginal Ice Zone. The most relevant flights for this study are marked green.

Date	Time (UTC)	Flight no.	Track	Remarks
28 Feb	07:48 - 11:51	292	A–A	-
01 Mar	08:13 - 11:45 13:06 - 18:02	293 / 294	A–CP–A (coord. with ship)	-
02 Mar	-	-	Cancelled flight	-
03 Mar	-	-	Rest day	-
04 Mar	10:16 - 15:09	295	A–Re (coord. with ship)	-
05 Mar	10:30 - 11:20	296	Re–A (transit)	No usable data
06 Mar	08:47 - 14:14	297	A–A (coord. with ship)	Trouble with Rosemount (temp.) and BAT (wind)
07 Mar	-	-	Cancelled flight	-
08 Mar	08:21 - 11:56 13:27 - 19:01	298 / 299	A–CP–A (across and along MIZ)	-
09 Mar	09:58 - 14:47	300	A–A (sawtooth across MIZ, low level not viable)	Trouble with Licor: no H_2O data
10 Mar	-	-	Cancelled flight	-
11 Mar	-	-	Rest day	-
12 Mar	12:13 - 18:13	301	A–A (orographic flows)	-
13 Mar	-	-	No flight	-
14 Mar	NaN - NaN 12:55 - 18:28	302 / 303	A–CP–A (across MIZ)	Most data lost
15 Mar	-	-	No flight	-
16 Mar	09:55 - 11:45	304	A–A (around Husavik)	-
17 Mar	-	-	No flight	-
18 Mar	09:09 - 14:59	305	A–A	-
19 Mar	13:01 - 17:29	306	A–A (orographic flows)	-

I myself participated in the flight campaign in Akureyri from 7 to 14 March. During my stay I gathered experience in flight planning and provided daily weather forecasts for the IGP team. The flight planning included discussing flight tracks, waypoints, mission scientists and weather concerns. The flight track would preferably include low level flying

at minimum safe altitude (∼20–50 m above sea surface), sawtooth patterns within the boundary layer and high level transit to obtain a comprehensive representation of the observed situation.

The weather forecasts were retrieved from the high resolution (2.5 km) HARMONIE-AROME model by the Icelandic Met Office and the Danish Meteorological Institute for the limited IGP domain, together with UK Met Office's MetUM model (2.2 km) over the same region. Both models permitted convection and were initialised twice a day from global forecasts from the Met Office and ECMWF.

3.1   Weather situation during 4–9 March 2018

The weather situation during the campaign was reasonably supportive for our experimental studies, with a low pressure system (<987.5 hPa) south-east of Iceland and a persistent high pressure (>1037.5 hPa) over Greenland during more or less the entire study period (Fig. 3.1).
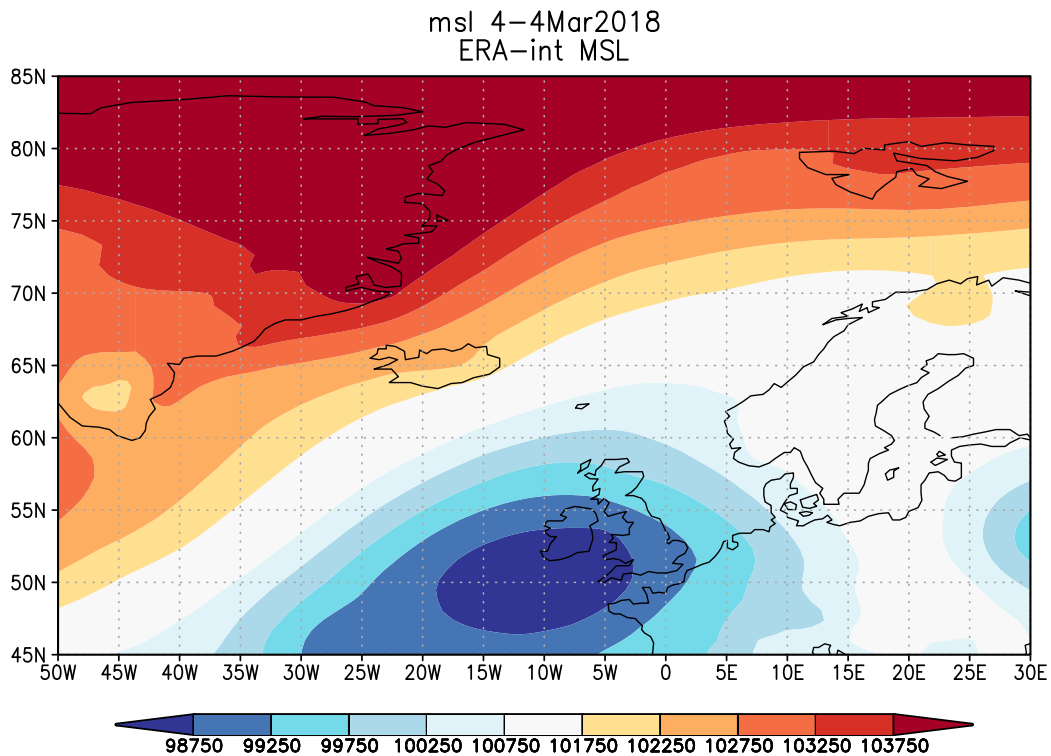
Figure 3.1: Mean sea-level pressure (filled contours, Pa) on 4 March 2018 (average over one day), from the ECMWF reanalysis ERA-interim, obtained from the Royal Netherlands Meteorological Institute (KNMI) Climate Explorer (van Oldenborgh et al., 2005).

The weather situation on 4 March 12 UTC was primarily dominated by northerly/north-easterly winds and sub-zero temperatures according to the HARMONIE model (Fig. 3.2). High surface wind speeds (up to 18 ms^{-1}) were evident along the ice edge (Fig. 3.2a) in the region of sharp horizontal temperature gradients of roughly 2 K per degree (Fig. 3.2b).

11

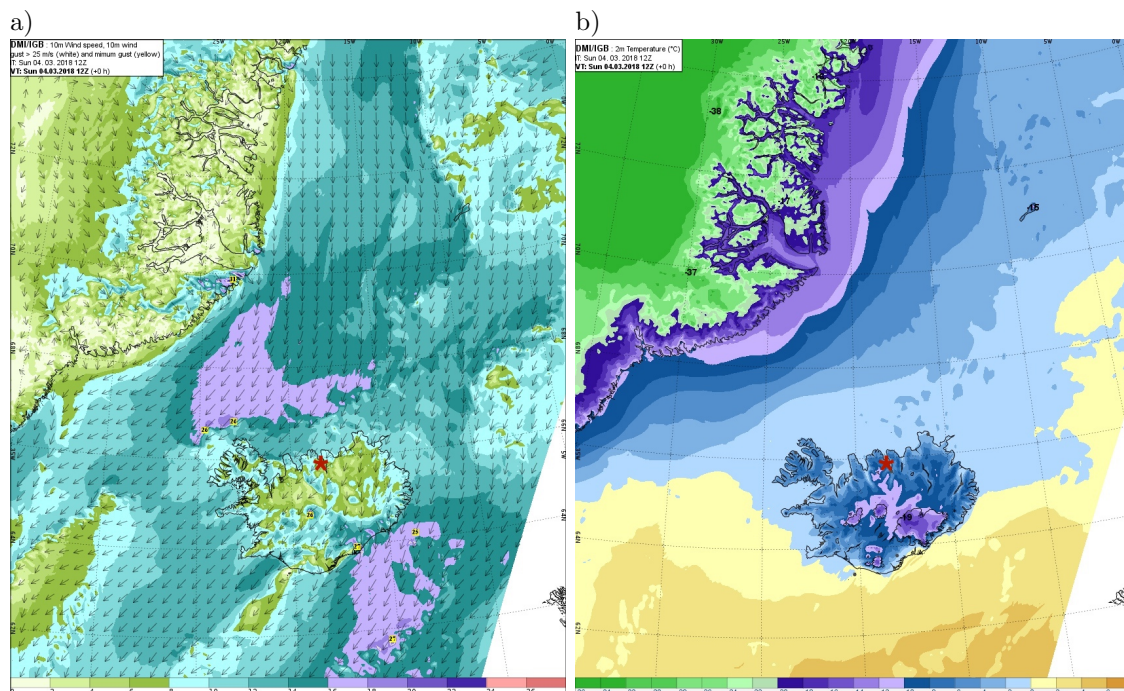Figure 3.2: Weather situation on 4 March 2018 12 UTC from HARMONIE (IMO, 2018) at initial forecast time (+00h) depicted by the different variables: a) 10 m wind speed (ms^{-1}) and wind vectors and b) 2 m temperature (°C). The red star indicates the location of Akureyri.

Such notably large temperature contrasts and strong surface winds are typically associated with a developing convective boundary layer and intense surface heat fluxes, which are governing aspects of cold air outbreaks.

A specific emphasis has been placed on the period of 4–9 March since the CAO appeared to dominate the weather situation during this period. The measured thermodynamic bulk properties from the relevant flights and radiosondes are investigated in order to characterize their temporal and spatial development over the ocean during a CAO. This period is also the target for isotopic measurements during the CAO with frequent isotope observations taken from aircraft, vessel and snow samples.
Surface sensible heat flux- and cloud cover analyses are used in the following discussion of the weather situation over the Iceland Sea during the given period (Figs. 3.3 and 3.4). Satellite images, daily forecasts from the campaign period and observations by the mission scientists on board the aircraft have also been emphasized.
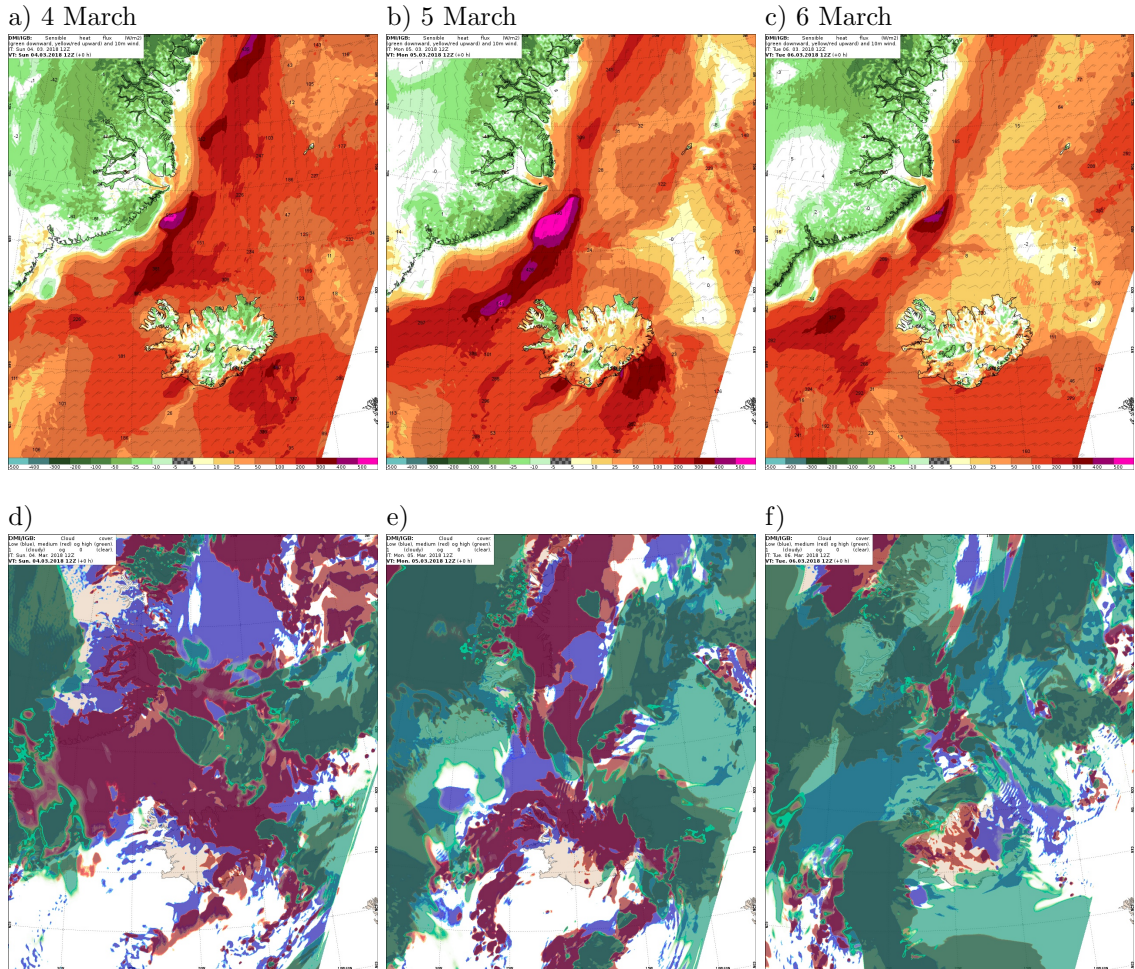
a) 4 March

b) 5 March

c) 6 March

d)

e)

f)

Figure 3.3: Model analyses of a,b,c) surface sensible heat flux (Wm^{-2}) and 10 m wind, and d,e,f) cloud cover: low (blue), medium (red) and high (green) on 4, 5 and 6 March 2018, 12 UTC (+00h) (from HARMONIE).

Generally, the surface sensible heat fluxes (SHFL) are most intense just off the MIZ. This is where the cold air from over the ice interacts with the warmer ocean surface, leading to a substantial transfer of heat from the ocean to the atmosphere. Such intense SHFLs are characteristic features during CAOs. A consequence of the heat transfer from the ocean to the atmosphere is convection and cloud development in the area. Accordingly, a persistent low cloud band was consistently laying over the ice edge (blue). This low cloud band was also observed on satellite images (e.g. Fig. 1.1).

4 March was mostly characterized by northerly 10 m winds over the Iceland Sea with speeds ranging from 10 to 18 ms^{-1} (Fig. 3.2a). A low cloud band lay over the ice edge and large parts of the Iceland Sea (Fig. 3.3d), and convective cells with frequent snow showers were apparent north of Iceland. Due to thick clouds near Akureyri, the aircraft mission was forced to to divert to Reykjavik for landing. The SHFL were quite strong on 4 March, with values of about 500 Wm^{-2} just off the ice edge at 69°N (Fig. 3.3a). This field of high fluxes expanded and intensified to nearly 800 Wm^{-2} during the next day (pink field, Fig. 3.3b). On 5 March, a strong jet off the ice edge was apparent and a low cloud band lay over the MIZ and the ocean (Fig. 3.3e). Further, two separate high cloud bands moved in from each side (Fig. 3.3e) and appeared to merge on 6 March (Fig. 3.3e).
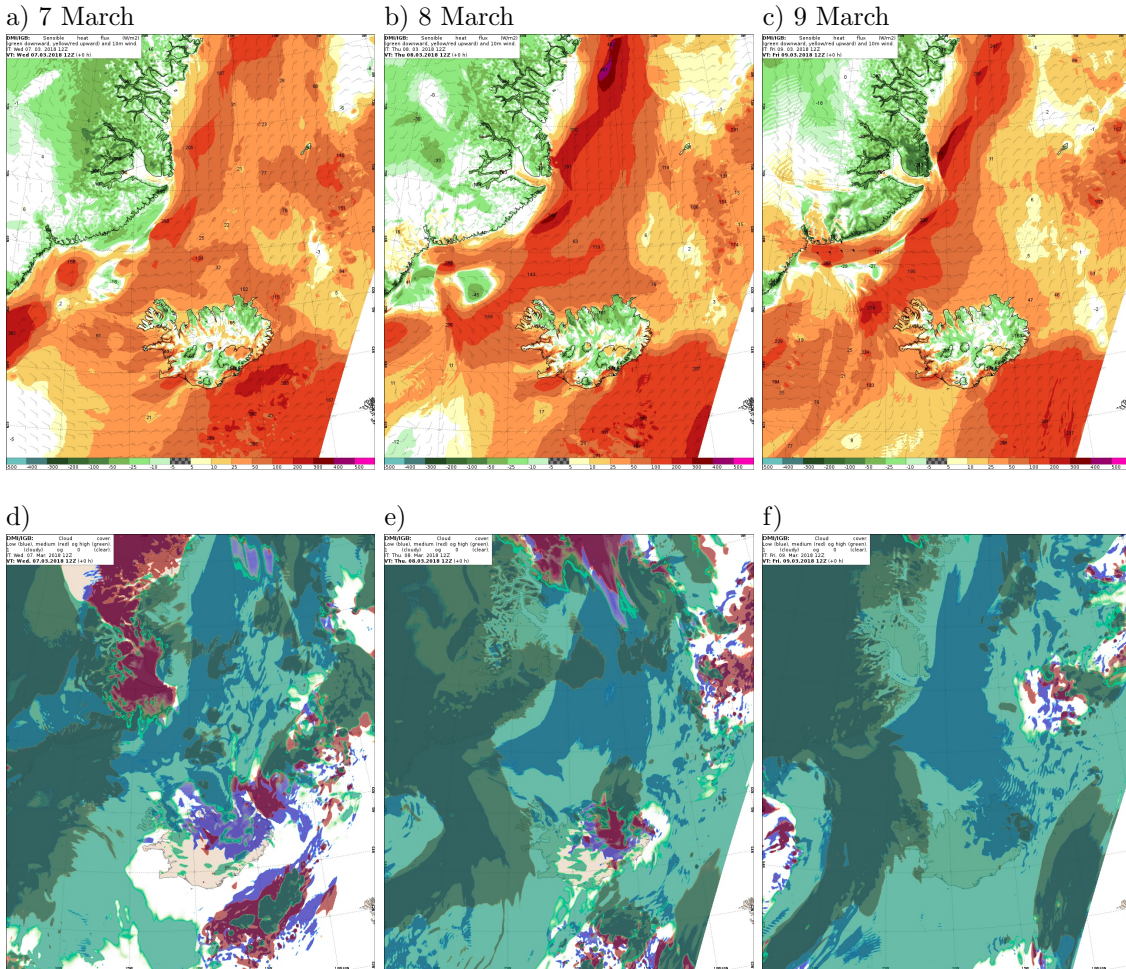
Figure 3.4: As Figure 3.3 but for 7, 8 and 9 March 2018.

During this day, the distinct field of high SHFL diminished rapidly (Fig. 3.3c), whereas it was nearly gone on 7 March with values of approximately 200 Wm^{-2} (Fig. 3.4a). A low cloud band and convective snow showers were apparent over the entire Iceland Sea on 7 March (Fig. 3.4d), which resulted in a cancellation of the flight on this day.

8 March, however, consisted of relatively better flight conditions, and a flight to Constable Point for refuel and back to Akureyri was successfully carried out (flight 298 and 299 in Table 3.1). Dense convective clouds were present during transit (Fig. 3.4e), but the cloud layer became shallower as the aircraft approached Greenland. A thin cloud layer was observed at approximately 300 m height off the ice edge, and at CP the conditions were clear with high cirrostratus according to the mission scientists on board the aircraft. The conditions were also measured to be quite turbulent at low level, with maximum wind at around 90 m height according to the scientists. A small area of high SHFL was detected furthest north in the model domain (nearly 74°N) with values of about 450 Wm^{-2} (Fig. 3.4b). However, this field also diminishes during the day, and is nearly absent on 9 March (Fig. 3.4c). The weather conditions on 9 March were also dominated by strong northeasterly winds and an extensive high cloud layer lay over the entire ocean. A thick low cloud band was observed over large parts of the ocean (Fig. 3.4f) with a cloud base below 150 m according to the mission scientists. Consequently, the conditions were not suitable for the planned low level flying this day (flight 300 in Table 3.1).

4   Method

The observations during the IGP campaign were mainly based on measurements by the British Antarctic Survey's Twin Otter research aircraft, and the NATO research vessel *Alliance*. Radiosondes were frequently released from the vessel, providing continuous profiles of various thermodynamic parameters within the atmospheric boundary layer. These increased the accuracy of the observed analysis during IGP.

My study mainly focuses on the thermodynamic parameters measured by the Twin Otter aircraft and radiosondes. Accordingly, the observations will be compared with a high-resolution COSMO model to see how accurately the model simulates the situation, and to find the optimal model setup that simulates the water cycle and the isotopic composition with the highest precision. First, the applied method for analysing the aircraft-, radiosonde- and model data will be presented.

4.1   Aircraft data and instrumentation

The primary objective of the meteorological campaign was to investigate the impact a cold air outbreak has on the surface fluxes and boundary layer properties downstream of the sea ice. The research aircraft was a Twin Otter aircraft of British Antarctic Survey (BAS, 2015), equipped with the Meteorological Airborne Science INstrumentation (MASIN). The aircraft was equipped with multiple airborne atmospheric instruments, including sensors measuring temperature, water vapour, turbulence and wind (Fig. 4.1, Table 4.1). During the IGP campaign, the aircraft also carried a Picarro Isotope- and Gas Analyser which measured the isotopic composition of water vapour with high precision.

Figure 4.1: BAS Twin Otter Aircraft, equipped with MASIN instrumentation. The numbers refer to Table 4.1 to illustrate where the various instruments are located on the aircraft.

Table 4.1: Airborne atmospheric instrumentation of British Antarctic Survey Twin Otter Aircraft, and their measured units (BAS, 2015).

No.	Parameter	Instrument	Units
1	Pressure	Heated pitot tube	hPa
2	Temperature	Rosemount sensor	K
3	Dew point	Buck cooled mirror hygrometer	K
4	Radiation	Eppley radiometer	Wm^{-2}
5	H_2O	Licor	$mol\ mol^{-1}$
6	True air speed	Best Aircraft Turbulence (BAT) probe	ms^{-1}
7	Lon/Lat/Alt	OXTS system	$°E/°N/m$

For the purpose of measuring air-sea interactions, the flights were carried out at minimum safe altitude at approximately 20–50 m above sea level. Additionally, complete vertical cross-sections of various boundary layer characteristics were obtained by flying in a saw-tooth pattern along the cross-section of interest.

The flights during 4–9 March were mainly carried out over the Iceland Sea and near the MIZ (Figs. 4.2 a–e). Flight 295 and 297 were also coordinated with the ship (Table 3.1).
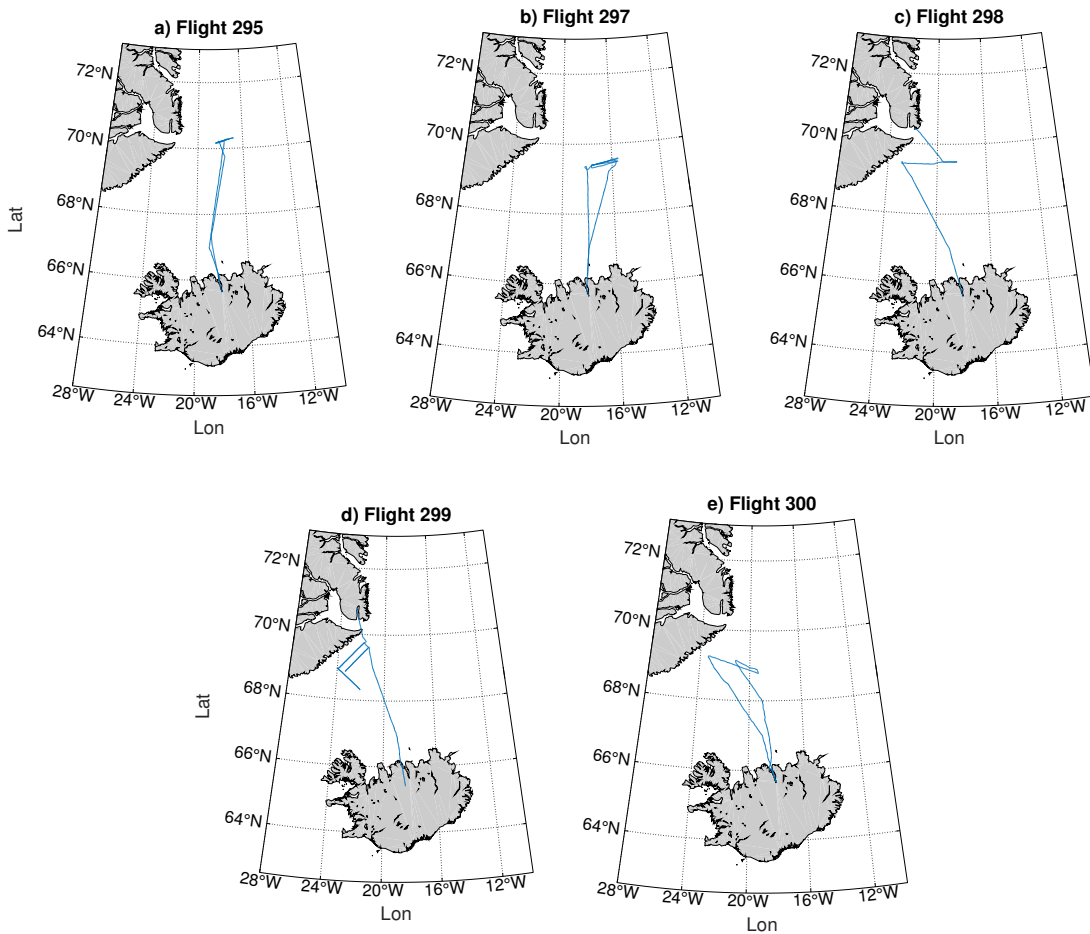

Figure 4.2: Flight tracks for flight 295, 297, 298, 299 and 300 respectively.

I have chosen to first investigate flight 295 (Fig 4.2a) in detail since this flight was conducted at approximately the same time and location as four radiosonde releases from the research vessel. Furthermore, the COSMO model exhibits some notable features over the Iceland Sea on this day, in which the aircraft and radiosonde observations will contribute to validation.

Subsequently, I have investigated data from flights 298 (Fig. 4.2c) and 299 (Fig. 4.2d), where several ascents/descents sampled the boundary layer near and over the MIZ. The thermodynamic properties along a short flight leg perpendicular to the Greenland coast during flight 299 have also been compared with data from the COSMO model (Sec. 5.5.2). In this case, the aircraft flew in a sawtooth pattern over the MIZ, towards the open ocean, through the depth of the boundary layer. The retrieved data from this flight leg provides information about how the thermodynamic boundary layer evolves moving away from the Greenland coast, which is an integral part of my study. In addition, as shown in Table 3.1, there were no instrumentation errors during any of these three flights.

4.1.1 Aircraft measurements and data correction

The Twin Otter aircraft is equipped with multiple airborne high-precision atmospheric instruments (Elvidge et al. (2015), Table 4.1), and continually samples measurement data with a sample period of one second. However, a few instrument malfunctions caused some errors, especially related to humidity data (Table 3.1). An error that occurred for all flights was that the dew point temperature regularly exceeded the true air temperature, resulting in unrealistic relative humidities (over 100%). This inconsistency is primarily caused by the two parameters being retrieved from different instruments; The Buck cooled mirror and The Rosemount probe. The Buck instrument uses a mirror that is permanently cooled to a temperature well below its measurement range. The mirror temperature is then raised to the dew point and maintained at that point by an electrical heater (Wendisch and Brenguier, 2013). Further, the Rosemount probe is a temperature sensor of high precision due to corrected dynamic error sources (Nagabhushana and Sudha, 2010).

The dew point temperature also typically exhibited a spiky behaviour during the first 30–60 minutes of every flight. The Buck cooled mirror instrument thus required some adaption time in order to provide precise measurements.

Relative humidity data was included in the data set from the Rosemount probe, but gave unrealistically high values (on the order of 10^7). It was therefore necessary to calculate the relative humidity from saturation vapour pressure and vapour pressure, which are based on true air temperature and dew point temperature respectively.
From Bolton (1980), the saturation vapour pressure e_s (hPa) and vapour pressure e (hPa) for $-30°C \leq T \leq 35°C$ are defined as

$$e_s(T) = 6.112 \cdot \exp\left(\frac{17.67 \cdot T}{T + 243.5}\right)$$

(4.1)

$$e(T_d) = 6.112 \cdot \exp\left(\frac{17.67 \cdot T_d}{T_d + 243.5}\right)$$

(4.2)

where T is the air temperature (°C), T_d is the dew point temperature (°C), and the constant 6.112 is the coefficient of best polynomial fit to saturation vapour pressure (Flatau et al.,

1992). Accordingly, Brock and Richardson (2001) defines specific humidity q (g kg^{-1}) and relative humidity (%) as:

$$q = \frac{0.622 \cdot e}{p - ((1 - 0.622) \cdot e)} \cdot 1000 \qquad (4.3)$$

$$RH = \frac{e}{e_s} \cdot 100\% \qquad (4.4)$$

where p is the static air pressure (hPa), and the constant 0.622 is the ratio of the gas constant for dry air to the gas constant for water vapour.
The specific humidity is initially dimensionless (kg kg^{-1}), but is scaled to obtain the specified unit g kg^{-1}.

Vertical profiles of temperature and humidity can be made by selecting certain transit periods where the aircraft ascends, descends or flies in a sawtooth pattern. An important factor to be aware of is the adjustment time of sensors in the face of rapid change, which may result in different humidity measures during ascents and descents. In an effort to reduce this source of error, only the descents are considered when retrieving vertical profiles from sawtooth legs. Furthermore, vertical profiles of various thermodynamic properties over the Iceland Sea are also obtained from radiosondes, which were frequently released from the ship.

4.2 Radiosonde data

The research vessel was another essential platform during the field project, carrying several oceanographic and meteorological instruments. Radiosondes were released from the ship approximately every 3–6 hours during interesting weather or when in vicinity of the aircraft. In total, 100 radiosondes were released during the campaign, of which 23 of them were released during 4 to 9 March (Table 4.2). Measured parameters include pressure (hPa), temperature (°C), relative humidity (%), dew point temperature (°C), wind speed (ms^{-1}), wind direction (°), potential temperature (°C) and specific humidity (g kg^{-1}).

Table 4.2: Overview of radiosonde launches from the research vessel in the period 4–9 March during the IGP campaign (from Weng and Sodemann (2019)). The radiosondes used in this study are marked blue.

No.	Date	Time (UTC)	Lat (°N)	Lon (°W)	Remark
46	4 Mar 2018	00	70.16	15.56	
47	4 Mar 2018	06	70.24	16.51	
48	4 Mar 2018	09	70.26	16.78	
49	4 Mar 2018	12	70.28	17.16	
50	4 Mar 2018	15	70.30	17.53	
51	4 Mar 2018	18	70.32	16.93	
52	5 Mar 2018	06	70.55	16.13	
53	5 Mar 2018	09	70.21	15.65	
54	5 Mar 2018	12	70.21	15.95	
55	5 Mar 2018	18	NaN	NaN	Instrument error after launch
56	5 Mar 2018	18	70.28	16.80	
57	6 Mar 2018	00	70.10	17.51	
58	6 Mar 2018	06	NaN	NaN	Instrument error after launch
59	6 Mar 2018	06	69.31	17.42	
60	6 Mar 2018	09	69.21	16.97	
61	6 Mar 2018	12	69.39	16.48	
62	6 Mar 2018	15	69.47	17.01	
63	6 Mar 2018	18	69.56	17.73	
64	7 Mar 2018	00	69.70	18.94	
65	7 Mar 2018	06	69.92	17.05	
66	7 Mar 2018	12	69.06	16.80	
67	7 Mar 2018	18	67.85	17.92	
68	8 Mar 2018	00	66.84	18.28	

The frequency of radiosonde releases was more inconsistent during 4–9 March due to some time off in Akureyri for the crew on 8 and 9 March. However, the first four days are well represented. For comparison with flight data, 4 March was considered the optimal date due to the precise coordination between aircraft and radiosonde releases, and lack of instrumentation errors (Table 3.1). In addition to this, a flight descent during flight 295 was conveniently located very close to the position of the ship and the radiosonde releases during this day (red line, Fig. 4.3).
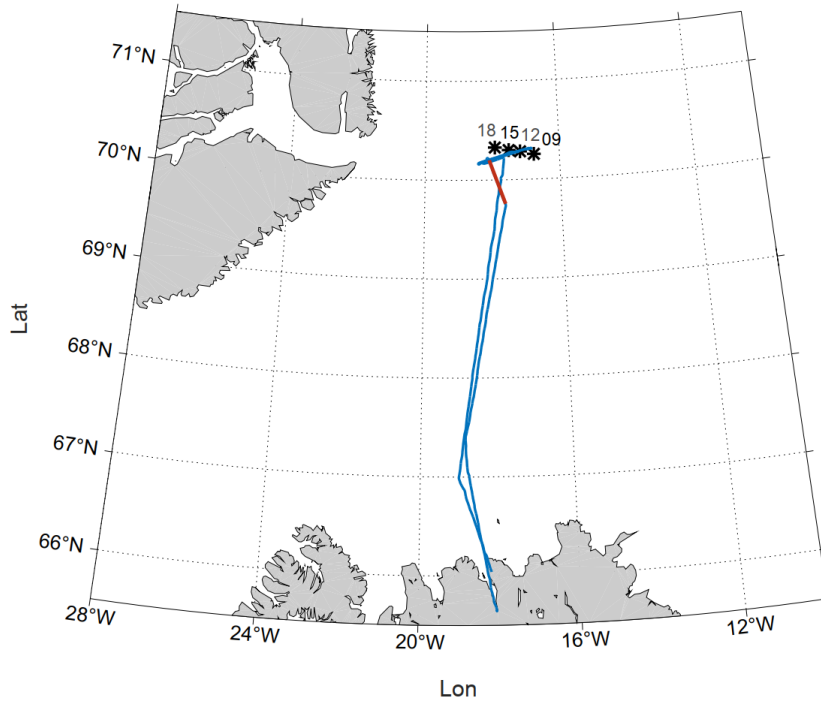
Figure 4.3: Radiosonde locations (black stars) and flight path from flight 295 (blue line) on 4 March 2018. Numbers indicate time of radiosonde releases in UTC, and the flight descent is highlighted in red. .

Four radiosondes from 4 March were released three hours apart along a straight line, stretching approximately 44 km from east to west at 70.3°N (Fig. 4.3). The radiosonde releases were aligned approximately in the downwind direction from the ice edge, creating an optimal basis for boundary layer investigation.

The distances between the radiosonde locations have been calculated with the *Haversine-formula* from Veness (2019).

$$
\begin{aligned}
a &= \sin^2\left(\frac{\Delta\phi}{2}\right) + \cos\phi_1 \cdot \cos\phi_2 \cdot \sin^2\left(\frac{\Delta\lambda}{2}\right) \\
c &= 2 \cdot \arctan 2(\sqrt{a}, \sqrt{1-a}) \\
d &= R \cdot c
\end{aligned}
\tag{4.5}
$$

Where ϕ is latitude, λ is longitude and R is the earth radius (6371 km).

The Haversine formula (Eq. 4.5) obtains the 'great-circle' distance between two points - that is, the shortest distance over the Earth's surface. The locations of the radiosondes were selected to be the release point coordinates. It is worth noting that the radiosondes drift slightly with the wind along their ascent, but this is of limited significance since the horizontal displacements are relatively small. Based on the coordinates of each radiosonde release on 4 March (Table 4.2), the distances between them are approximately 13–15 km apart (Table 4.3).

Table 4.3: The distances between the radiosonde releases on 4 March 09, 12, 15 and 18 UTC calculated with the Haversine formula (Eq. 4.5) using the coordinates from Table 4.2.

Radiosondes (UTC)	Distance (km)
09 → 12	14.72
12 → 15	13.85
15 → 18	15.35
09 → 18	43.92

The speed of the ship can then easily be calculated by dividing the distance (m) with time between each uplift, which results in an average velocity of approximately 1.35 m/s.

The radiosonde profiles were also plotted in thermodynamic *skew-T log-P* diagrams. Such diagrams include dry adiabats, moist adiabats, saturation mixing ratio and wind barbs for reference, making it easy to analyse the state and stability throughout the lower atmosphere. They are also useful for detecting the different convective levels in the lower troposphere. By horizontally interpolating the vertical columns of data from the four radiosondes, vertical cross-sections of various thermodynamic parameters throughout the boundary layer can be retrieved. These vertical cross-sections provide information about the horizontal and vertical propagation of the thermodynamic properties, which is of great relevance in this study.

4.3   Simulations with COSMO$_{iso}$

The high resolution, non-hydrostatic COSMO$_{iso}$ model (Steppeler et al., 2003) is applied
to simulate the characteristics of the boundary layer and the atmospheric water cycle
during the study period. Accordingly, it is being compared to radiosonde- and flight data
in order to investigate the correspondence with the observed thermodynamic properties
of the boundary layer. In this study, the COSMO model provides data every three hours
and includes a rotated grid with horizontal grid spacing of 0.05°, corresponding to ap-
proximately 5.5 km. Further, 40 hybrid vertical levels are used. The model domain covers
the area around Iceland, the Iceland Sea and the southern Greenland Sea (Fig. 4.4),
and stretches vertically to ∼40 hPa. The initial boundary data are interpolated from the
atmospheric general circulation model ECHAM5-Wiso (M. Werner, AWI, pers. comm.),
nudged to the European Centre for Medium-Range Weather Forecasts (ECMWF) reanal-
ysis data ERA-interim. This global model system provides data every six hours with a
much lower resolution than COSMO, which, in this case, lead to erroneous values at, and
close to, the boundaries. These boundaries, with a width of 11 grid points, have thus been
removed from the domain (dashed lines, Fig 4.4). The detailed simulation setup is given
in Appendix A (Listings 1 and 2).
The COSMO model is extended for the purpose of simulating stable isotopes in the at-
mospheric water cycle by implementing isotopes from ECHAM5-Wiso (Pfahl et al., 2012;
Werner et al., 2011). The study of isotopes will, however, not be emphasized in this study.
The parameters of greatest interest are temperature and humidity, whereas modelled fluxes
and wind patterns will be mentioned as influences on the lower atmospheric behaviour.

The vertical structure of the lower atmosphere is represented by simulated profiles of
various parameters, such as temperature (°C), potential temperature (K) and specific hu-
midity (g kg^{-1}). The potential temperature (θ) is included in the radiosonde data, but
for the flight- and model data θ is calculated as follows (Stull, 1988);

$$\theta = T\left(\frac{p_0}{p}\right)^{R/c_p} \tag{4.6}$$

where T is true air temperature in K, p$_0$ is surface reference pressure (set as 1000 hPa), p
is air pressure in hPa, R is the gas constant (287 J K^{-1}kg^{-1}) and c$_p$ is the heat capacity
of dry air at constant pressure (1004 J K^{-1}kg^{-1}).
Furthermore, equivalent potential temperature (θ$_e$) has been used in investigating the sta-
bility of the simulated atmosphere as θ$_e$ is a function of both temperature and humidity:

$$\theta_e = \left(T + \frac{L_v}{c_p}q\right)\left(\frac{p_0}{p}\right)^{R/c_p} \tag{4.7}$$

where L$_v$ is the latent heat of evaporation (2501 kJ kg^{-1} at 0°C) and q is the specific
humidity or mixing ratio of water vapour mass per mass (kg kg^{-1}).

When investigating horizontal distributions of the various thermodynamic bulk properties,
the ice edge is interpreted as the boundary of where the ocean surface temperature falls to
−1.7°C. This approximation was also done by Wacker et al. (2005) when the Lokal Model
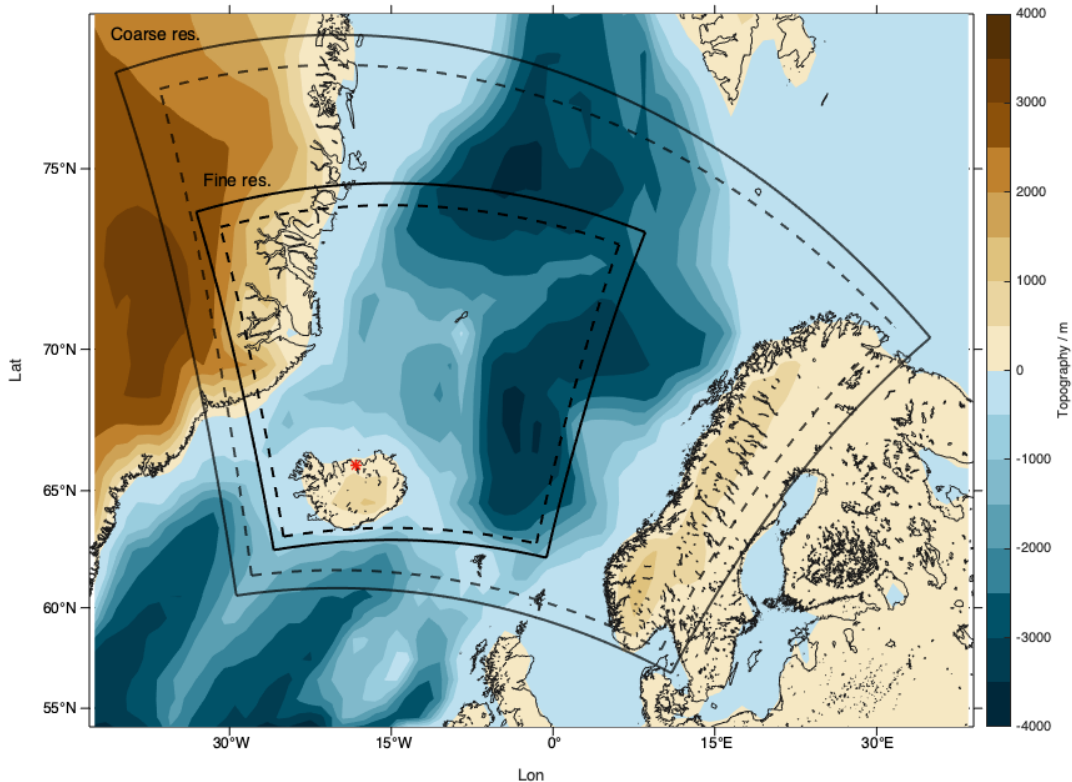was implemented over the Fram Strait.

Figure 4.4: The COSMO$_{iso}$ model domains for the fine-resolution runs (small) and the coarse-resolution runs (large) over the topography/bathymetry (colours in metres a.s.l.) in the Nordic Seas-area. The removed boundary layer zone is indicated by the dashed lines, and the red star marks the location of Akureyri.

4.3.1   Accuracy measures for model validation

When comparing model results with observed values, the bias and the root mean square error (RMSE) are measured for accuracy. The bias (mean error) describes the average difference between the absolute values of the model and observations, while RMSE represents the square root of the averaged squared differences. RMSE is therefore always positive, regardless of whether the model overestimates or underestimates. The accuracy is highest when both measures approach zero.

The bias and RMSE between the modelled value m and observed value o are defined as follows (Warner, 2011):

$$bias = \frac{1}{n} \sum_{i=1}^{n} (m_i - o_i) = \bar{m} - \bar{o}. \tag{4.8}$$

$$RMSE = \sqrt{\frac{1}{n} \sum_{i=1}^{n} (m_i - o_i)^2} \tag{4.9}$$

These accuracy measures are also used when various model runs with different initial conditions are compared with the observed situation.

4.3.2 Model simulations

First, three high-resolution model runs will be presented and compared for 4 March 2018, 09 UTC. Each model run is initialised at different times, at which the optimal lead time will be determined by its correlation to the observations. The three runs are initialised on 2 March 00 UTC (+57h), 3 March 00 UTC (+33h) and 4 March 00 UTC (+9h), hereafter labelled run 0200, 0300 and 0400 respectively (yellow rows in Table 4.4). Comparing results from the three runs will then provide an idea of how the lead time influences the sensitivity of the thermodynamic parameters. For longer spin-up time, the model will pick up on more detailed structures. However, instabilities and various weather systems may get more time to develop. Instabilities are also believed to occur from spin-up problems during the transition from the coarse initial boundary data to the high-resolution COSMO simulation. Simulations from 2 and 3 March were therefore run again with a coarser horizontal resolution of 0.2°, corresponding to approximately 22 km, and 40 hybrid vertical levels (hereafter labelled run 0200c and 0300c, Table 4.4). The model domain for these simulations covers a larger part of Greenland and the Nordic Seas (Fig. 4.4).

In addition, a model run initialised on 8 March 00 UTC is used for comparison with flight 299, conducted in the afternoon on 8 March.

Table 4.4: Details on all simulations of COSMO$_{iso}$ used in this study.

Model run	Simulation start	Simulation end	Total running time	Resolution
0200	2 Mar 00 UTC	8 Mar 03 UTC	147 h	fine: 0.05°
0200c	2 Mar 00 UTC	5 Mar 00 UTC	72 h	coarse: 0.2°
0300	3 Mar 00 UTC	9 Mar 03 UTC	147 h	fine: 0.05°
0300c	3 Mar 00 UTC	5 Mar 00 UTC	48 h	coarse: 0.2°
0400	4 Mar 00 UTC	6 Mar 00 UTC	48 h	fine: 0.05°
0800	8 Mar 00 UTC	10 Mar 00 UTC	48 h	fine: 0.05°

5 Results and discussion

The observed thermodynamic bulk properties within the atmospheric boundary layer have been investigated and compared with a high resolution model simulation. The results from this study are categorized into three main parts; aircraft observations (Sec. 5.1), radiosonde observations (Sec. 5.2) and model results (Sec. 5.3). The comparison between simulation and observations are then discussed in Sections 5.4 and 5.5.

5.1 Aircraft observations

The primary science objective for the aircraft campaign during IGP (Sec. 3) was to obtain a comprehensive sampling of the marine boundary layer and the air-sea interactions during a cold air outbreak over the Iceland Sea. Hence, the Twin Otter research aircraft sampled the boundary layer and surface layer over the Iceland Sea and near the Greenland ice edge. The thermodynamic properties within the boundary layer were sampled via ascending/descending or 'sawtooth' patterns, and surface properties were obtained from low level flying at minimum safe altitude, down to about 30 m a.s.l.. The temperature- and humidity measurements during all flights from 4 to 9 March are illustrated in Appendix B. In this section, however, the emphasis is on flights 295, 298 and 299.

5.1.1 Flight 295 (4 March 2018)

Flight 295 on 4 March represents a typical flight mission during the IGP campaign. During this mission, the aircraft flew over the Iceland Sea with a low-level leg furthest north at approximately 70.2°N, in vicinity of the research vessel (Fig. 4.3).

The weather situation during this flight was dominated by low clouds and high wind speeds over the Iceland Sea (Sec. 3.1 and Fig. 1.1). Various thermodynamic bulk properties within the boundary layer were sampled along the flight track, such as pressure and potential temperature, which primarily indicate a gradual vertical warming from about 260 K at 1000 hPa to 271 K at 700 hPa (highlighted in Fig. 5.1).
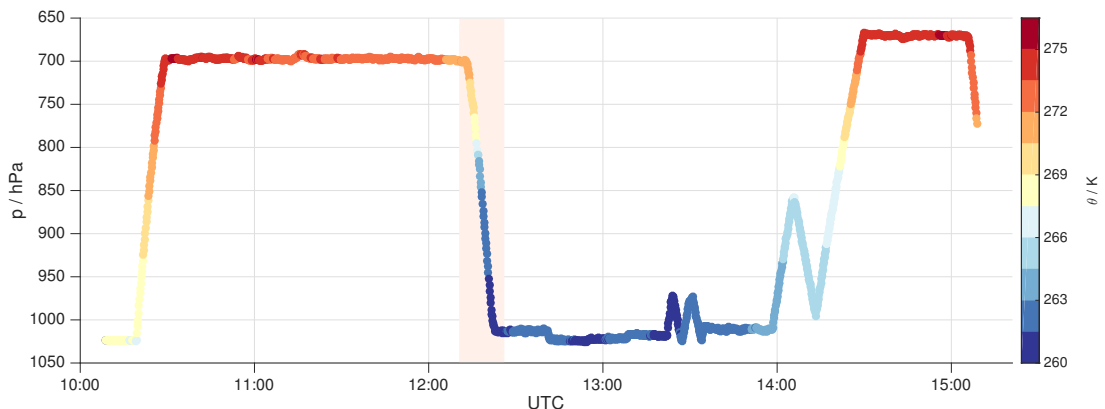

Figure 5.1: Evolution of air pressure (hPa) and potential temperature (K) along the flight path during flight 295 on 4 March 2018. The aircraft is flying northward until approximately 12:30 UTC, at which the low level leg is conducted furthest north (see map of flight track, e.g. Fig. 4.3).

Additionally, when comparing the southern ascent at 10:30 UTC (65.7°N) with the northern descent at 12:15 UTC (70.0°N), a northward cooling also becomes apparent. For example, the potential temperature at 900 hPa is observed to decrease by 8 K from 270 K along the southern ascent to 262 K along the northern descent (Fig. 5.1). The distance corresponds to approximately 450 km.

A near-neutral boundary layer of about 800 hPa depth is also observed along the northern descent at 12:15 UTC. This descent was located close to the ice edge, and the temperature contrasts between ocean and atmosphere are large. The air temperature increases from $-28°C$ at nearly 3 km height to $-10°C$ near the ocean surface (Fig. 5.2a), and the specific humidity varies between 0.3 and 1.4 g kg^{-1} (Fig. 5.2b).
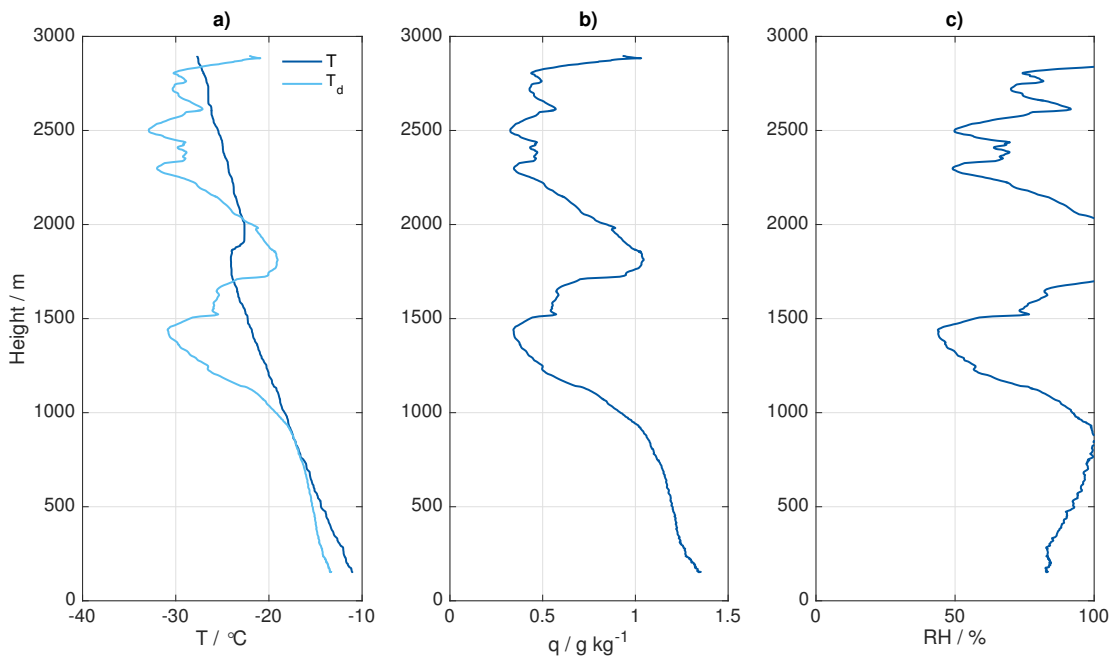

Figure 5.2: Vertical profiles of a) air temperature T (dark blue, °C) and dew point temperature T_d (light blue, °C), b) specific humidity q (g kg^{-1}) and c) relative humidity RH (with respect to water, %) from the descent at 12:15 UTC (highlighted in Fig. 5.1) during flight 295 on 4 March 2018, 70.0°N, 17.8°W.

The distinct temperature inversion right below 2000 m indicates the top of the boundary layer (Fig. 5.2a). Regions of 100% relative humidity are associated with cloudiness, and are observed just below 1000 m and near the boundary layer top (Fig. 5.2c). This has a high degree of correspondence to the modelled cloudiness from HARMONIE where a low cloud layer is evident over large parts of the Iceland Sea (Fig. 3.3d).

It is worth noting that the dew point temperature (light bue line, Fig. 5.2a) regularly exceeds the air temperature (dark blue line) which results in unrealistically high magnitudes of relative humidity (>100%, Fig. 5.2c). The humidity obtained from the aircraft data may thus not be very accurate (see Sec. 4.1.1).

5.1.2   Flight 298 and 299 (8 March 2018)

Vertical profiles from other flights during 4–9 March have also been investigated. During flight 299, a sawtooth leg was conducted 45 km east of the Greenland coast. The associated potential temperature profiles exhibit an inversion at approximately 250 m height (blue line, Fig. 5.3). An inversion at 530 m was also observed from a flight ascent 15 km further east of the sawtooth leg (red line) during the same flight. Additionally, the potential temperature profile from a descent during flight 298 exhibits an inversion at about 640 m height at a distance of 140 km away from the coast (yellow line).

Other flight profiles indicate inversions at around 1500–2000 m over the ocean (e.g. flight 295, Fig. 5.2a). This confirms that the boundary layer deepens downstream of the sea ice.

These observations are comparable with the results from previous studies by Brümmer (1996) and Hartmann et al. (1999) where the boundary layer thickness was observed to be 100–300 m over the ice, and reached 900–2200 m over the ocean roughly 300 km downwind from the ice edge (see Sec. 2.4.1).

Similar results are also evident from radiosonde observations over the Iceland Sea during the IGP campaign (Sec. 5.2).
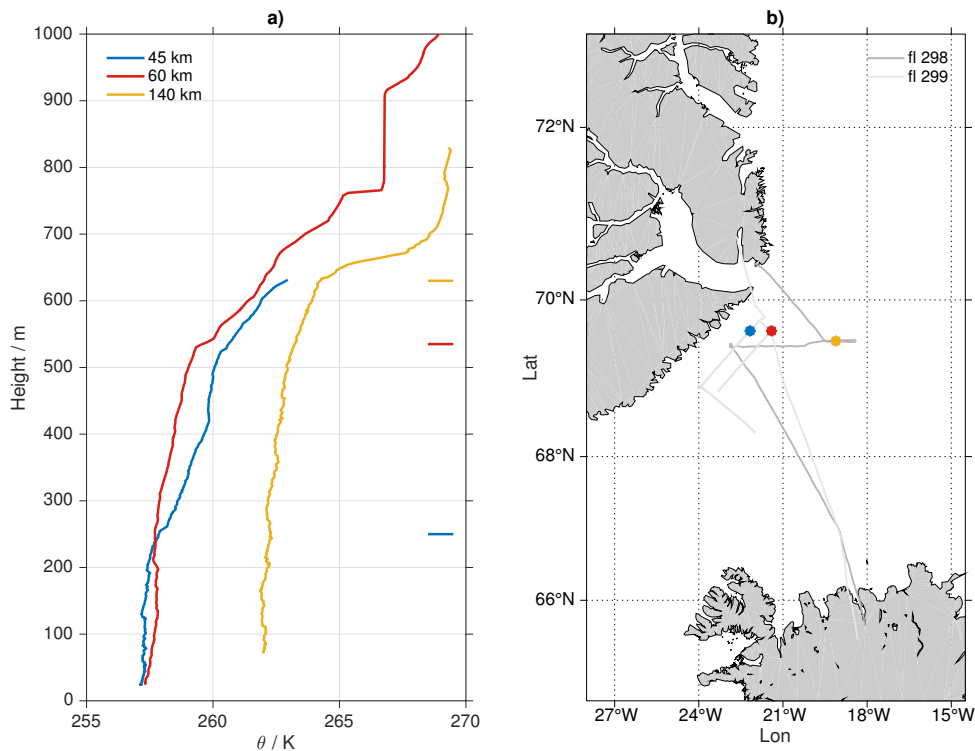

Figure 5.3: a) Vertical profiles of potential temperature θ (K) from aircraft descents and ascents during flight 298 and 299 on 8 March, and b) their positions relative to the Greenland coast. The blue colour represents a descent of the sawtooth leg 45 km from the coast during flight 299, the red; an ascent 60 km from the coast during flight 299, and yellow; a descent 140 km from the coast during flight 298. The approximate heights of the most distinct inversions, referred to in the text, are indicated by lines on the right side of a).

5.2 Radiosonde observations

The radiosonde observations launched from the R/V Alliance during the IGP campaign (Table 4.2, Sec. 4.2) covered the area over the Iceland- and southern Greenland Seas. They provide detailed continuous profiles of the atmosphere, and are, in this study, used to characterize the thermodynamic bulk properties within the boundary layer. For simplicity and relevance, I have chosen to investigate four radiosondes on 4 March due to their convenient positions relative to the Greenland coast and the aircraft mission on this day.

5.2.1 Radiosondes on 4 March 2018

Four radiosondes were released approximately 160 km east of the Greenland coast on 4 March (Fig. 4.3). The first radiosonde was released at 09 UTC and was located furthest east. Each radiosonde was released three hours apart as the ship moved westward, and the last release at 18 UTC was thus closest to the ice edge.

Studying vertical profiles of these zonally aligned radiosondes is useful for analysing how the boundary layer properties, such as height, temperature and humidity evolves moving away from the Greenland coast. The characteristic boundary layer height is indicated by a capping inversion and a sudden drop in humidity. In this case, the boundary layer height is observed to be increasing from a height at approximately 1600 m to 1900 m eastwards (yellow and red lines in Figs. 5.4a,b). This is expected because the surface temperature is observed to increase away from the ice edge, which leads to convection and consequently a boundary layer deepening in this direction. No clear inversion is apparent for the 18 UTC profile (purple line), presumably due to large amounts of mixing throughout the day. An eastward increase in humidity near the surface is also apparent, with values near 1.2 g kg^{-1} for the westernmost radiosonde (purple line) and 1.5 g kg^{-1} for the easternmost radiosonde (blue line) (Fig. 5.4c).
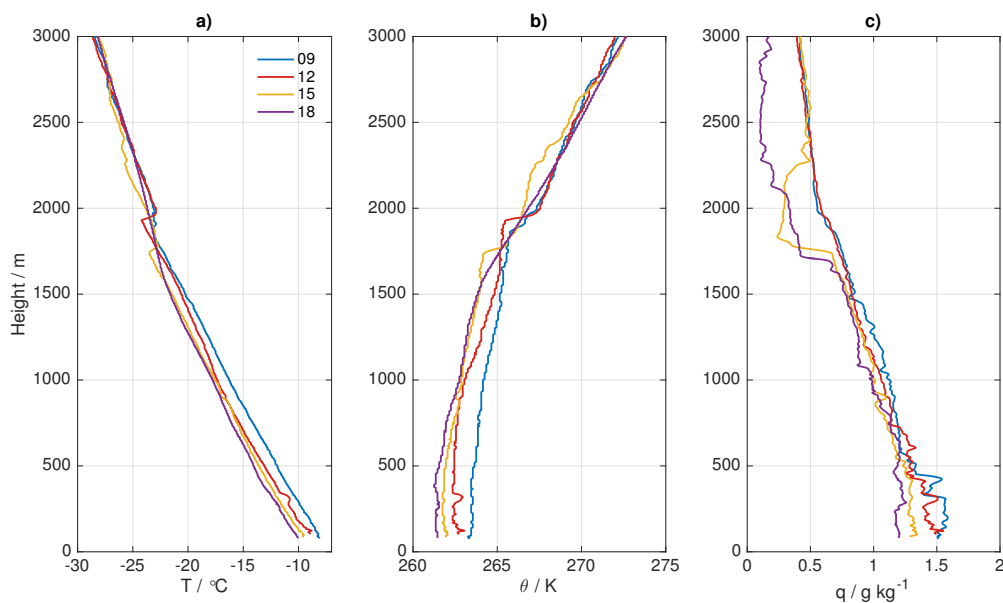

Figure 5.4: Profiles of a) temperature (°C), b) potential temperature (K) and c) specific humidity (g kg^{-1}) on 4 March 2018 09 (blue), 12 (red), 15 (yellow) and 18 (purple) UTC. The radiosondes are aligned from east to west as indicated in Table 4.3.

When investigating the vertical profiles in *skew-T log-P* diagrams, the temperature below 800 hPa is observed to generally follow the dry adiabat (thin blue line, Fig 5.5), indicating a neutral boundary layer. In addition to a temperature inversion, the boundary layer top (∼800 hPa) is characterized by a sudden decrease in dew point temperature (blue line).
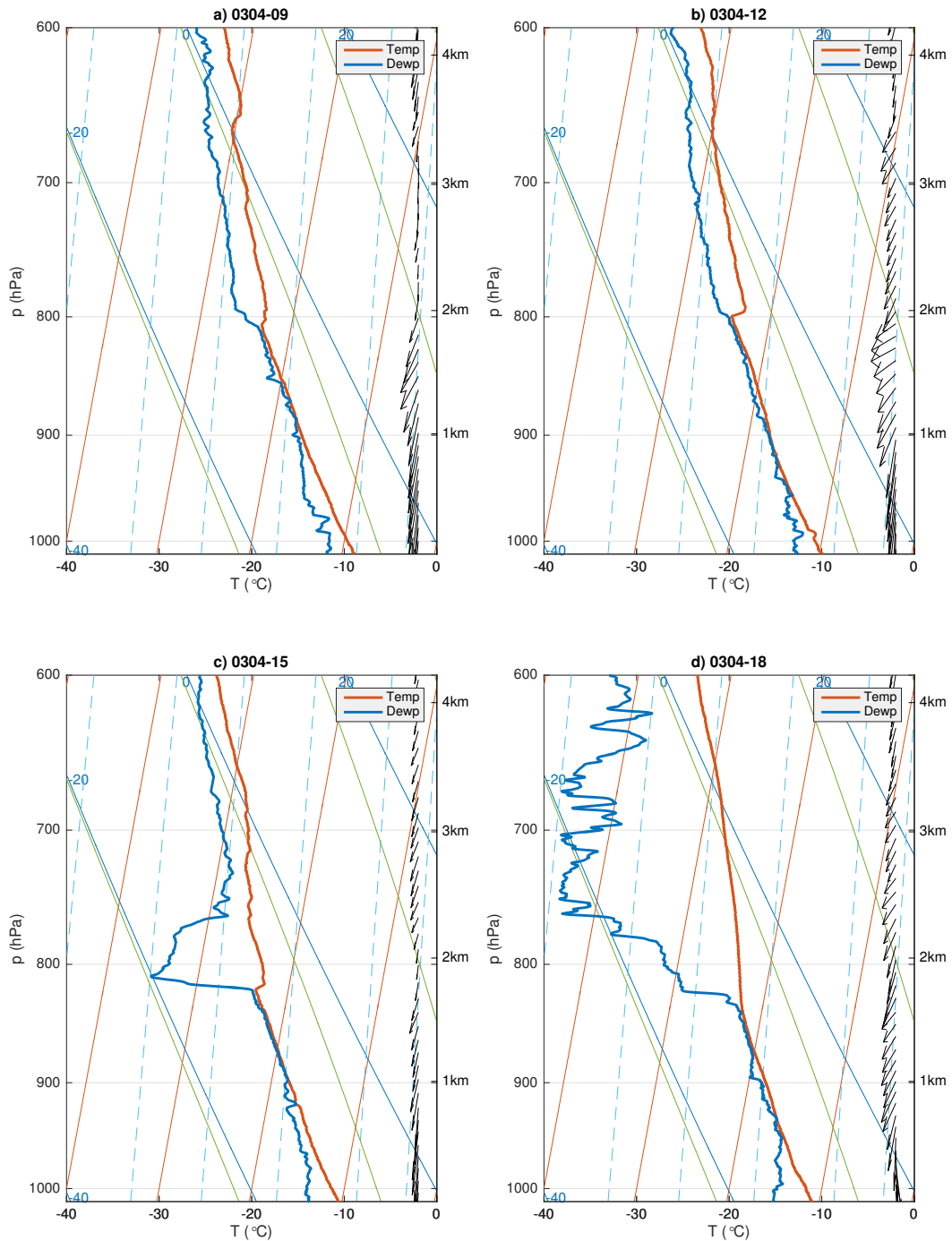

Figure 5.5: Skew-T log-P diagram showing the temperature (red, °C) and dew point temperature (thick blue, °C) with pressure (left axis, hPa) and height (right axis, km), on 4 March 09, 12, 15 and 18 UTC. The diagram includes dry adiabats (thin blue), moist adiabats (green), saturation mixing ratio (blue dashed) and wind barbs.

This decline in dew point temperature indicates a dry atmosphere as the air needs to cool considerably in order to saturate and develop clouds.

The general wind pattern appears to be mainly northerly with an easterly component throughout the tropopause (shown by the wind vectors in Figure 5.5). Since the radiosondes are released three hours apart, and the winds are primarily north-easterlies, it is implied that the analysed air masses are initially aligned in a more north-south direction, rather than west-east. The sampling of the boundary layer development moving away from the Greenland coast will therefore be in the southward direction instead of eastwards. Fortunately, this does not affect the results, as these measured air columns are to a larger degree aligned with the mean flow.

The data from the westernmost radiosonde from 18 UTC deviates from the other radiosondes primarily in two ways; the air above the boundary layer being notably dry, and the surface winds being purely northerly (Fig. 5.5d). The low dew point temperatures are presumably a result of a dry and cold area of origin. A rapid decrease in dew point temperature is also observed from the second westernmost radiosonde (Fig. 5.5c), but at a lesser extent than furthest west. A westward decrease in easterly surface winds is also apparent.

In summary, the weather situation during the IGP campaign was observed to be dominated by a typical weak- to moderate CAO from Greenland. A boundary layer deepening was observed in the downwind direction from the Greenland coast by both aircraft (Fig. 5.3a) and radiosondes (Fig. 5.4b). An increase in temperature and specific humidity within the boundary layer was also observed in this direction (Fig. 5.4). Finally, a notably dry area above the boundary layer top was measured by the radiosondes closest to the ice (Figs. 5.5c,d). The observed thermodynamic behaviour will subsequently be compared with results from the COSMO model (Sec. 5.4 and 5.5). First, the model results will be presented and discussed.

5.3   COSMO model

The COSMO model is primarily used for comparison with the observed situation in order to determine an optimal setup for accurate simulations of water isotopes and the atmospheric water cycle. The following objective is to compare the results of various model setups with radiosonde- and aircraft observations to assess their ability to reproduce the boundary layer characteristics over the Iceland Sea during a cold air outbreak. The initial boundary conditions used in the COSMO model are based on data from the global model ECHAM5-Wiso, nudged to ERA-Interim reanalysis data (Sec. 4.3). The initial situation therefore changes for model runs with different lead times, and the outcomes may end up substantially different.

First, the model was run to simulate the weather situation on 4 March, in coordination with the radiosonde releases during that day. Three simulations were then run, where each simulation was initialised 24 hours apart; run 0200, 0300 and 0400 (see Table 4.4).

On a large scale, all model runs display quite similar behaviour in horizontal moisture distribution with low specific humidity close to the ice edge and a moisture transport through Denmark Strait. However, run 0200 exhibits a distinct cyclonic structure of high humidity at 69°N, 18°W which is not apparent in run 0300 or 0400 (Fig. 5.6).
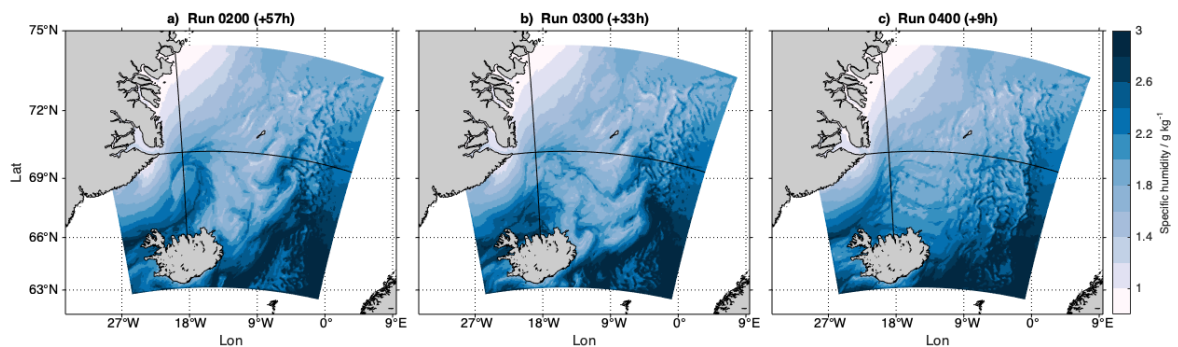

Figure 5.6: Horizontal distribution of 2 m specific humidity (g kg^{-1}) for each model run on 4 March 2018, 09 UTC. Black lines indicate locations of cross-sections used in Figure 5.17.

Since the model had the longest time to adapt with respect to the conditions during the run from 2 March, it is reasonable to presume that this run will be closest to reality. Run 0200 will therefore be further investigated in the following subsections.

5.3.1   COSMO model run 0200

Model run 0200 are used to simulate the weather situation on 4 March 09 UTC, which is 57 hours after the model initialization. The simulation exhibits a high surface pressure over Greenland, and a continuous increase in temperature from about -15 to 2°C in the south-east direction (fig. 5.7) as the atmosphere is heated by the ocean. As seen already in the humidity field, a distinct cyclonic structure also appears around 69°N, 18°W.
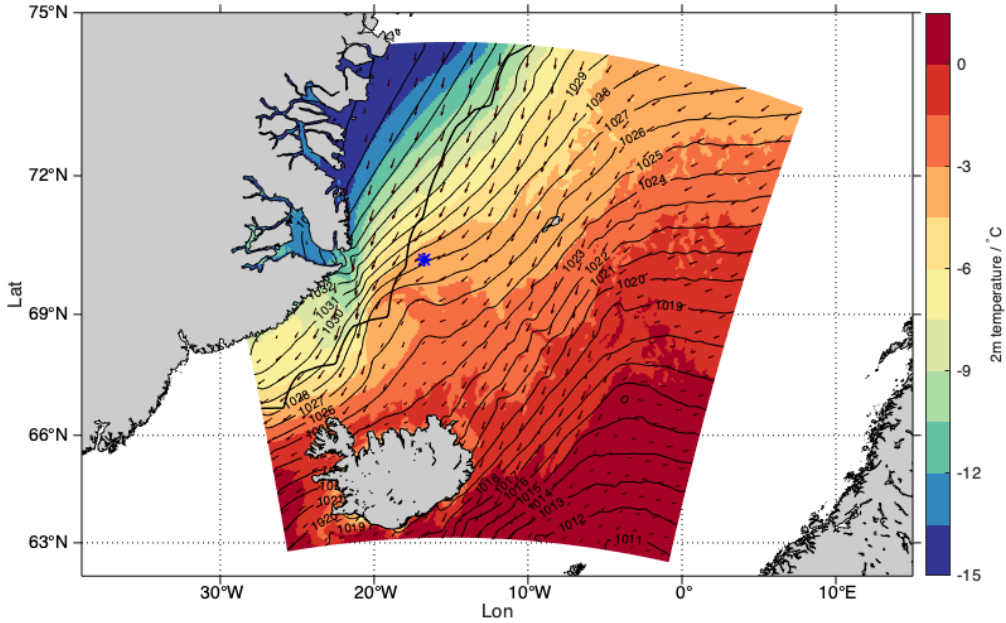
Figure 5.7: Horizontal distribution of 2 m temperature (filled contours, °C), mean sea level pressure (black isobars, contour interval 1 hPa) and 10 m wind (arrows) on 4 March 2018, 09 UTC, from model run 0200 (+57h). The blue star indicates the location of the 09 radiosonde, and the thick black line indicates the ice edge ($T_s = -1.7°C$).

This +57 h model forecast exhibits a weak disturbance in sea level pressure just south of where the radiosonde was released. The thermodynamic properties in the radiosonde area will therefore be mainly influenced by the relatively high temperatures and north-easterly winds associated with the developing cyclone.

Additionally, the cyclone structure is indicated by low boundary layer height (Fig. 5.8a), high specific humidity (Fig. 5.8b) and weak surface sensible heat fluxes (Fig. 5.8c).
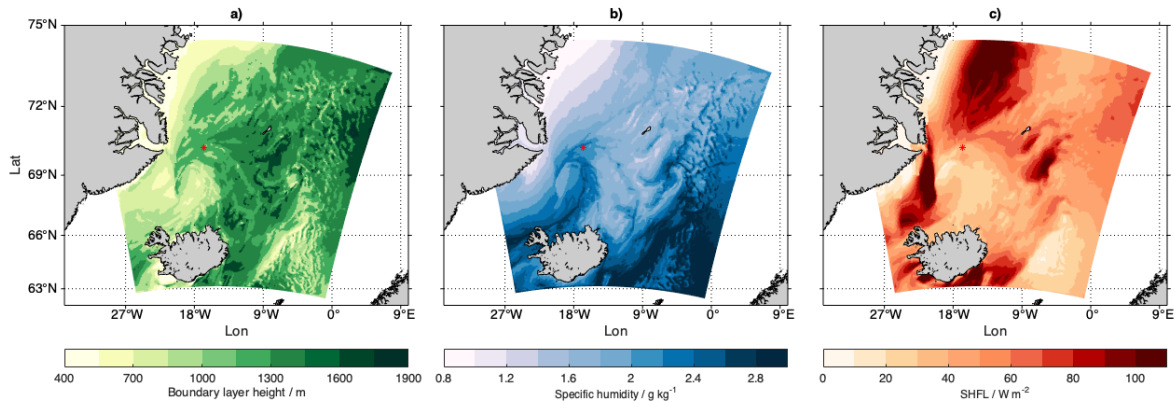

Figure 5.8: Horizontal distribution of a) boundary layer height (m), b) 2 m specific humidity (g kg^{-1}) and c) Surface sensible heat flux (Wm^{-2}) on 4 March 2018, 09 UTC. The red stars indicate the position of the radiosonde release at 09 UTC.

Strong gradients are evident near the Greenland coast, and the cyclonic structure is apparent on all charts. The sensible heat fluxes appear strongest just off the ice edge (>80 Wm^{-2}, Fig. 5.8c) as one would expect during a cold air outbreak. Due to the strong warm air advection of the near surface air in the cyclone area, the surface heat fluxes are reduced in this domain.

However, the satellite image of March 4 (Fig. 1.1) confirms with high precision that the cyclone structure was not observed on this day. Accordingly, run 0200 will not provide an ideal representation of the atmospheric situation during the period of interest since the simulation develops an instability that clearly did not appear in reality. Before finding the optimal lead time to compare with observations, the cyclogenesis during run 0200 will be further investigated to obtain an idea of why the cyclone develops only during this simulation and not the others.

Analysis of the cyclogenesis in run 0200

When studying the instability behind the cyclone in run 0200, it is convenient to compare the thermodynamic properties with a simulation that does not exhibit the same instability. Run 0200 is therefore compared with run 0300, initialised 24 hours after. Both temperature and humidity in the cyclone area appear significantly lower during run 0300 than during run 0200 at 09 UTC on 4 March (Fig. 5.9).
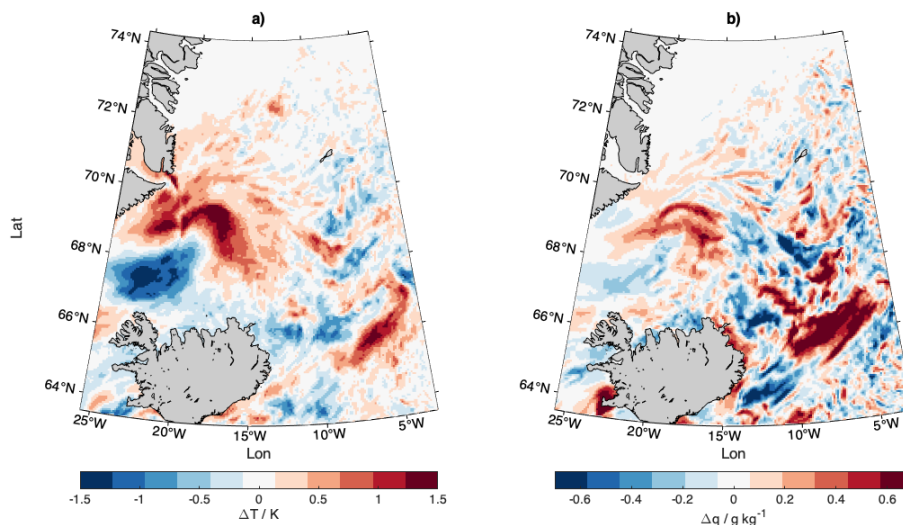

Figure 5.9: Horizontal distribution of a) temperature difference (K) and b) specific humidity difference (g kg^{-1}) between model runs 0200 (+57 h) and 0300 (+33 h) at 900 hPa, on 4 March 09 UTC. Positive values are found where run 0200 is warmer/moister than run 0300.

To detect which processes triggered the cyclone development, various dynamic influences have been studied for both model runs at the specific time when the cyclone appeared to develop, that is 3 March 03 UTC.

First, equivalent potential temperature (θ_e) is investigated since it provides information about static stability and convection as it is a function of both temperature and humidity. At 900 hPa, run 0200 displays a field of significantly high θ_e compared to run 0300, near the area of the developing cyclone (Fig. 5.10a).
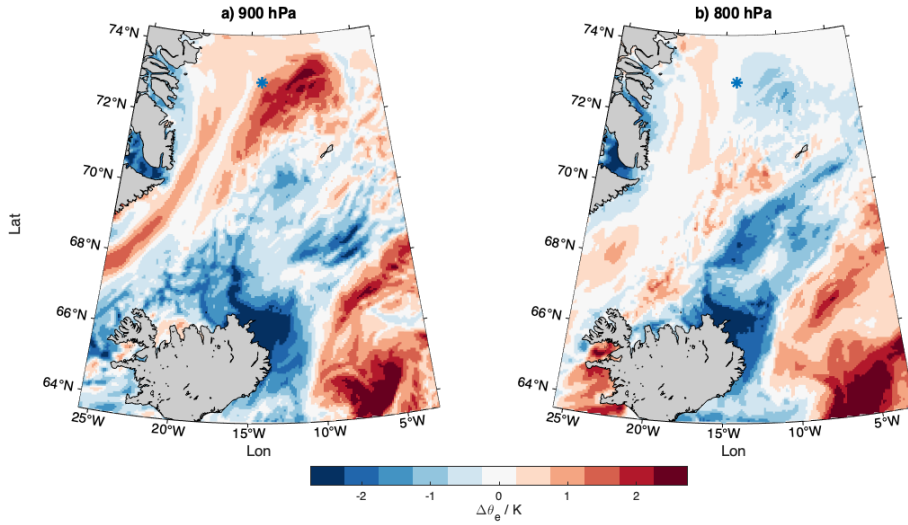
Figure 5.10: Horizontal distribution of equivalent potential temperature difference ($\Delta\theta_e$, K) between model runs 0200 and 0300 at a) 900 hPa and b) 800 hPa, on 3 March 03 UTC. Positive values are found where run 0200 are warmer/moister than run 0300, and the blue star at 73°N, 14°W indicates the approximate location where the cyclone develops first appears at sea level pressure in run 0200. θ_e is calculated from Eq. 4.7.

The field of high $\Delta\theta_e$ is evident around 73°N, 10°W, and implies that run 0200 exhibits significantly high θ_e values in this area compared to run 0300. This distinct difference between the two model runs is however not apparent at 800 hPa (Fig. 5.10b), which implies that the field of excessive temperature and humidity from run 0200 exists mainly within the boundary layer. Additionally, run 0200 displays a field of relatively low static stability in the same area (Fig. 5.11a).
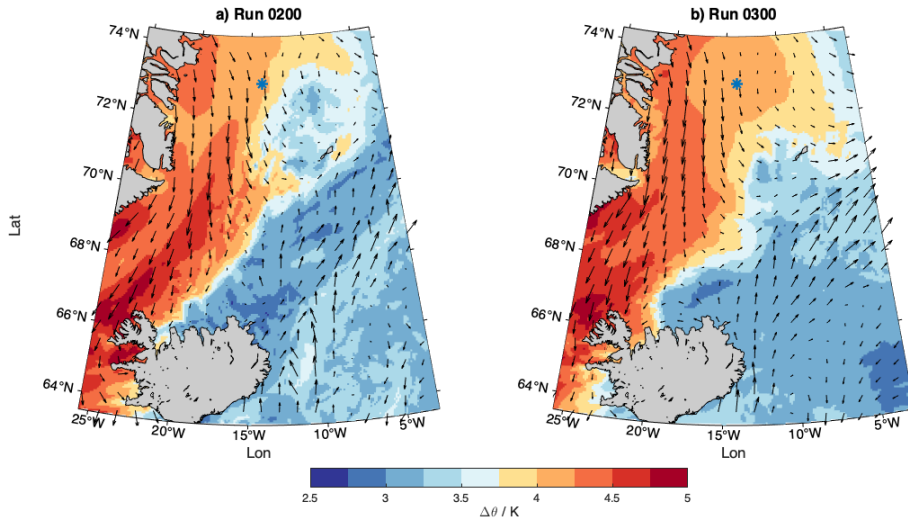

Figure 5.11: Horizontal distribution of the difference in potential temperature ($\Delta\theta$, K) and vertical wind shear (arrows) between 800 and 900 hPa for a) run 0200 and b) run 0300, on 3 March 03 UTC. The blue star at 73°N, 14°W indicates the approximate location where the cyclone first appears at sea level pressure in run 0200. θ is calculated from Eq. 4.6.

The atmosphere between 900 and 800 hPa is naturally most statically stable over the MIZ and near the ice edge for both model runs, with a moderate decrease over the ocean. During model run 0200, a field of relatively low static stability becomes apparent at 72°N, 10°W (Fig. 5.11a). This field of low stability lies approximately in the same area as the field of high θ_e values in Figure 5.10a, and is not apparent in run 0300 (Fig. 5.11b). Hence, it seems reasonable to presume that these characteristic features induced the growth of the pressure disturbance in run 0200. The wind shear in the area of interest seems to be quite similar for the two model runs, and was probably not decisive for the cyclone development.

Relative vorticity was investigated at 800 hPa for the two model runs, where run 0200 exhibited considerably stronger vorticities over the Iceland Sea than run 0300 (Appendix C, Fig C.1). It is worth noting that run 0300 is initialised only 3 hours before the forecast, which seems to be too short time for the model to spin up adequately. Additionally, surface heat fluxes and convective rainfall were investigated. These parameters did however not exhibit any particular notable processes in the area of interest, nor were there any large differences between the two runs (Appendix C, Figs. C.2−C.4).

The main contributors for the cyclone development on 3 March 03 UTC in run 0200 appears to be a combination of long spin-up time and the excessive temperature- and humidity values in the area of the cyclone development (Fig. 5.10a). An unwanted instability therefore develops in the northern part of the model domain, which is not apparent in the other runs with less spin-up time. Furthermore, the transition from the initial large-scale grid spacing to a much finer resolution of 0.05° (Table 4.4) may also have contributed to the instability development.

5.3.2   Fine vs coarse resolution

A study by Pfahl et al. (2012) revealed some pronounced differences between the high-resolution COSMO model and its own initial boundary basis; the coarse-resolution ERA40 reanalysis. A winter storm event in January 1986 was simulated by the COSMO model and compared with ERA40. The simulated temperature structure and sea level pressure were investigated over the US and western North Atlantic, where the COSMO model exhibited a stronger low pressure anomaly than the reanalysis data after five days of the simulation. This is partly due to the much finer resolution, according to Pfahl et al. (2012).
In order to investigate how the small horizontal grid-spacing influences the sensitivity and ability to develop various weather systems, simulations of high-resolution (0.05°) are compared with simulations of much coarser resolution (0.2°).

Run 0200

A comparison between fine and coarse resolution is first made in order to investigate the possibility of the small grid spacing causing the development of the cyclonic structure over the Iceland Sea in run 0200. The fine-resolution simulation of the weather situation from 00 to 18 UTC on 4 March exhibits the development and advection of a cyclone structure north of Iceland and a substantially humid area east of Iceland (Figs. 5.12 a–c). During the corresponding coarse-resolution simulation, the cyclone is slightly less distinct and the humid area east of Iceland is not apparent (Figs. 5.12 d–f).
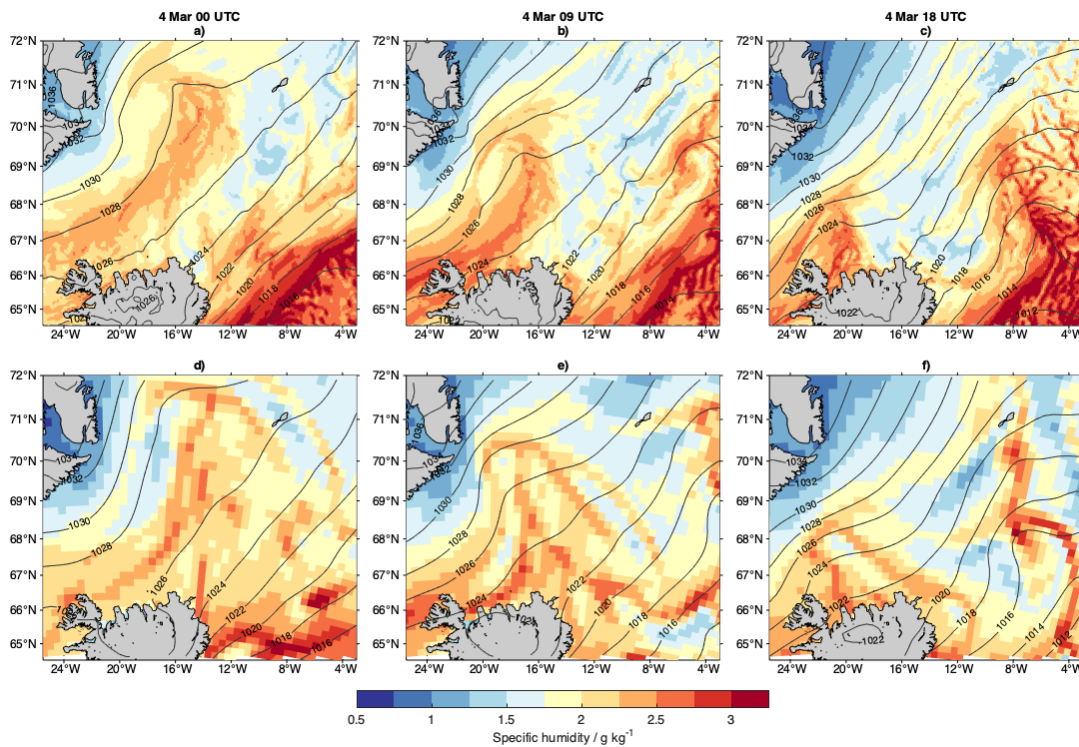
Figure 5.12: 2 m specific humidity (colours, g kg^{-1}) and sea level pressure (isobars, contour interval 2 hPa) over the Iceland Sea on 4 March a,d) 00 UTC (+48 h), b,e) 09 UTC (+57 h) and c,f) 18 UTC (+66 h) from model run 0200 with fine resolution of 0.05° (a–c) and coarse resolution of 0.2° (d–f).

At 00 UTC, a cyclonic structure associated with high humidity develops, and a band of approximately 2.3 g kg^{-1} follows the 1028 hPa isobar (Fig. 5.12a). At 09 UTC, the cyclone is apparent with humidity values of roughly 2.5 g kg^{-1} (Fig. 5.12b). At last, at 18 UTC, the cyclone has advected southward, and the pressure gradient is slightly sharper for the high-resolution run than for the coarse-resolution run (Figs. 5.12 c,f).

The spatial variability of the humidity fields is noticeably smaller in the coarse-resolution run due to the larger grid spacing. However, the humidity values within the cyclone appear generally similar as those of fine resolution. Increasing the grid spacing for run 0200 did therefore not seem to reduce the spin-up problems that caused the cyclone development to a great extent. This instability therefore appears to develop from the combination of long spin-up time and the high temperatures and humidity values in the development area (as discussed in Section 5.3.1). However, the coarse resolution managed to exclude the field of excessive specific humidity east of Iceland.

Run 0300

Additionally, a simulation of coarse resolution initialised on 3 March 00 UTC was run and compared with the corresponding fine-resolution run 0300. Unlike the vague contrasts between the simulations of fine and coarse resolution from 2 March 00 UTC, clear differences are visible between the simulations from 3 March 00 UTC (Fig. 5.13).
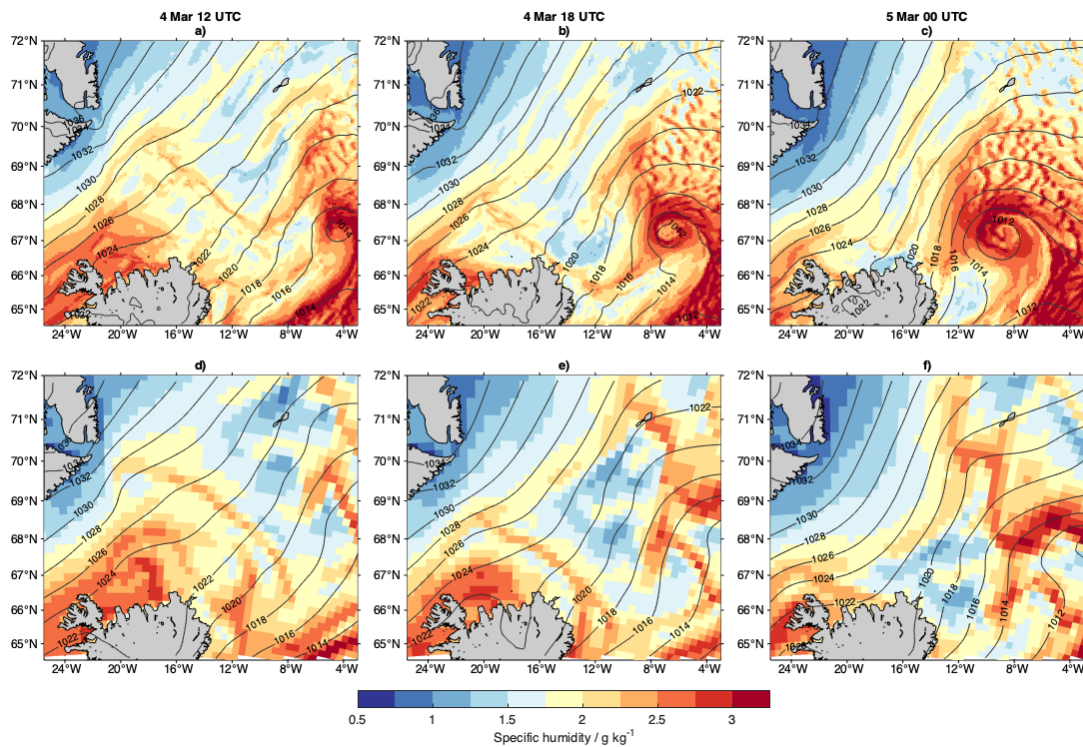
36

Figure 5.13: 2 m specific humidity (colours, g kg^{-1}) and sea level pressure (isobars, contour interval 2 hPa) over the Iceland Sea on a,d) 4 March 12 UTC (+36 h), b,e) 4 March 18 UTC (+42 h) and c,f) 5 March 00 UTC (+48 h) from model run 0300 with fine resolution of 0.05° (a–c) and coarse resolution of 0.2° (d–f).

During the high-resolution run for the period from 4 March 12 UTC to 5 March 00 UTC, a distinct low pressure system spins up in the eastern part of the domain (Figs. 5.13 a–c). This does not occur during the coarse-resolution run (Figs. 5.13 d–f).

This cyclone is considerably more intense than the developing cyclone in run 0200. The system in run 0300 displays a sea level pressure of 1012 hPa and humidity values of more than 3 g kg^{-1} (Fig. 5.13b), compared with the system in run 0200 which exhibits a sea level pressure of 1026 hPa and a humidity maximum of approximately 2.5 g kg^{-1} (Fig. 5.12b).

This low pressure system from run 0300 is not apparent in any satellite images (e.g. Fig. 1.1) or in the simulation of coarser resolution. This confirms the theory that the transition from the coarse initial boundary data (ECHAM5-Wiso) to the high resolution of 0.05° is likely to cause spin-up problems resulting in unanticipated instabilities and a subsequent low pressure system.

The simulation is highly flawed due to the development of this intense low pressure system. However, the cyclone lies at 67°N, 7°W at 18 UTC and does not appear to influence the radiosonde area around 70°N, 17°W.

Even though both run 0200 and 0300 develop unanticipated weather systems, they will be further compared with run 0400 and radiosonde observations in order to determine the optimal lead time. The optimal lead time will be based on the simulation correspondence with observed data.

5.3.3   COSMO model runs 0200, 0300 and 0400

To investigate the model accuracy, profiles of temperature and humidity from the three fine-resolution model runs have been compared with the corresponding radiosonde observation from 4 March 09 UTC (Fig. 5.14).

The observed temperature in this location appeared to gradually decrease with height, with a distinct inversion at 800 hPa indicating the top of the boundary layer (black line, Fig. 5.14a). The potential temperature profile indicates a more or less neutral boundary layer, with constant values of about 264–265 K up to the capping inversion (Fig. 5.14b). The specific humidity was also observed to gradually decrease upwards, with values around 1.5 g kg^{-1} near the surface and 0.5 g kg^{-1} near, and above, the boundary layer top (Fig. 5.14c).
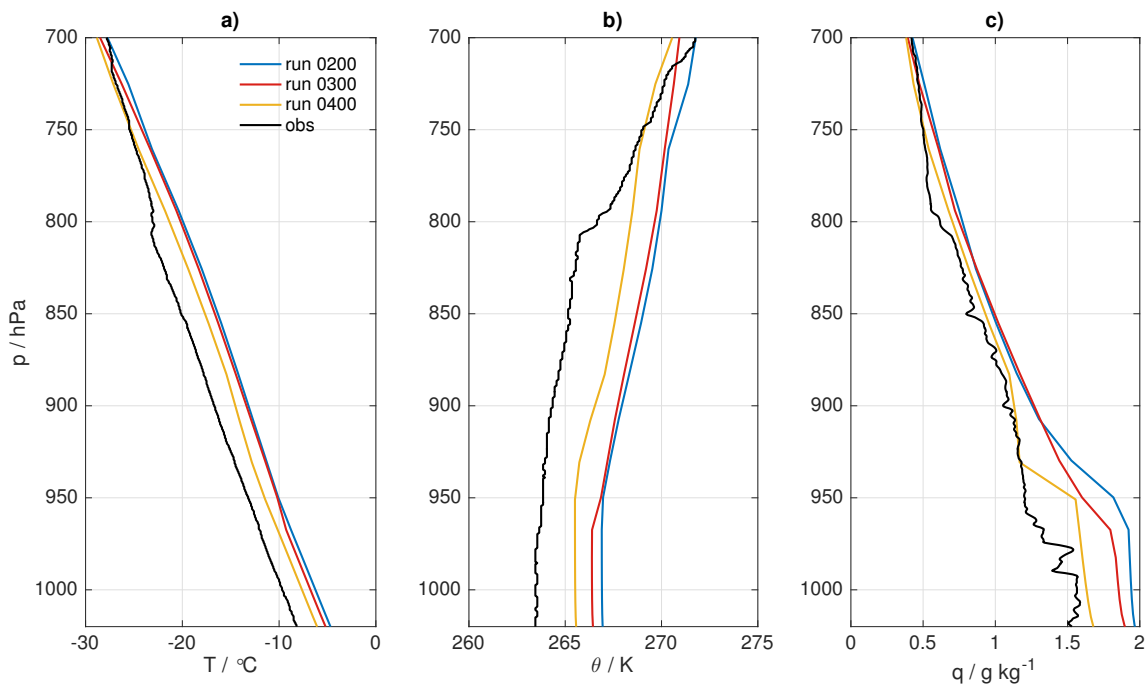

Figure 5.14: Vertical profiles of a) temperature (°C), b) potential temperature (K) and c) specific humidity (g kg^{-1}) up to 750 hPa, from model run 0200 (blue), run 0300 (red), run 0400 (yellow) and the observed situation from a radiosonde (black) on 4 March 2018 09 UTC, 70.25°N, 15.78°W.

All model runs represent a warmer and moister boundary layer than the observed situation. Run 0200 (blue line) appears to be furthest from reality in the entire boundary layer, as it is consistently warmer and moister than the observations and the two other runs. The observed surface temperature was −8.5°C, compared to −5°C for run 0200. This 3.5 K bias is evident throughout the entire boundary layer (Table 5.1). In addition, the humidity at the surface was observed to be 1.5 g kg^{-1} where the three model runs have offsets of roughly 0.2, 0.4 and 0.5 g kg^{-1} respectively (Fig. 5.14c, and Table 5.1). All runs also seem to lack the distinct inversion at 800 hPa, which is prominently present in the observed radiosonde profile.

Table 5.1: Mean temperature (T)- and humidity (q) bias betewen the three model runs and the corresponding radiosonde on 4 March 2018 09 UTC. The bias is calculated within the boundary layer (up to 800 hPa) and at the surface (by Eq. 4.8).

	< 800 hPa		Surface	
Run	T (K)	q (g kg^{-1})	T (K)	q (g kg^{-1})
0200	3.5	0.29	3.6	0.47
0300	3.2	0.24	3.2	0.41
0400	2.1	0.10	2.3	0.18

The skill of the model forecasts evidently degrades with increasing lead time. Run 0400 appears to have the best correlation with observations with a temperature bias of 2.1 K and humidity bias of 0.10 g kg^{-1} throughout the boundary layer. In comparison, run 0200 presents biases of 3.5 K and 0.29 g kg^{-1}.

Furthermore, the simulated horizontal winds have been compared with radiosonde observations. It is primarily evident that all model runs exhibit a far stronger easterly surface wind than observed (Fig. 5.15a). The observed horizontal wind near the surface was almost purely northerly, with a zonal component of about 2 ms^{-1} westward and a meridional component of 17 ms^{-1} southward (black line, Figs. 5.15a,b). The winds appeared to decrease up to 750 hPa (right above the boundary layer top), where the zonal and meridional components reached values of 0 and -4 ms^{-1} respectively.
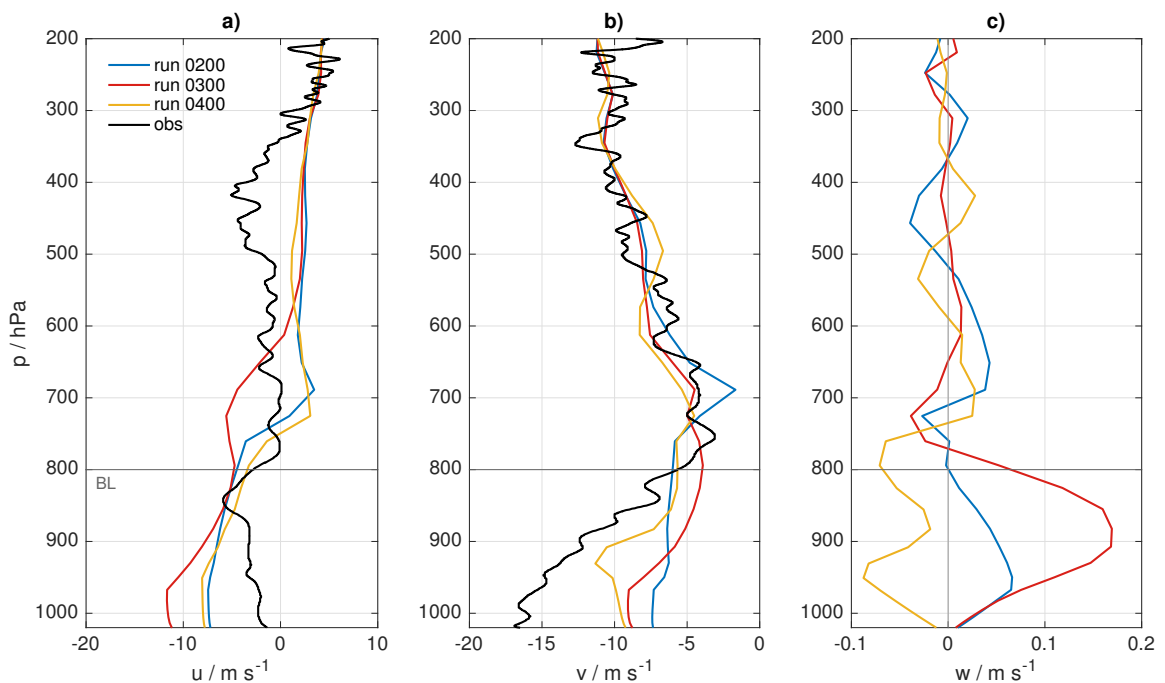

Figure 5.15: Vertical profiles of a) zonal (u), b) meridional (v) and c) vertical (w) wind speed (ms^{-1}) from model run 0200 (blue), run 0300 (red) and run 0400 (yellow) on 4 March 2018 09 UTC, 70.25°N, 15.78°W. The observed horizontal wind speeds from the corresponding radiosonde are shown in black (a,b), and the boundary layer top is indicated at 800 hPa in all panels.

For all model runs, the zonal wind component (Fig. 5.15a) changes direction from easterly (negative) to westerly (positive) between 750 and 610 hPa, while the observed wind is easterly (or zero) up to 340 hPa. Run 0200 (blue line) and 0400 (yellow line) exhibit a 6 ms^{-1} stronger surface wind speed than observed, while run 0300 (red line) has a more extreme offset of approximately 10 ms^{-1}. The overall structures of the model profiles are not particularly similar to the observations.

The simulated meridional wind component (Fig. 5.15b) is more similar to the observations in structure up to 200 hPa. However, the model represents much weaker northerly wind speeds near the surface than what was observed. Model run 0200 exhibits a northerly surface wind speed of 7 ms^{-1}, while the radiosonde observed much stronger 17 ms^{-1}. This indicates that the winds are modelled to be far more easterly than observed.

The vertical wind component (Fig. 5.15c) is difficult to evaluate since it has not been observed by the radiosonde, and the different runs do not appear to agree on either speed or direction. Run 0400 suggests a downward motion in the entire boundary layer (below 800 hPa), while both run 0200 and 0300 represent an upward motion. Run 0300 doubtlessly exhibits the strongest vertical winds within the boundary layer with speeds up to 0.17 ms^{-1}. However, this is of limited significance considering the relatively low magnitudes.

Generally, the simulated winds have a larger easterly component than observed, and the air is thus originating further east than in reality. The air properties in this north-eastern area of origin are typically associated with higher temperature- and humidity values than further west (closer to Greenland), which explains the excessive simulated temperature- and humidity values (Fig. 5.14). Accordingly, the air-sea temperature contrasts faints, and the surface heat fluxes become weaker with north-easterly flow than with pure northerly flow. One can also observe the air within the boundary layer originating in the north-east from the modelled trajectories (Fig. 5.16).
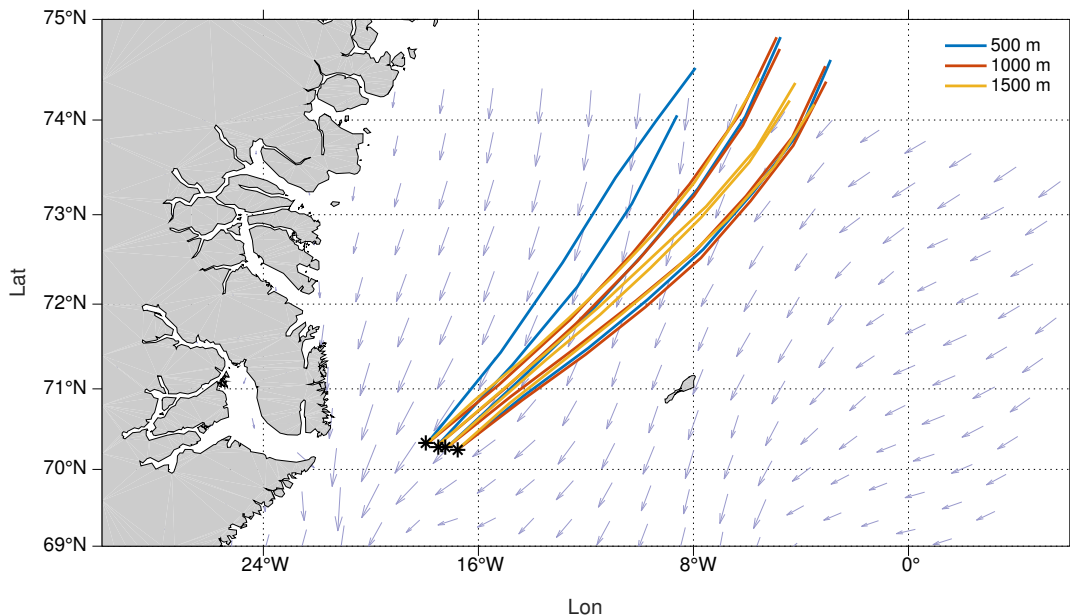

Figure 5.16: Simulated trajectories 48 hours back in time from each radiosonde-location (black stars) at 500 m (blue), 1000 m (red) and 1500 m (yellow), and 10 m wind (vectors) from model run 0200 on 4 March 2018 09 UTC.

Furthermore, the boundary layer heights retrieved from the three runs have been compared. They do not correlate perfectly, but a similar behaviour is apparent in the general structure near the Greenland coast, namely a boundary layer deepening (Fig. 5.17).

Along the zonal line (see Fig. 5.6), the boundary layer height increases from 500 m to 1200 m for all runs along a distance of 3 degrees longitude, which corresponds to approximately 115 km at this latitude (from -22 to $-19°$E, Fig. 5.17a). Similarly, a boundary layer deepening from 400 m to 1000 m occurs from the Greenland coast at 74°N southward to 72°N (Fig. 5.17b).
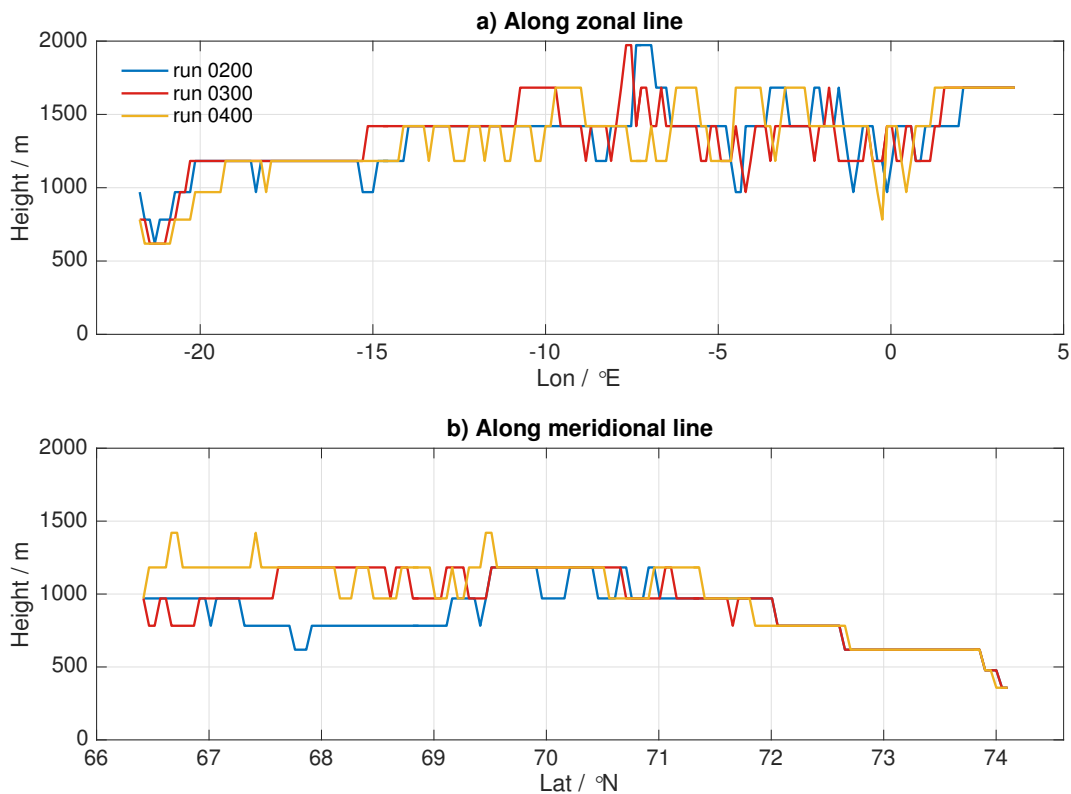

Figure 5.17: Boundary layer height (m) along a) the zonal line and b) the meridional line indicated on the maps in Figure 5.6 from model run 0200 (blue), run 0300 (red) and run 0400 (yellow) on 4 March 09 UTC. The ice edge is located $-22°$E in a) and 74°N in b).

When comparing the observed inversion heights from the radiosonde profiles with the corresponding boundary layer heights from the model simulations, it is immediately clear that each simulation underestimates the general boundary layer depth over the ocean (Table 5.2). The observed boundary layer height z_i mainly increases eastward, despite a 100 m decrease furthest east. Accordingly, the simulated boundary layer is consistently lower than observed, with heights of 1–1.4 km compared to 1.6–2 km observed by the radiosondes.

Table 5.2: Observed boundary layer heights z_i (km) from each radiosonde on 4 March (estimated from Figure 5.5), and the biases for each simulation. Negative biases indicate underestimation by the model.

UTC	Lat (°N)	Lon (°W)	z_i (km)	Bias from obs. (km)		
				run 0200	run 0300	run 0400
09	70.3	16.8	**1.9**	-0.7	-0.7	-0.7
12	70.3	17.2	**2.0**	-1.0	-1.0	-0.8
15	70.3	17.5	**1.8**	-0.6	-0.6	-0.6
18	70.3	17.9	**1.6**	-0.6	-0.6	-0.4
Average				-0.7	-0.7	-0.6

The precision of the model evidently increases throughout the day for all model runs. However, an overall degradation in model skill is prominent over time (Tables 5.1 and 5.2), at which the optimal lead time for the 4 March forecast is from 4 March 00 UTC. It is therefore reasonable to assess an optimal lead time of +9 to +18 h for further comparison with radiosonde- and aircraft observations.

5.4   Model compared with radiosondes

When investigating the model's ability to reproduce the boundary layer modifications during a cold air outbreak, it is necessary to compare the model results to the observed situation. First, vertical cross-sections from the four radiosondes on 4 March are presented and compared with model run 0400 during the period from 09 to 18 UTC. During this simulation, a field of relatively high humidity is most distinct near the radiosonde area at 09 UTC. Accordingly, the air is advected south-westward along the 1028 hPa isobar during the following nine hours (Fig. 5.18). The simulation represents both temperature and humidity quite well along the cross-section, with a slight overestimation of surface temperature furthest east, and a slight overestimation of humidity above 800 hPa furthest west (Fig. 5.19).
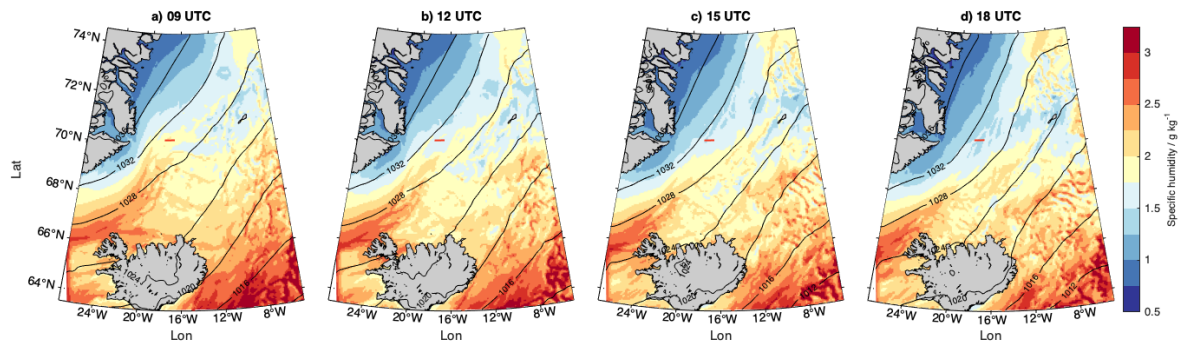

Figure 5.18: Evolution of 2 m specific humidity (g kg^{-1}) and mean surface pressure (black isobars, contour interval 4 hPa) on 4 March 2018 a) 09 UTC, b) 12 UTC, c) 15 UTC and d) 18 UTC, by model run 0400. The red lines indicate the location of the cross-section of radiosondes (Fig. 5.19).
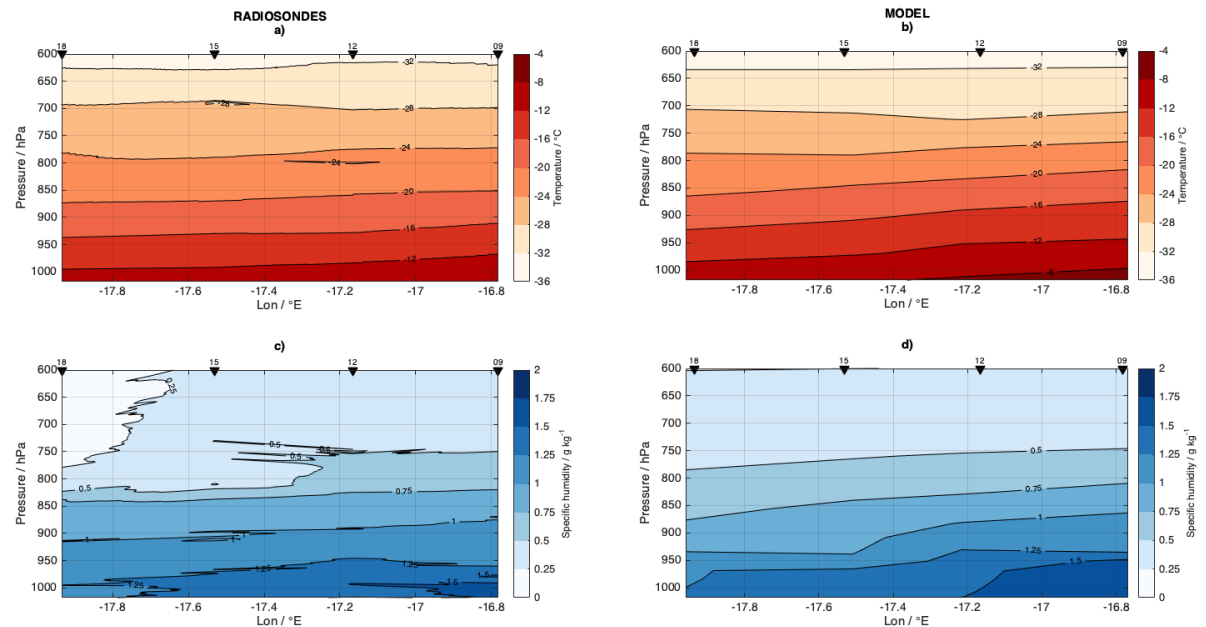

Figure 5.19: Cross-sections of temperature (red, °C) and specific humidity (blue, g kg^{-1}) from a,c) radiosondes and b,d) model run 0400, along the section of radiosondes from 17.93°W to 16.78°W, on 4 March 2018 09 to 18 UTC. The leftmost values are from 18 UTC and the rightmost values from 09 UTC in all panels.

43

Since there are three hours between the radiosonde releases, the modelled cross-sections have been presented the same way, with easternmost values from 09 UTC and westernmost values from 18 UTC.

The general structure of temperature and humidity looks fairly similar for the observed and modelled situations. However, the easternmost surface values for both temperature and humidity are slightly higher in the model than observed. Furthest east (09 UTC), the 1000 hPa temperature and humidity values are exceedingly $-8°C$ and 1.6 g kg^{-1} for the model (Figs. 5.19b,d), compared with $-10°C$ and 1.5 g kg^{-1} observed by the radiosondes (Figs. 5.19a,c). At the westernmost point (18 UTC), the temperatures are nearly perfectly represented, while the simulated specific humidity is still considerably overestimated, especially above 800 hPa (Figs. 5.19d and 5.20b). The simulated temperatures are consistently overestimated in the boundary layer (below 800 hPa), while an underestimation is found above (Fig. 5.20a).
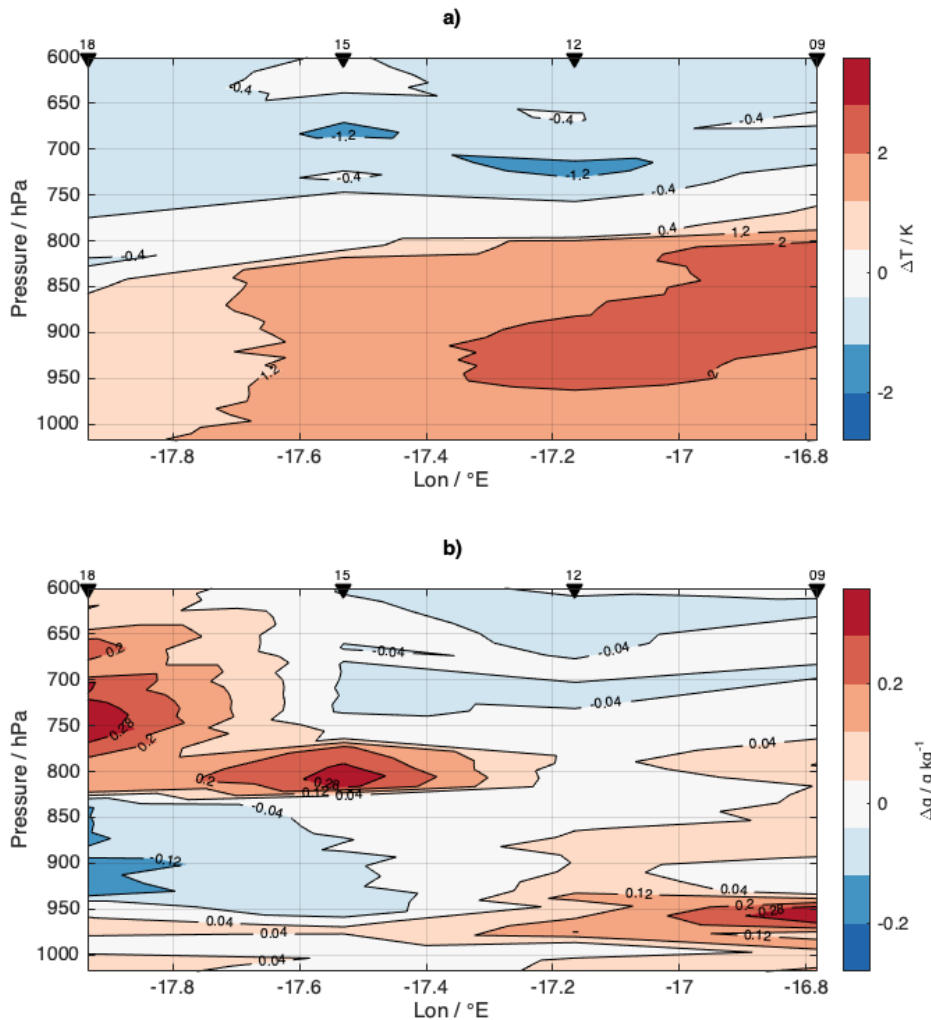

Figure 5.20: Cross-section of the a) temperature difference (K) and b) specific humidity difference (g kg^{-1}) between model run 0400 and radiosondes (Fig. 5.19). Positive values are found where the model is warmer/more humid than observed by radiosondes. Similar plots for run 0200 and 0300 (fine and coarse res.) are given in Appendix D.

The model also appears to have largest offsets from the easternmost radiosonde with biases up to 2 K and 0.3 g kg^{-1}. As the field of high humidity in the model advects away from the radiosonde area (Fig. 5.18), the mean bias between model and observation decreases. The representation of temperature clearly increases in accuracy with time (Table 5.3). However, the mean humidity bias behaves slightly different.

Table 5.3: Mean temperature (T)- and humidity (q) bias betewen model run 0400 and the four radiosondes on 4 March 2018 09, 12, 15 and 18 UTC respectively. The bias is calculated from the ground to 600 hPa (by Eq. 4.8).

UTC	Lat (°N)	Lon (°W)	Bias T (K)	Bias q (gkg^{-1})
09	70.3	16.8	0.8	0.06
12	70.3	17.2	0.6	0.01
15	70.3	17.5	0.5	0.01
18	70.3	17.9	0.2	0.11
Average			0.5	0.05

The humidity in the model does not include the dry area observed above 800 hPa (Fig. 5.19c) which causes the sufficiently large mean bias of 0.11 g kg^{-1} for the 18 UTC humidity measure.

Data from the four radiosondes were also compared with run 0200 and run 0300 (fine and coarse res.) in order to evaluate their accuracy relative to run 0400 (Appendix D). The biases and root mean square errors (RMSE), averaged from 4 March 09, 12, 15 and 18 UTC, have therefore been calculated for all simulations, and it is again confirmed that run 0400 provides the best representation of the weather situation on 4 March 09–18 UTC (Tables 5.4 and 5.5).

Table 5.4: Temperature (T)- and humidity (q) bias averaged from 4 March 09, 12, 15 and 18 UTC for all model runs. The bias is calculated from the ground to 600 hPa (by Eq. 4.8).

Model run	Bias T (K)		Bias q (g kg^{-1})	
	fine res.	coarse res.	fine res.	coarse res.
0200	1.2	1.2	0.11	0.12
0300	1.0	1.0	0.08	0.09
0400	0.5	-	0.05	-

Table 5.5: Root mean square error (RMSE) of temperature (T) and humidity (q) averaged from 4 March 09, 12, 15 and 18 UTC for all model runs. The RMSE is calculated from the ground to 600 hPa (by Eq. 4.9).

Model run	RMSE T (K)		RMSE q (g kg^{-1})	
	fine res.	coarse res.	fine res.	coarse res.
0200	1.9	2.1	0.19	0.22
0300	1.7	1.9	0.16	0.20
0400	1.2	-	0.12	-

5.5   Model compared with aircraft observations

I have used data from two aircraft missions, flight 295 on 4 March and flight 299 on 8 March, to further investigate the model's ability to simulate the thermodynamic properties within the boundary layer. Hence, the observations from these two flights are compared with the fine-resolution model simulations initialised at 4 March 00 UTC and 8 March 00 UTC respectively (see Table 4.4).

5.5.1   Flight 295, 4 March

In addition to several radiosonde releases on 4 March, a research flight (flight 295) was conducted from 10 to 15 UTC, northward from Akureyri to 70.2°N and back (see Sec. 5.1). Vertical profiles of temperature T, potential temperature θ and specific humidity q from the flight descent, at approximately 70°N, are compared with radiosonde- and model data from the same location and time (Fig. 5.21). The temperature correspondence is quite high between radiosonde (blue line) and aircraft (red line), with a difference of approximately 1 K within the boundary layer and a distinct inversion at 800 hPa (Figs. 5.21a,b). The flight descent is located slightly closer to the ice edge than the simultaneous radiosonde release, which explains the slightly lower temperatures (see Fig. 4.3). The simulated temperature profile (black line) exhibits a warm bias of about 2–3 K within the boundary layer (Fig. 5.21a). Furthermore, the specific humidity measured from the aircraft appears quite erroneous when compared with radiosonde- and model data (Fig. 5.21c). This inconsistency is presumably due to errors in the Buck cooled mirror instrument, as discussed in Section 4.1.1.
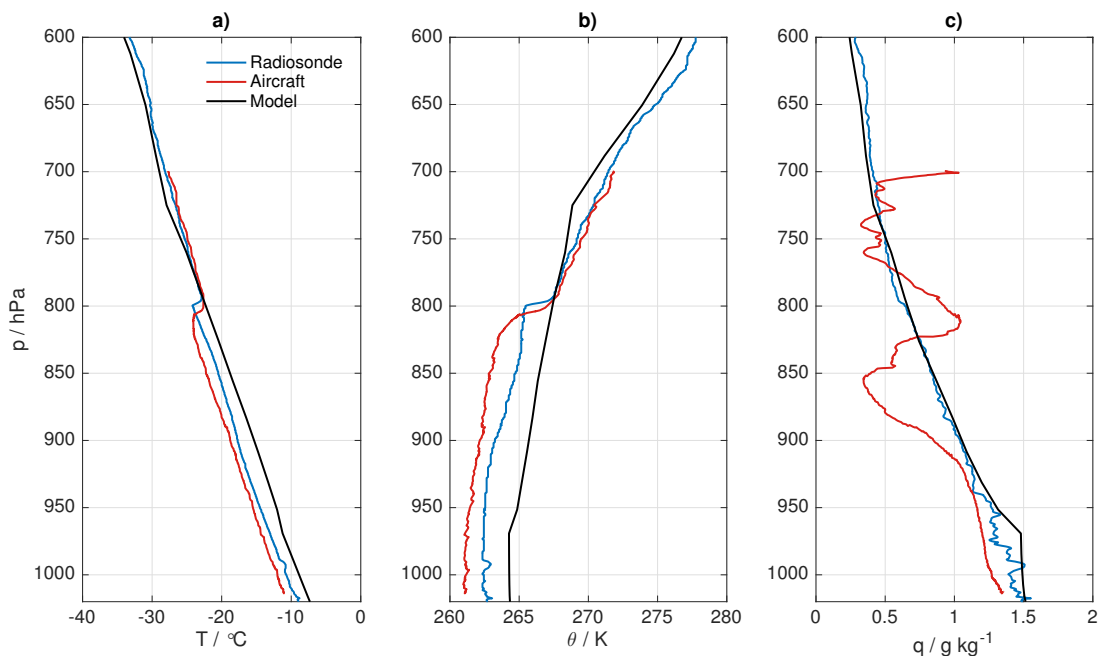

Figure 5.21: Vertical profiles of a) temperature (°C), b) potential temperature (K) and c) specific humidity (g kg^{-1}) from radiosonde data (blue), aircraft data (flight 295, red) and model data (run 0400 (+12h), black) on 4 March 12 UTC, 70°N, 17°W.

46

Observations along the flight track of flight 295 are compared with the corresponding model results from run 0400, which is initialised approximately 12 hours before the flight. The simulated temperature and specific humidity at 900 hPa gradually decreases northward, with a field of higher humidity located west of the flight path (Fig. 5.22b).
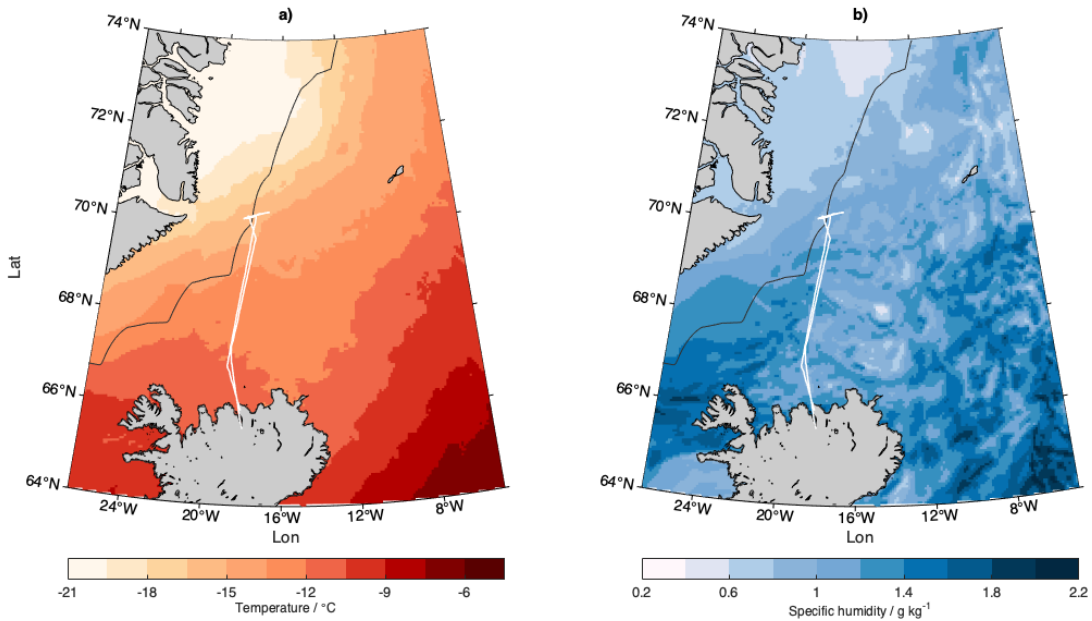

Figure 5.22: Aircraft flight track from flight 295 (white line) and the horizontal distributions of a) 900 hPa temperature (°C) and b) 900 hPa specific humidity (g kg^{-1}) by model run 0400 (+12h) on 4 March 2018 12 UTC (filled contours). The thin black line indicates the ice edge, defined as the contour where $T_s = -1.7$°C.

Transit flying was first conducted at 700 hPa height to 70°N. Then low level flying, including a short sawtooth leg, was carried out along the leg furthest north in coordination with the ship. The simulated temperatures and specific humidity values range from -10 to -16°C (Fig. 5.22a) and 1 to 1.4 g kg^{-1} (Fig. 5.22b) along the flight path at 900 hPa.

When vertical cross-sections from flight 295 are compared with model run 0400, the vertical humidity gradient appears stronger in the model than the aircraft observations. Consequently, the model underestimates the humidity in the upper levels while the near-surface layer appears more accurately represented (Fig. 5.23b). Based on the comparison with radiosonde- and model data (Fig. 5.21c), this behaviour was not expected as the model- and radiosonde profiles exhibited higher humidity values than the aircraft up to 820 hPa. The observed temperature along the flight path corresponds very well to the modelled situation within the lower boundary layer, but a slight overestimation by the model is found in the area where the aircraft performs the sawtooth pattern at 68–69°N (Fig. 5.23a). Additionally, as mentioned above, the simulated specific humidity appears too low when compared with the aircraft observations. This underestimation of specific humidity contradicts the previous comparisons between model and observations (Sec. 5.4) since the model typically exhibits a too moist boundary layer (Fig. 5.20b).
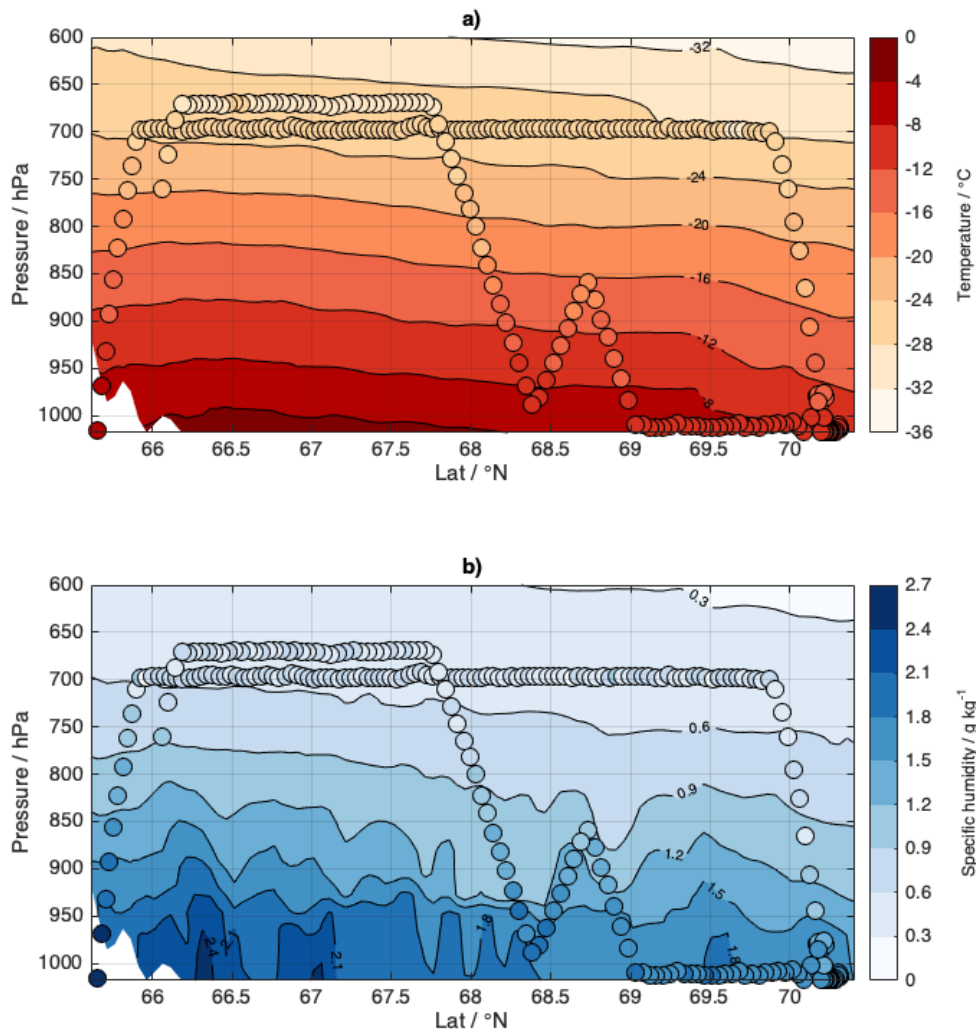
Figure 5.23: Cross-sections of a) temperature (°C) and b) specific humidity (g kg^{-1}) from model run 0400 (+12h) along the flight path indicated on the maps in Figure 5.22, on 4 March 2018 12 UTC. Observed values each minute from flight 295 are indicated as filled circles over the modelled simulation.

5.5.2   Flight 299, 8 March

On 8 March, flight 298 and 299 were conducted, with a refuel break at Constable Point (CP) in Greenland. The weather situation was quite favourable during this mission, with a shallow cloud layer near the ice and clear weather in Greenland (Sec. 3.1)
Flight 299 was directed southward from CP, where three sawtooth legs and three low level legs were conducted near, and over, the ice. A noticeable temperature gradient is observed along the first sawtooth leg at 15 UTC (highlighted in Fig. 5.24).
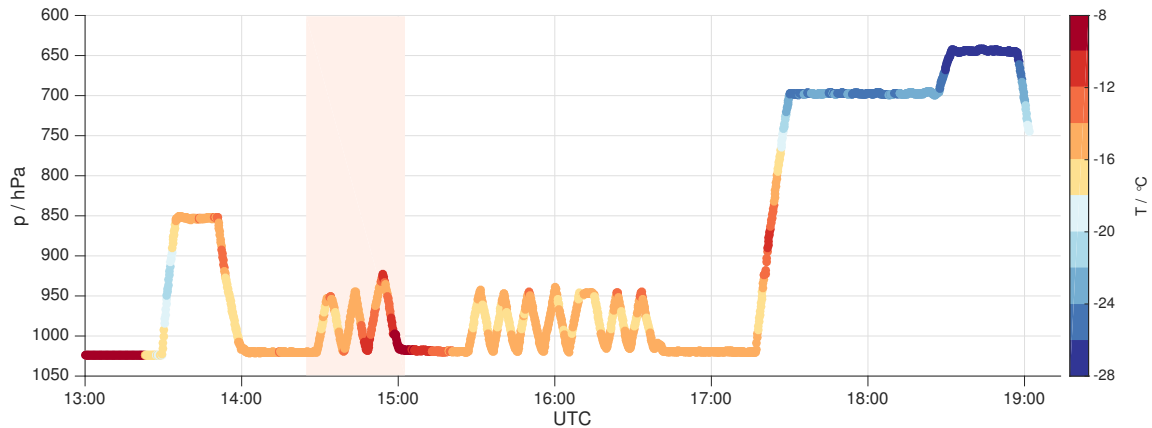

Figure 5.24: Evolution of air pressure (hPa) and air temperature (°C) during flight 299 on 8 March 2018. The aircraft was flying southward from Greenland to Akureyri, at which the sawtooth legs were conducted over the MIZ. The horizontal flight pattern is illustrated in Figure 4.2d.

The first ascent at 13:30 UTC exhibits an inversion at approximately 920 hPa, indicating a boundary layer height of roughly 800 m. In addition, an inversion at 870 hPa ($\sim$1200 m height) is evident along the last ascent at 17:20 UTC, which is located a few degrees south-east.

The performance of sawtooth patterns enables the possibility of retrieving vertical atmospheric cross-sections along the legs. The first sawtooth leg was perpendicular to the Greenland coast, and has thus been selected for comparison with the COSMO model at 15 UTC along the same cross-section (69.0°N, 23.8°W to 68.3°N, 21.8°W).
For the simulations on 4 March, a lead time of +9 to +18 h was deemed optimal (Sec. 5.3.3). A simulation with 15 h lead time was therefore run, in order to compare with the aircraft observations from flight 298 on 8 March 15 UTC (model run 0800, Table 4.4). The observed temperature gradient at the end of the sawtooth leg (highlighted in Fig. 5.24) is also evident in the model where the temperature increases from approximately -11 to -7°C (Fig. 5.25a).

The model represents fairly uniform temperatures over the ocean (approximately -4°C), with sharper gradients over the MIZ.
Furthermore, the surface specific humidity values range from about 1.4 to 1.9 g kg^{-1} along the sawtooth leg. A noticeable field of high humidity is also apparent at 10°W stretching from 69 to 74°N ($>$2.2 g kg^{-1}, Fig. 5.25b), possibly induced by strong surface heat fluxes generating high evaporation from the ocean. The modelled sensible and latent heat fluxes show distinct gradients near the area of high surface specific humidity (Fig. 5.26).
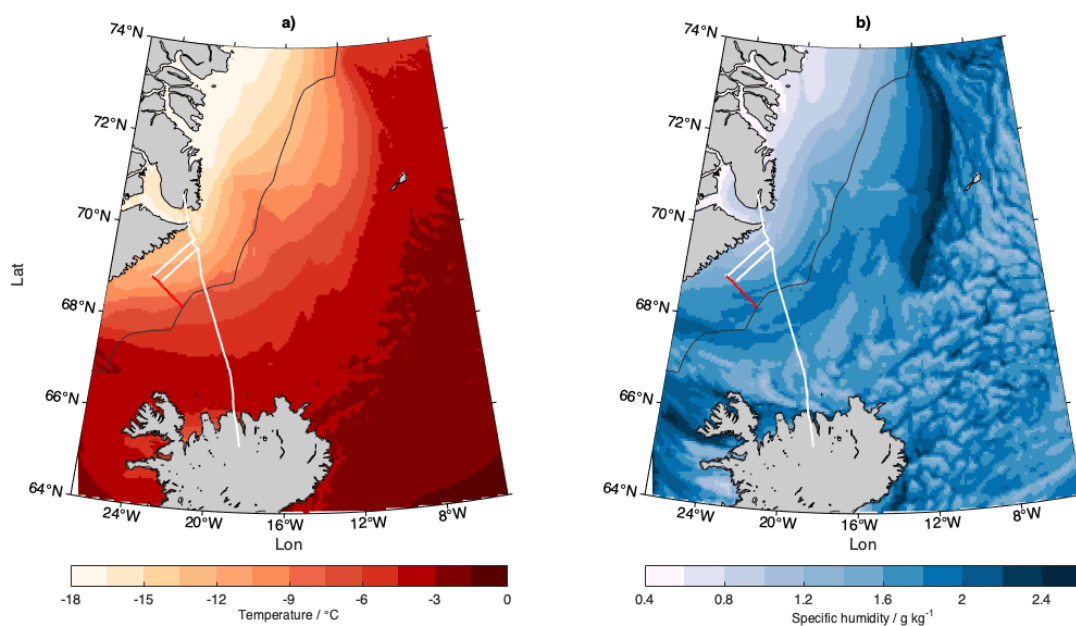
Figure 5.25: Aircraft flight track from flight 299 (white line) over the horizontal distributions of a) 980 hPa temperature (°C) and b) 980 hPa specific humidity (g kg^{-1}) by model run 0800 (+15h) on 8 March 15 UTC (filled contours). The selected sawtooth leg is highlighted in red.
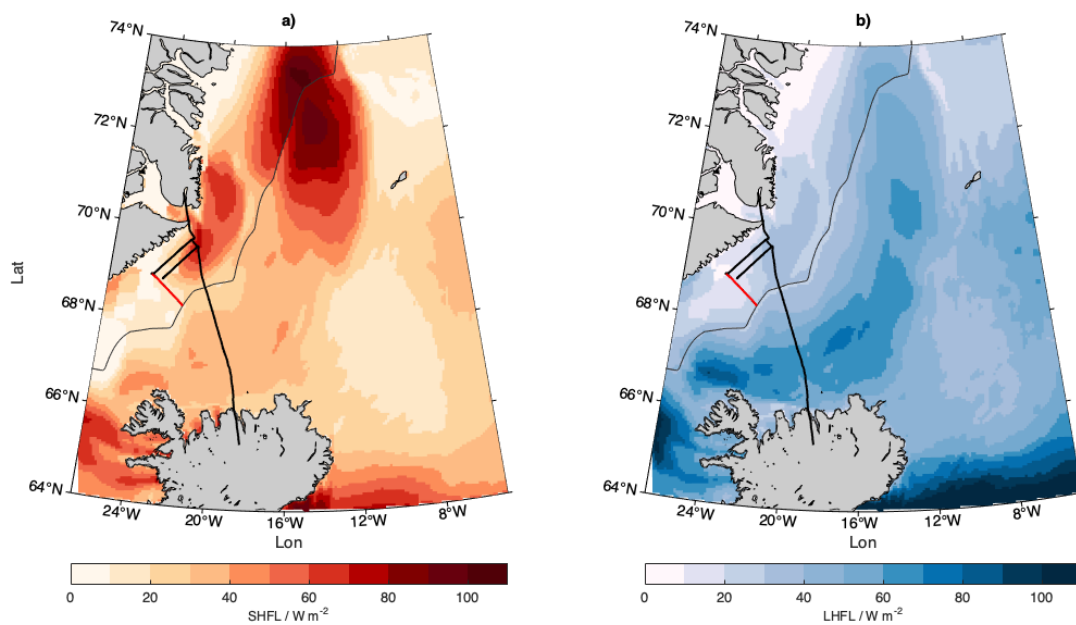

Figure 5.26: Aircraft flight track from flight 299 (thick black line) over the horizontal distributions of a) surface sensible heat flux, SHFL (Wm^{-2}) and b) surface latent heat flux, LHFL (Wm^{-2}) by model run 0800 (+15h) on 8 March 15 UTC (filled contours). The sawtooth leg is highlighted in red.

The sensible heat fluxes are strongest where the ocean releases most heat to the colder atmosphere during a CAO (>80 Wm^{-2}) at 72–74°N (Fig. 5.26a). The latent heat flux remains fairly constant at approximately 20–60 Wm^{-2} over large parts of the ocean, with a maximum of 80 Wm^{-2} north-west of Iceland (Fig. 5.26b). Both heat fluxes appear relatively weak along the sawtooth leg (<20 Wm^{-2}), which implies that there are no large air-sea differences in temperature or humidity, or strong winds in the area.

A consistent increase in temperature and humidity south-eastward from the ice edge is evident for both aircraft- and model data. However, the model exhibits a significantly warmer and moister boundary layer than the aircraft observations, with a temperature bias of approximately 4 K along the whole flight leg (Fig. 5.27a). The specific humidity represented by the model is far too humid near the coast, but becomes comparable to the observed quantity along the last sawtooth (Fig. 5.27b).
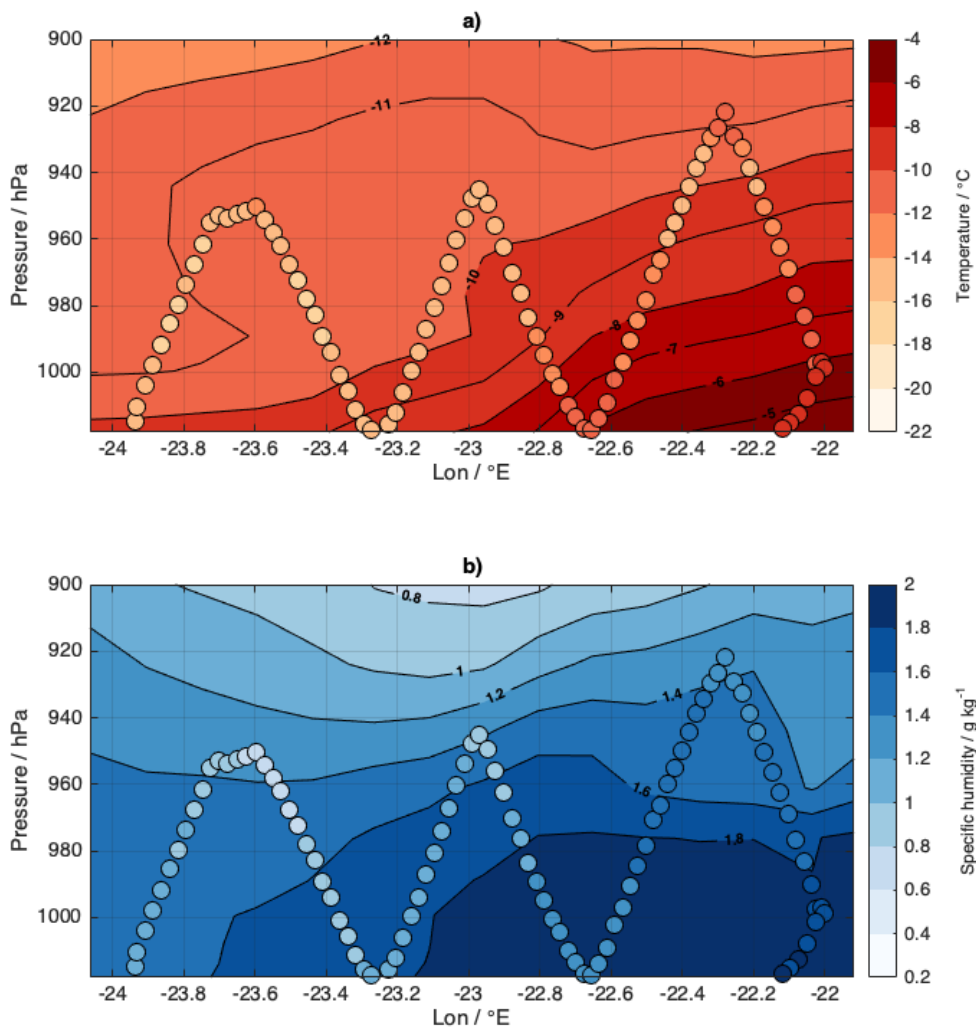

Figure 5.27: Cross-sections of a) temperature (°C) and b) specific humidity (g kg^{-1}) from model run 0800 (+15h) along the sawtooth leg indicated on the maps in Figs. 5.25 and 5.26, on 8 March 2018 15 UTC. Observed values every 20 seconds from the sawtooth leg during flight 299 are indicated as filled circles over the modelled simulation.

A possible source of error in this case is the impact of rapid changes in the atmospheric properties on the aircraft instruments when flying at low altitudes outwards from the Greenland coast over the MIZ (see Sec. 4.1.1). Even though some similarities can be identified in the contour structures, it is primarily evident that the model, in this case, does not manage to reproduce the detailed structure of the thermodynamic properties within the lower boundary layer. It is worth noting that the distance is short (approximately 90 km), the aircraft was flying over ice, and there might be some errors from the aircraft instruments during the rapid modifications of the near-surface atmosphere.

6 Summary and conclusions

Airborne field observations from a cold air outbreak event over the Iceland Sea have been investigated in order to obtain greater knowledge about CAOs and their effects, and to enhance the predictability in the area. A Twin Otter research aircraft and several radiosondes frequently obtained in situ measurements of the atmospheric boundary layer during a CAO event over the Iceland-Greenland Seas in the course of the IGP campaign in March 2018. Additionally, as part of a larger project on the atmospheric water cycle, the observations from the campaign were compared with the regional $COSMO_{iso}$ model in order to find the optimal model setup for simulating high-resolution stable isotopes with high precision. In total, five simulations were run with different lead times and resolutions, representing the weather situation on 4 March 2018. The model precision is evidently increasing with decreasing lead time and finer resolution. The best simulation for the 4 March forecast is the fine-resolution run 0400, initialised on 4 March 00 UTC. Hence, the optimal lead time is determined to be less than +24 hours. Simulations with fine resolution also generally provided the highest precisions despite the spin-up problems occurring in combination with long lead time.

A boundary layer deepening was mainly evident in the downwind direction from the Greenland coast due to large amounts of heat being transferred form the ocean, inducing convection and mixing. When comparing the observations with the model, all simulations generally overestimated the temperatures and humidities within the boundary layer. During run 0200, a distinct cyclone structure developed in the radiosonde area, causing too high easterly winds and excessive temperature- and humidity values near the surface. By running the same simulation with a coarser resolution, the cyclone was still evident, but to a slightly lesser extent. The dynamics behind the instability were thoroughly investigated, and in addition to a long spin-up time, high equivalent potential temperatures (θ_e) near the area of origin seem to have enhanced the cyclogenesis. Further, run 0300 exhibited slightly lower temperature- and humidity values in the radiosonde area than run 0200, but an intense low pressure system occurred east of Iceland a few hours later. However, this system disappeared entirely when the same simulation was run with a coarser resolution, confirming that spin-up problems may occur during the transition from the coarse-resolution initial boundary data to the much finer resolution of COSMO. At last, the fine-resolution run 0400 included lower temperature- and humidity values and weaker gradients than the other runs, providing the highest precision of the five simulations.

High model precision is crucial in climate- and weather forecasting. By increasing the number of observations over the Iceland-Greenland Seas, this research contributes to enhance the precision over this relatively unexplored area for future weather prediction models.

Appendices

A   Model set up

A.1   COSMO job

The code for the COSMO model setup is given in Listing 1. This specific code is for the high-resolution run 0400 which was concluded as the optimal run for further comparisons with observations. The initial time (`ydate_ini`) is changed for model runs 0200, 0300 and 0800. Furthermore, the horizontal grid spacings (`dlon` and `dlat`), total number of grids (`ie_tot` and `je_tot`) and domain limits (`startlon_tot` and `startlat_tot`) are changed for the coarse-resolution simulations.

A.2   Integration to LM

The code for the integration to Lokal Model in run 0200 is given in Listing 2.

Listing 1: COSMO model setup for run 0400 (fine resolution)

```
# The COSMO Job


###################################################
# prepare job skript
###################################################

cat > make_cosmo_job << EOF
#!/bin/bash
#--- Job settings:
#-----------------

#### job name:
#SBATCH --account=nn9555k
#SBATCH --partition=${QUEUE}
#PBS -N ${WDIR}_cosmo_job

#### wall time limit
#SBATCH --time=$WALLTIME

#SBATCH --nodes=${NODES} --ntasks-per-node=${NMULT}

#### join stdout and stderr

#### email address
##PBS -M $EMAIL

#cd \$PBS_O_WORKDIR
#echo \$PBS_O_WORKDIR

echo "mother superior: \$(uname -n)"
#NSLOTS=\$(cat \$PBS_NODEFILE | wc -l)
#echo "running on \$NSLOTS cpus ..."
ulimit -s unlimited
ulimit -a

# load modules
module restore system
module load ifort/2018.1.163-GCC-6.4.0-2.28
module load netCDF-Fortran/4.4.4-intel-2017a-HDF5-1.8.18
module load icc/2018.1.163-GCC-6.4.0-2.28
module load ifort/2018.1.163-GCC-6.4.0-2.28
module load iccifort/2018.1.163-GCC-6.4.0-2.28
module load impi/2018.1.163-iccifort-2018.1.163-GCC-6.4.0-2.28
module load iimpi/2018a
module load imkl/2018.1.163-iimpi-2018a
module load intel/2018a
module load zlib/1.2.11-GCCcore-6.4.0
module load Szip/2.1.1-GCCcore-6.4.0
module load HDF5/1.8.19-intel-2018a
module load netCDF/4.4.1.1-intel-2018a-HDF5-1.8.19
module load netCDF-Fortran/4.4.4-intel-2018a-HDF5-1.8.19
```

```
module load bzip2/1.0.6-GCCcore-6.4.0
module load libpng/1.6.34-GCCcore-6.4.0

set -e

#--- Environment settings:
#-------------------------

MPIPROGINF='DETAIL'                 # program information
export MPIPROGINF                   # {NO|YES|DETAIL}
#
MPISUSPEND='ON'                     # select waiting method
export MPISUSPEND                   # {ON|OFF}={SUSPEND/RESUME|SPIN WAIT}
#
F_FTRACE='NO'                       # analysis list from compile opt. -ftrace
export F_FTRACE                     # {NO|YES|FMT0|FMT1|FMT2}
#
F_ERRCNT=0                          # stop execution after the first run time
                                    # error
export F_ERRCNT

#LD_LIBRARY_PATH="${LD_LIBRARY_PATH}"
#export LD_LIBRARY_PATH
LIBDWD_FORCE_CONTROLWORDS=1
export LIBDWD_FORCE_CONTROLWORDS

#--- Prepare namelist files:
#---------------------------

cat > INPUT_ORG << end_input_org
 &LMGRID
  startlon_tot=-5.4, startlat_tot=-2.4,
  pollat=25.0,       pollon=165.0,
  dlon=0.05,         dlat=0.05,
  ie_tot=250,        je_tot=250,        ke_tot=40,
 /
 &RUNCTL
  ydate_ini='2018030400',
  ydate_bd='2018030400',
  dt=15.0,
  hstart=0.0,  hstop=48.0,
  idbg_level=100,
  lreproduce=.FALSE., luseobs=.FALSE.,
  lphys=.TRUE., ldiagnos=.TRUE., ldfi=.FALSE.,
  luse_rttov=.FALSE.,
  nprocx= $NPX, nprocy= $NPY, nprocio=$NPIO,
  nboundlines=4, lreorder=.FALSE.,
  ldatatypes=.FALSE.,
  ncomm_type=1, liso=.TRUE.,
  hincmxt=6.0,
  hincmxu=6.0,
 /
 &TUNING
  clc_diag=0.5, rat_lam=1.0, rat_can=1.0,
  c_soil=1.0, v0snow=25.0,
  wichfakt=0.0, crsmin=150., qc0=0.0, qi0=0.0,
```

```
 /
end_input_org

cat > INPUT_IO << end_input_io
 &IOCTL
  ngribout=1, lasync_io=.FALSE.,
  lbdclim=.TRUE.,
 /
 &DATABASE
 /
 &GRIBIN
  ydirini='/cluster/work/users/$USER/cosmo/input/iceland2018_17o_fine/',
  lchkini=.TRUE.,
  lana_qi=.TRUE., lana_qr_qs=.FALSE., lana_rho_snow=.FALSE.,
  ydirbd='/cluster/work/users/$USER/cosmo/input/iceland2018_17o_fine/',
  hincbound=6.0,
  lchkbd=.TRUE.,
  llb_qi=.TRUE., llb_qr_qs=.FALSE.,
  lbdana=.TRUE.,
  lan_t_so0=.TRUE., lan_t_cl=.TRUE., lan_w_cl=.TRUE.,
  lan_vio3=.TRUE., lan_hmo3=.TRUE., lan_plcov=.TRUE., lan_lai=.TRUE.,
  lan_rootdp=.TRUE., lan_t_snow=.TRUE., lan_w_i=.TRUE., lan_w_snow=.TRUE.,
  lan_rho_snow=.TRUE.,
 /
 &GRIBOUT
  ysystem='file',
  yform_write='ncdf',
  hcomb= 0.,48.0,3.0,
  l_p_filter=.TRUE.,
  l_z_filter=.TRUE.,
  ytunit='d',
  yvarml='U', 'V', 'W', 'P', 'T', 'QV', 'QC', 'QI', 'QR', 'QS', 'PS', 'PMSL', 'RAIN_GSP',
'SNOW_GSP', 'RAIN_CON', 'SNOW_CON', 'TOT_PREC', 'QV18O', 'QV2H', 'QV17O', 'QC18O', 'QC2H',
'QC17O', 'QI18O', 'QI2H', 'QI17O', 'QR18O', 'QR2H', 'QR17O', 'QS18O', 'QS2H', 'QS17O',
'RAIN_18O_G', 'SNOW_18O_G', 'RAIN_18O_C', 'SNOW_18O_C', 'RAIN_2H_G', 'SNOW_2H_G',
'RAIN_2H_C', 'SNOW_2H_C', 'RAIN_17O_G', 'SNOW_17O_G', 'RAIN_17O_C', 'SNOW_17O_C',
'AEVAP_S', 'HPBL', 'R18OSOIL_P', 'R2HSOIL_P', 'R17OSOIL_P', 'R18OSOIL', 'R2HSOIL',
'R17OSOIL', 'EVAPTOT', 'EVAP18O', 'EVAP2H','EVAP17O', 'BSEVAP', 'BSEVAP18O', 'BSEVAP2H',
'BSEVAP17O', 'IEVAP', 'IEVAP18O', 'IEVAP2H', 'IEVAP17O', 'PTEVAP', 'PTEVAP18O', 'PTEVAP2H',
'PTEVAP17O', 'SNOEVAP', 'SNOEVAP18O', 'SNOEVAP2H', 'SNOEVAP17O', 'W_SO',
'W_SNOW','T_G','QV_S','QV_2M','RELHUM','RELHUM_2M','TQV','ALHFL_S','ASHFL_S','T_2M','U_10M'
,'V_10M',
  yvarpl=,
  yvarzl=,
  yvarsl='default',
  lcheck=.TRUE.,
  lwrite_const=.TRUE.,
  ydir='$OUTDIR',
 /
end_input_io

cat > INPUT_DYN << end_input_dyn
 &DYNCTL
  l2tls=.TRUE., irunge_kutta=2, irk_order=3, iadv_order=5,
              y_scalar_advect='Bott4',
              y_vert_adv_dyn='impl2', ieva_order=3,
```

```
   ldiabf_lh=.TRUE.,
   lsemi_imp=.FALSE., lcond=.TRUE.,
   lspubc=.TRUE., lexpl_lbc=.TRUE., ldyn_bbc=.TRUE.,
   betasw=0.4, xkd=0.1, epsass=0.15,
   lhordiff=.TRUE., itype_hdiff=2,
   hd_corr_u_bd=0.25, hd_corr_u_in=0.25,
   hd_corr_t_bd=0.0, hd_corr_t_in=0.0,
   hd_corr_q_bd=0.0, hd_corr_q_in=0.0,
   hd_corr_p_bd=0.0, hd_corr_p_in=0.0,
   hd_dhmax=250.0, itype_bbc_w=2,
 /
end_input_dyn

cat > INPUT_PHY << end_input_phy
 &PHYCTL
    lgsp=.TRUE., itype_gscp=3, lprogprec=.TRUE., ldiniprec=.FALSE.,
                ltrans_prec=.TRUE.,
    lrad=.TRUE., hincrad=1.0, nradcoarse=1, lradf_avg=.FALSE.,
    ltur=.TRUE., itype_turb=3, ninctura=1, imode_turb=1,
                itype_tran=2, imode_tran=1,
                lexpcor=.FALSE., ltmpcor=.FALSE., lprfcor=.FALSE.,
                lnonloc=.FALSE., lcpfluc=.FALSE., limpltkediff=.TRUE.,
       itype_wcld=2, icldm_rad=4, icldm_turb=1, icldm_tran=0,
       itype_synd=2,
    lsoil=.TRUE., itype_evsl=2, itype_trvg=2,
                lmulti_layer=.TRUE., lmelt=.TRUE., lmelt_var=.TRUE.,
        ke_soil=7,
        czml_soil = 0.005, 0.02, 0.06, 0.18, 0.54, 1.62, 4.86, 14.58,
    lconv=.TRUE., lcape=.FALSE., nincconv=4,
    lforest=.TRUE., llake=.FALSE., lseaice=.FALSE., lsso=.TRUE.
 /
end_input_phy

cat > INPUT_DIA << end_input_dia
 &DIACTL
  n0gp=0,      hincgp=1.0,
  n0meanval=0, nincmeanval=1,
  lgplong=.FALSE., lgpshort=.TRUE., lgpspec=.FALSE.,
 /
end_input_dia

cat > INPUT_INI << end_input_ini
 &INICTL
  ndfi=1, nfilt=1,
  tspan=3600.0, taus=3600.0,
  dtbak=40.0, dtfwd=40.0,
 /
end_input_ini

cat > INPUT_ASS << end_input_ass
 &NUDGING
  lnudge=.FALSE.,
 /
end_input_ass

cat > INPUT_ISO << end_input_iso
```

```
 &ISOCTL
  imodsoil_iso=0, imodroce_iso=1, roce_iso=1.0,1.0,1.0, imodevap_iso=2, imodrainev_iso=2,
fequ_conv_iso=0.5, imodplant_iso=0
 /
end_input_iso


#--- Start the run:
#-----------------

mpiexec -np $NP /cluster/home/hso039/bin/cosmo_iso_terra
rm -f INPUT_*

#--- Notification that job is finished:
#-------------------------------------

mailx -s "Job $WDIR finished!" $EMAIL <<EOF_mail
Model run $WDIR finished at \`date\` on \`uname -n\`
Last output file produced: \`ls -lrt $OUTDIR | tail -1\`
EOF_mail

# copy results to nird for storage
rsync -rv $WORK/cosmo/output/${WDIR}/* /nird/projects/nird/NS9054K/cosmo_iso/output/$WDIR/
run_0400
```

Listing 2: The integration to Lokal Model (LM) for run 0200 (fine resolution)

```
# The INT2LM Job


####################################################
# prepare job skript
####################################################

cat > int2lm_job << EOF
#!/bin/bash
#--- Job settings:
#-----------------

#### job name:
#SBATCH --account=nn9555k
#SBATCH --partition=${QUEUE}
#PBS -N ${WDIR}_int2lm_job

#### wall time limit
#SBATCH --time=$WALLTIME

#SBATCH --nodes=${NODES} --ntasks-per-node=${NMULT}

#### join stdout and stderr
#PBS -j oe

#### email address
##PBS -M $EMAIL

#cd \$PBS_O_WORKDIR
#echo \$PBS_O_WORKDIR

echo "mother superior: \$(uname -n)"
#NSLOTS=\$(cat \$PBS_NODEFILE | wc -l)
#echo "running on \$NSLOTS cpus ..."
ulimit -s unlimited
ulimit -a

# load modules
#module load ifort/2017.4.196-GCC-6.4.0-2.28
module load ifort/2018.1.163-GCC-6.4.0-2.28
module load netCDF-Fortran/4.4.4-intel-2017a-HDF5-1.8.18

set -e

#--- Environment settings:
#------------------------

MPIPROGINF='DETAIL'              # program information
export MPIPROGINF               # {NO|YES|DETAIL}
#
MPISUSPEND='ON'                 # select waiting method
export MPISUSPEND               # {ON|OFF}={SUSPEND/RESUME|SPIN WAIT}
```

```
#
F_FTRACE='NO'                          # analysis list from compile opt. -ftrace
export F_FTRACE                        # {NO|YES|FMT0|FMT1|FMT2}
#
F_ERRCNT=0                             # stop execution after the first run time
                                       # error
export F_ERRCNT

#LD_LIBRARY_PATH="/opt/parastation/mpi2-intel/lib:${LD_LIBRARY_PATH}"
#export LD_LIBRARY_PATH
LIBDWD_FORCE_CONTROLWORDS=1
export LIBDWD_FORCE_CONTROLWORDS

#--- Loop over all files:
#-----------------------

HINC=06
HSTOP=192
HADD=0
YDATE_START='2018030200'

rm -f YU* OUTPUT

while [ \${HADD} -le \${HSTOP} ]
do
YDATE_INI=\`'/cluster/home/hso039/bin/get_utc_date \${YDATE_START} \${HADD} 365\`

echo "running for " \${YDATE_INI}

#--- Prepare namelist file:
#-------------------------

cat > INPUT << end_input
 &CONTRL
  ydate_ini='\${YDATE_INI}',
  hstart=0.0, hstop=0.0, hincbound=0.0,
  nprocx=$NPX, nprocy=$NPY, lreorder=.FALSE.,
  yinput_model='CM', idbg_level=5,
  linitial=.TRUE., lboundaries=.FALSE.,
  ltime_mean=.TRUE., luvcor=.TRUE.,
  lfilter_pp=.FALSE., lbalance_pp=.FALSE., norder_filter=5,
  lfilter_oro=.TRUE., eps_filter=0.1,
  ilow_pass_oro=1, ilow_pass_xso=0, rxso_mask=0.0,
  lprog_qi=.TRUE., lpost_0006=.TRUE.,
  lmulti_layer_in=.TRUE., lmulti_layer_lm=.TRUE., l_smi=.FALSE.,
  lsso=.TRUE., lforest=.TRUE., lt_cl_corr=.TRUE., luse_t_skin=.FALSE.,
  itype_w_so_rel=3,
  itype_t_cl=1,
  itype_rootdp=0,
  itype_ndvi=0,
  lprog_qr_qs=.FALSE., lprog_rho_snow=.FALSE.,
  luvcor=.TRUE., lvertwind_ini=.TRUE., lvertwind_bd=.FALSE.,
  liso=.TRUE.,
 /
&GRID_IN
  ie_in_tot=98, je_in_tot=80, ke_in_tot=31,
```

```
   pollon_in=180.0, pollat_in=90.0,
   dlon_in=1.125, dlat_in=1.1215,
   startlon_in_tot=-59.625, startlat_in_tot=0.56074,
   endlon_in_tot=49.5, endlat_in_tot=89.142,
   pcontrol_fi=30000.0,
   ke_soil_in=4,
   czml_soil_in=0.03,0.19,0.78,2.68,6.98,
 /
 &LMGRID
   ielm_tot=250, jelm_tot=250, kelm_tot=40,
   pollon=165.0, pollat=25.0,
   dlon=0.05, dlat=0.05,
   startlon_tot=-5.4, startlat_tot=-2.4,
   ke_soil_lm=7,
   czml_soil_lm=0.005, 0.02, 0.06, 0.18, 0.54, 1.62, 4.86, 14.58,
/
 &DATABASE
 /
 &DATA
   ylmext_cat='$WORK/int2lm/expar/',
   ylmext_lfn='COSMO_IGP2018_700x560.nc',
   ie_ext=700, je_ext=560,
   yinext_cat='$WORK/int2lm/input/echamwiso_17o/',
   yinext_lfn='cas\${YDATE_INI}.nc',
   yin_cat='$WORK/int2lm/input/echamwiso_17o/',
   ylm_cat='$OUTDIR',
   yinput_type='analysis'
   nprocess_ini=131, nprocess_bd=132,
   yinext_form_read='ncdf', yin_form_read='ncdf',
   ylmext_form_read='ncdf'
 /
 &PRICTR
   igp_tot = 36, 40, 48, 44, 48, 85, 77
   jgp_tot = 30, 94, 38, 26, 26, 96, 12
   lchkin=.TRUE., lchkout=.TRUE.,
 /
end_input

#--- Start the run:
#-----------------

rm -f YUCHKDAT YUTIMING YUDEBUG OUTPUT
mpiexec -np $NP /cluster/home/hso039/bin/int2lm
rm INPUT

HADD=\`expr \${HADD} + \${HINC}\`

done

#--- Notification that job is finished:
#-------------------------------------

mailx -s "Job $WDIR finished!" $EMAIL <<EOF_mail
Model run $WDIR finished at \`date\` on \`uname -n\`
Last output file produced: \`ls -lrt $OUTDIR | tail -1\`
EOF_mail
```

B Aircraft data

The evolution of air pressure, air temperature, specific humidity and relative humidity along each flight path during the period 4–9 March 2018 are illustrated in Figs. B.1–B.5. Note that the relative humidity (d) frequently presents erroneous values by exceeding 100%.
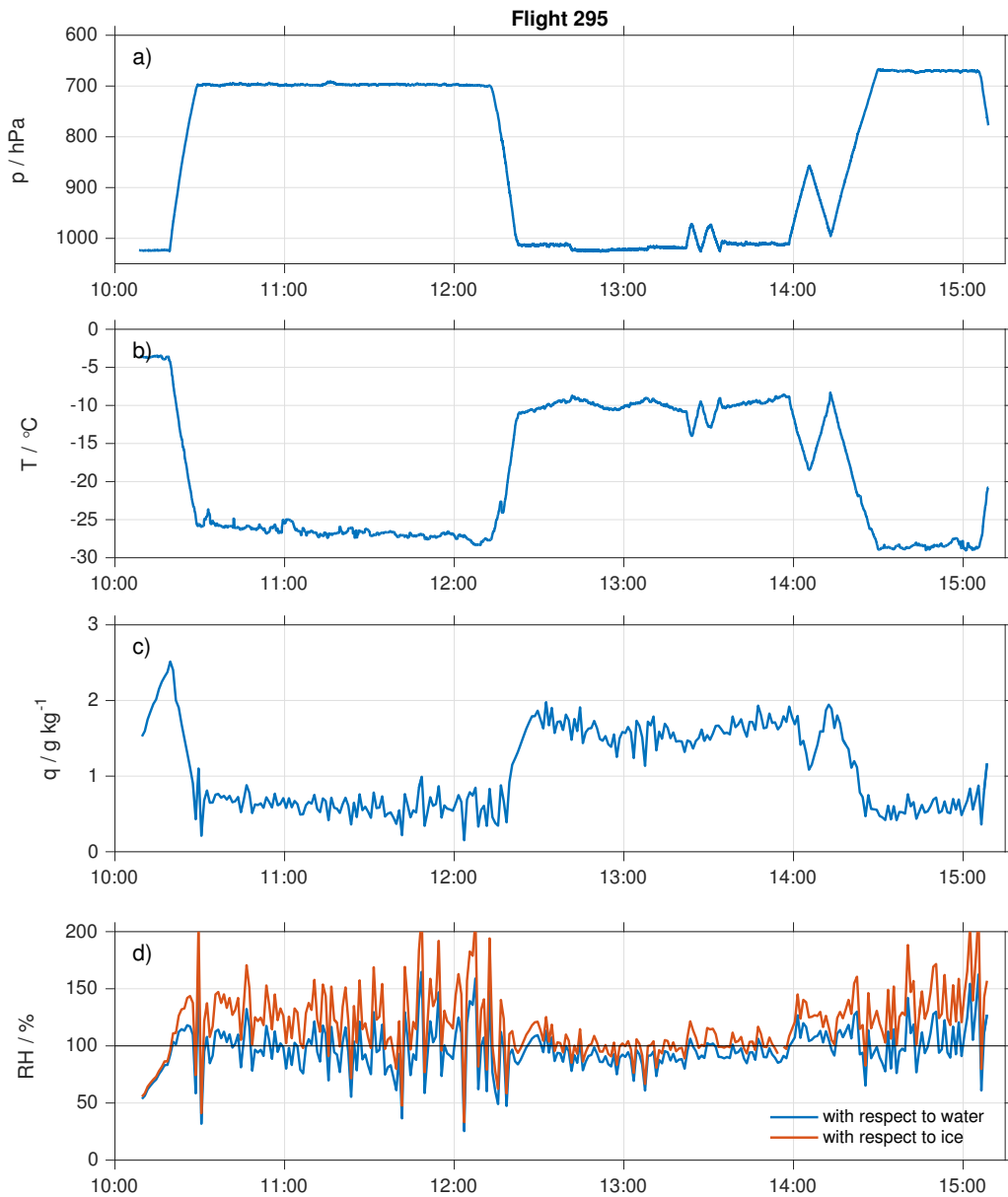

Figure B.1: a) Pressure (hPa), b) Temperature (°C), c) specific humidity(g kg^{-1}) and d) relative humidity (%) with respect to water (blue) and ice (orange) during flight 295 on 4 March 2018.
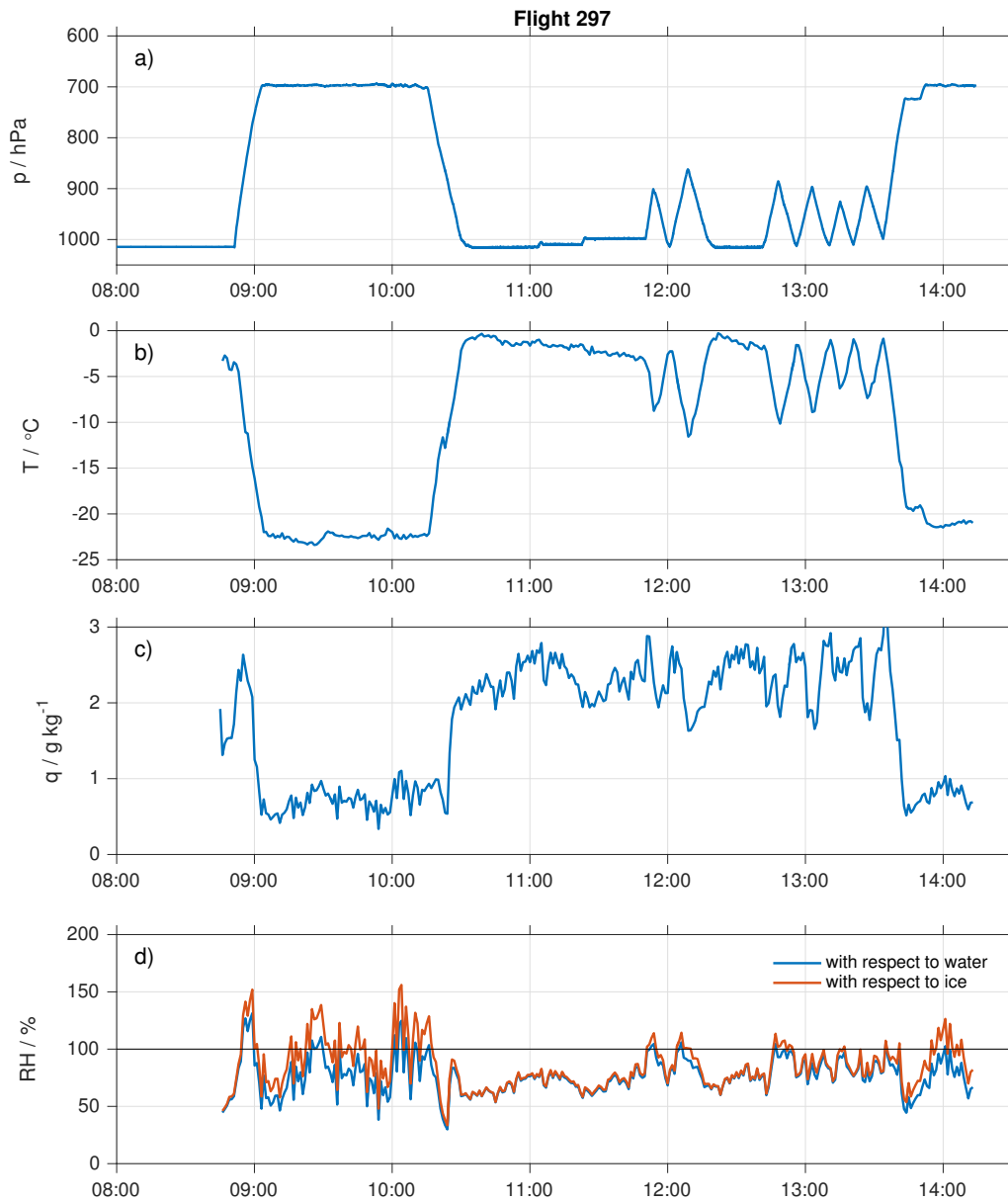
Figure B.2: As Figure B.1, but for flight 297 on 6 March. The air temperature (b) is obtained from a DMT cloud and aerosol spectrometer (CAPS) probe, since the Rosemount sensor did not work during this flight.
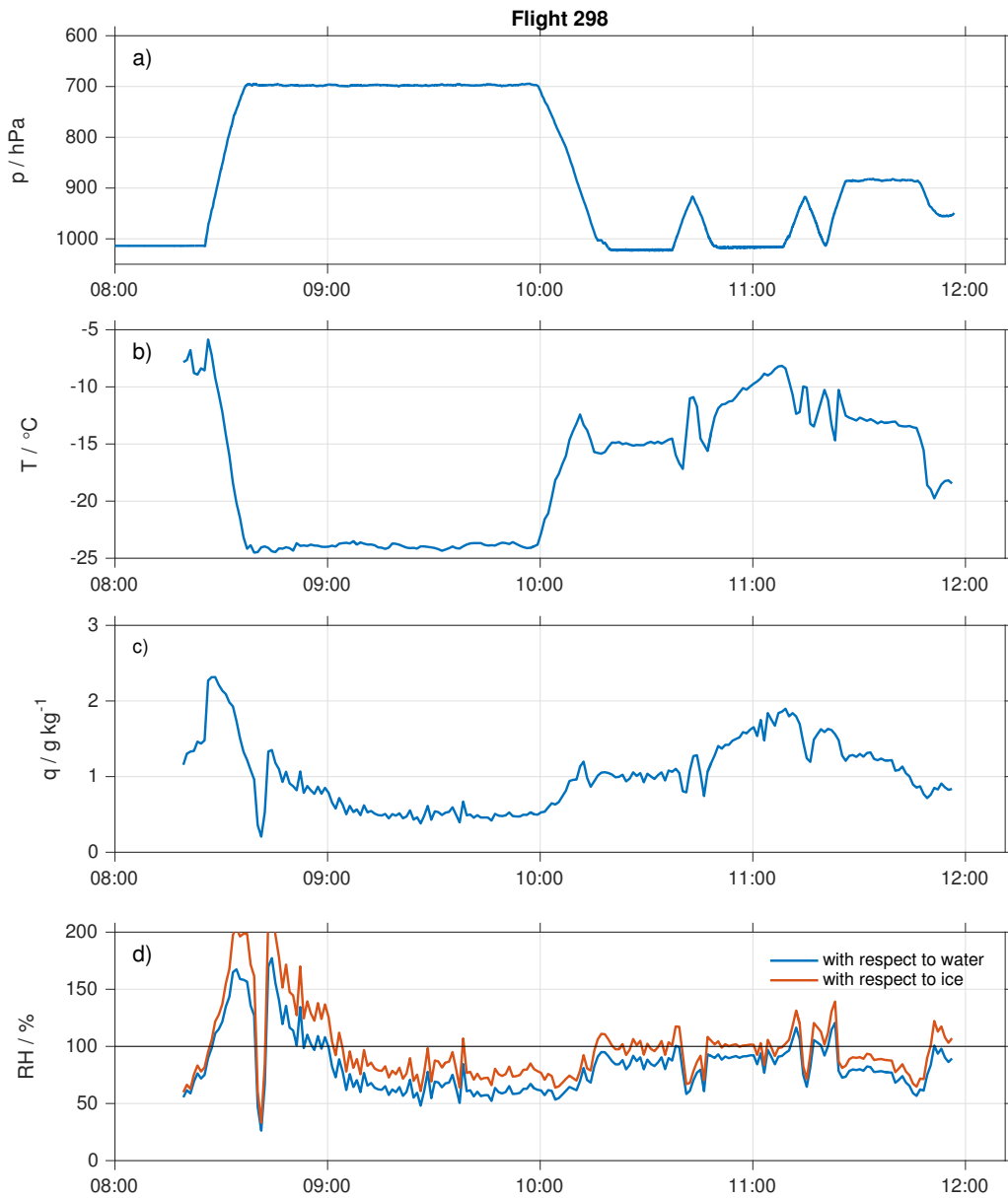
Figure B.3: As Figure B.1, but for flight 298 on 8 March.
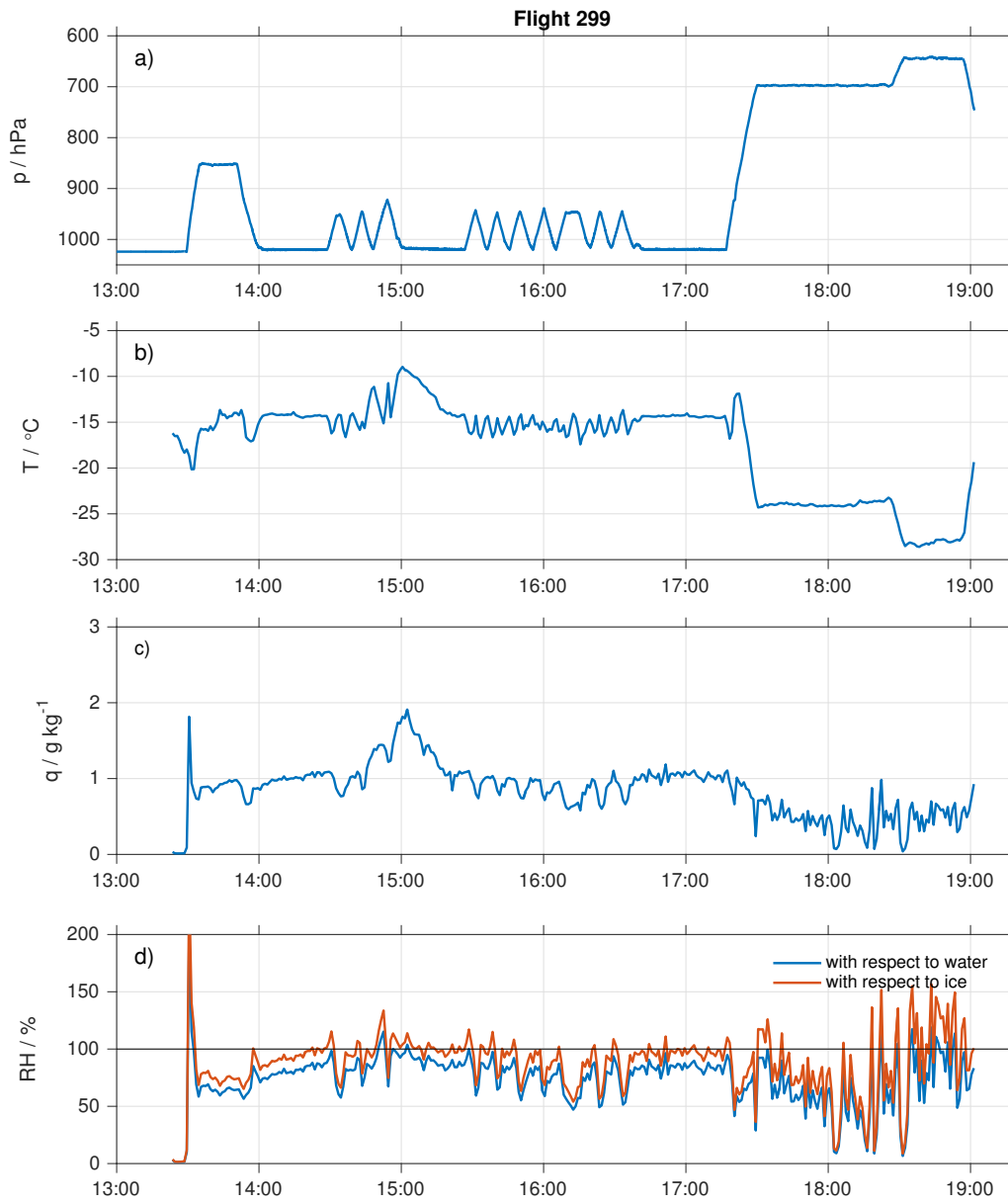
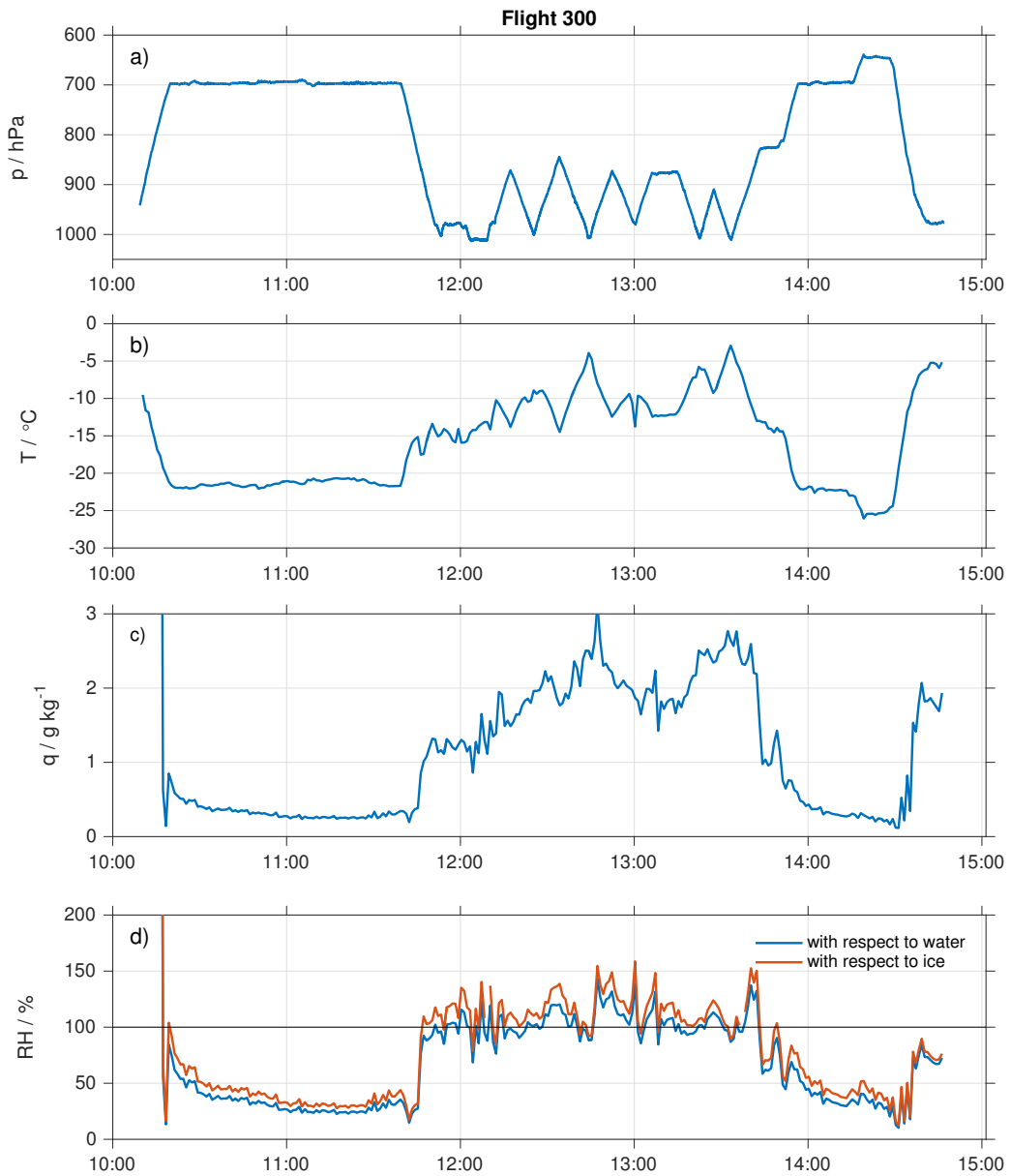Figure B.4: As Figure B.1, but for flight 299 on 8 March.

Figure B.5: As Figure B.1, but for flight 300 on 9 March.

C   Additional analysis of the cyclogenesis in run 0200

In Section 5.3.1, the cyclogenesis on 3 March 03 UTC in run 0200 was investigated by comparing equivalent potential temperature (θ_e) and stability ($\theta_{800hPa} - \theta_{900hPa}$) with run 0300. The horizontal distribution of relative vorticity ζ (Fig. C.1), surface heat fluxes (Figs. C.2 and C.3) and convective rainfall (Fig. C.4) were also considered as influences on the developing cyclone. The following figures compare these properties from run 0200 and run 0300, where no distinct differences are found in the area where the cyclone developed.
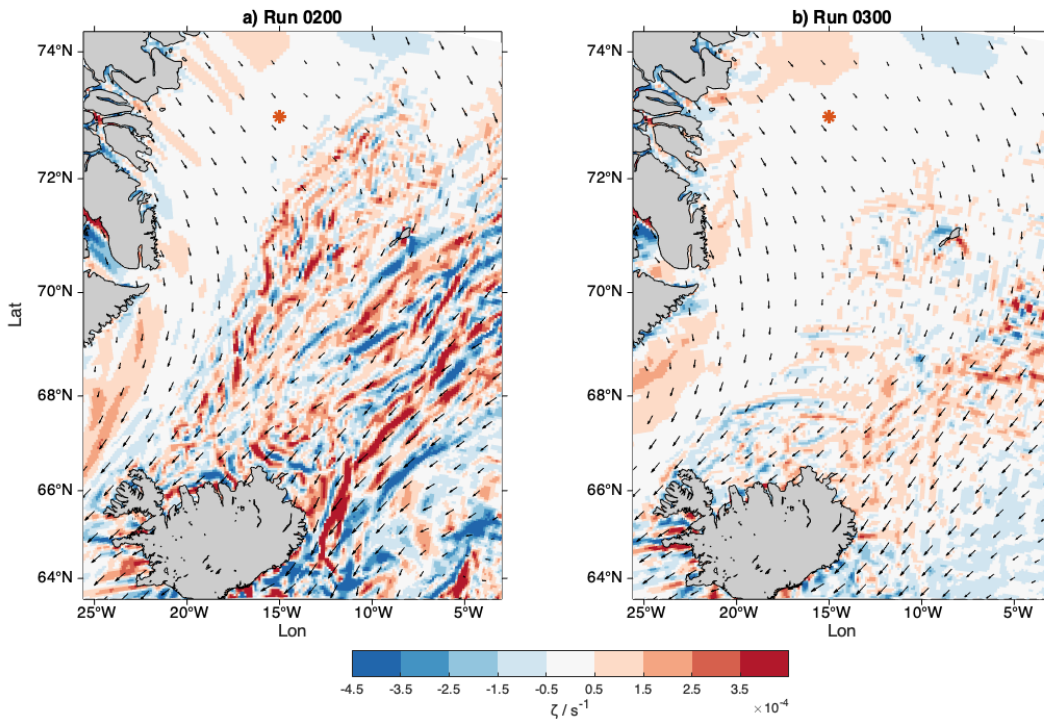
Figure C.1: Relative vorticity ζ (s^{-1}) and wind vectors at 800 hPa for a) model run 0200 (+27h) and b) model run 0300 (+3h) on 3 March 03 UTC. The red star at 73°N, 14°W indicates the approximate location of where the cyclone first appears at sea level pressure in run 0200.
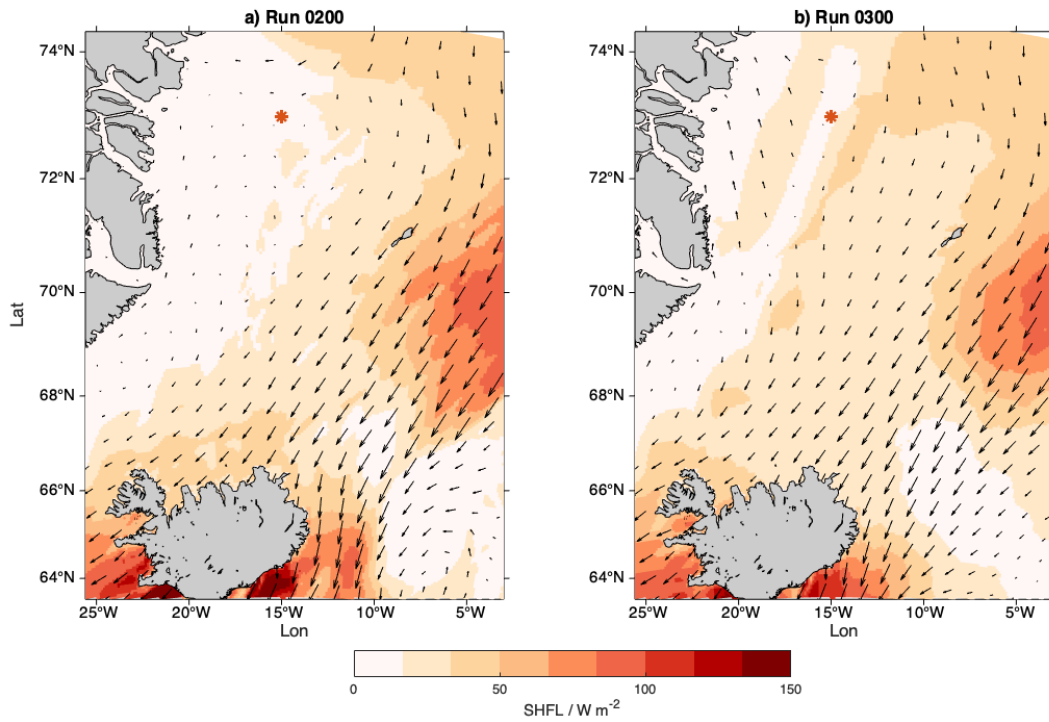
Figure C.2: Surface sensible heat flux, SHFL (Wm^{-2}) and 10 m wind (vectors) for a) model run 0200 (+27h) and b) model run 0300 (+3h) on 3 March 03 UTC.
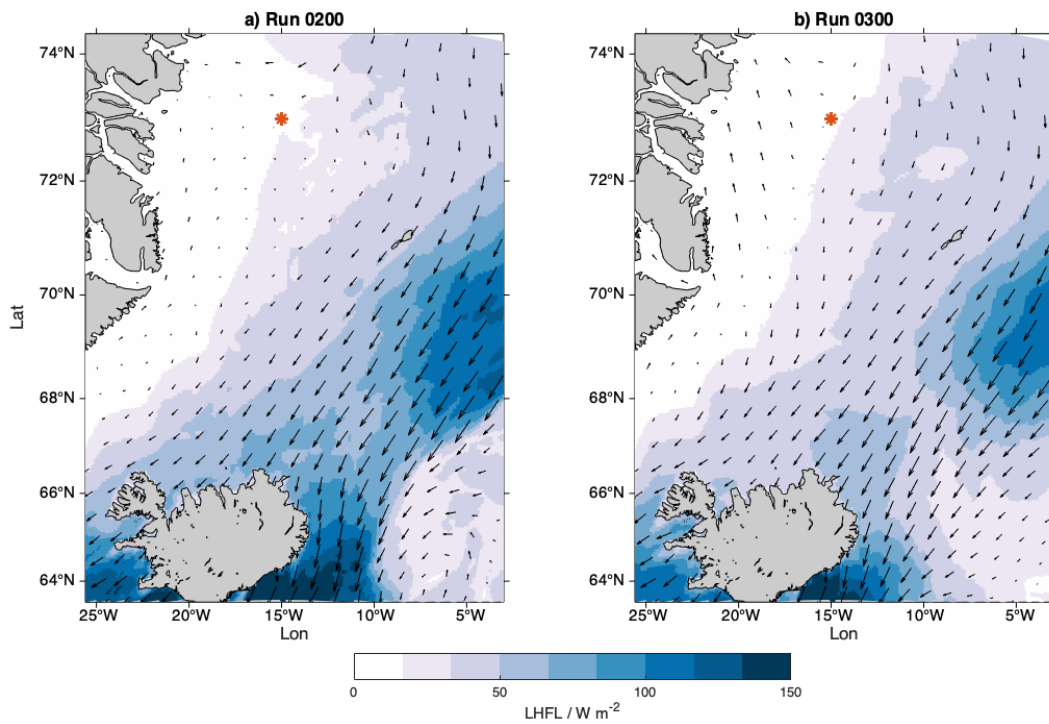

Figure C.3: Surface latent heat flux, LHFL (Wm^{-2}) and 10 m wind (vectors) for a) model run 0200 (+27h) and b) model run 0300 (+3h) on 3 March 03 UTC.
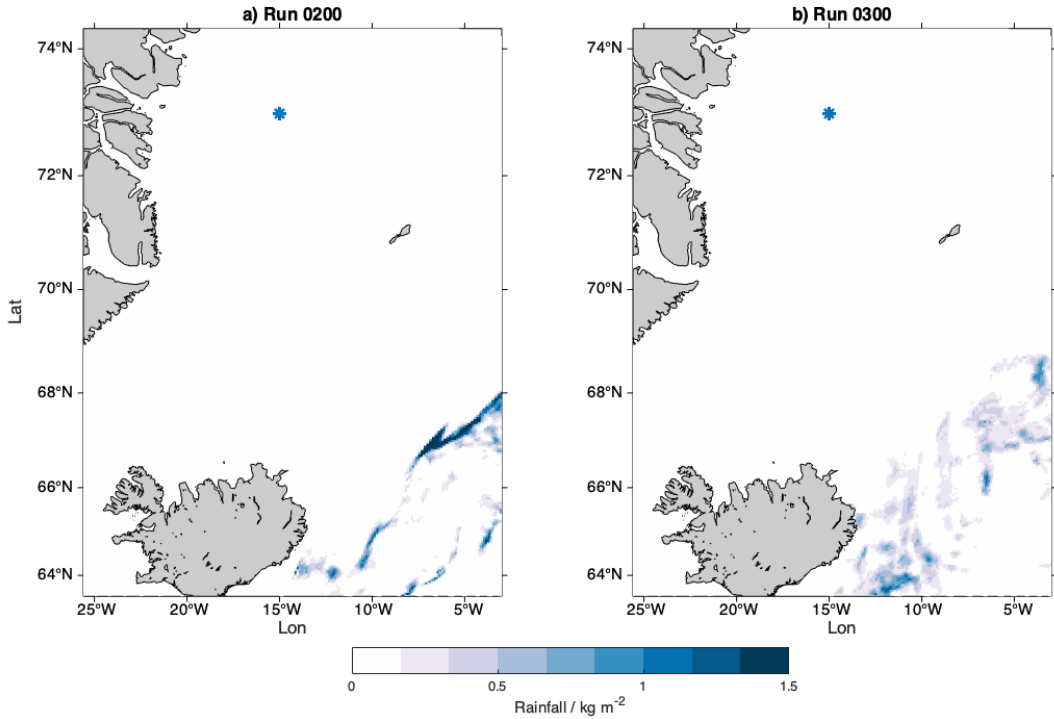
Figure C.4: Convective rainfall (kg m^{-2}) for a) model run 0200 (+27h) and b) model run 0300 (+3h) on 3 March 03 UTC.

D   Model bias for runs 0200 and 0300

In Section 5.4, temperature- and humidity cross-sections from the four radiosondes on 4 March 09, 12, 15 and 18 UTC were compared with the corresponding model results from run 0400.

Next, the radiosondes are compared with run 0200 and run 0300, with fine and coarse resolution, in order to compare their errors with those of run 0400 (Table 5.3). During run 0200, the cyclone of exceedingly high humidity values was most distinct at 09 UTC. It then advects south-westward from 69°N, 18°W to 67°N, 20°W during the nine hours (Fig. D.1), just like the field of higher humidity during run 0400 (Fig. 5.18). This behaviour is also apparent for run 0300, but to a considerably lesser extent than for run 0200 (Fig. D.2).
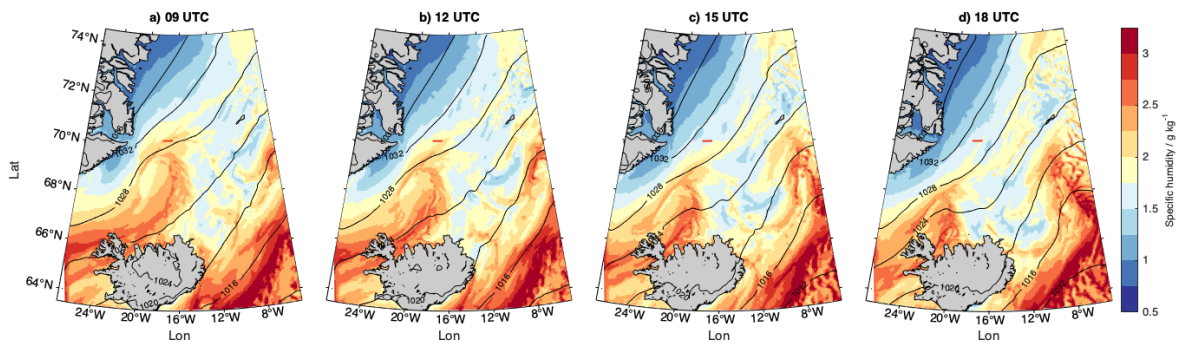

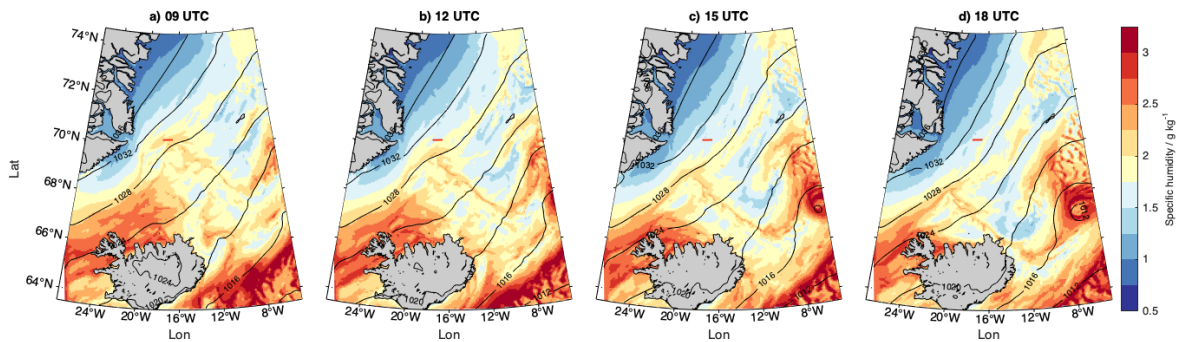Figure D.1: As Figure 5.18, but for run 0200 (fine resolution).

Figure D.2: As Figure 5.18, but for run 0300 (fine resolution).

Accordingly, the specific humidity in all model runs decreases with time near the radiosonde area. However, run 0200 exhibits excessively high humidity values in this area, and the gradients are stronger than for the other simulations. The temperature biases between run 0200 and the radiosonde observations are consistently about 0.2 K higher than for run 0300 (Table D.1) and up to 1 K higher than for run 0400. It is also evident that the simulated humidity is most accurate at 12 and 15 UTC for all three fine-resolution runs, with biases from 0.01 to 0.09 g kg^{-1}.

Table D.1: Mean temperature (T)- and humidity (q) bias between model runs 0200 and 0300 (fine resolution) and the four radiosondes on 4 March 09, 12, 15 and 18 UTC. The bias is calculated from the ground up to 600 hPa (by Eq. 4.8).

| | Bias T (K) | | Bias q (g kg^{-1}) | |
UTC	run 0200	run 0300	run 0200	run 0300
09	1.8	1.5	0.16	0.15
12	1.3	1.1	0.09	0.02
15	1.0	0.9	0.05	0.03
18	0.5	0.3	0.14	0.13
Avg.	1.2	1.0	0.11	0.08

Furthermore, the coarse-resolution runs 0200c and 0300c exhibit slightly larger temperature- and humidity errors than the corresponding fine-resolution runs at 09 and 12 UTC. However, at 15 and 18 UTC, the coarse-resolution runs exhibit smaller errors than the fine-resolution runs (Tables D.1 and D.2). On average, the temperature biases are similar for both fine and coarse resolution, while the humidity bias is 0.01 g kg^{-1} higher with coarse resolution. The high-resolution run 0400 still obtains the most accurate results with biases of 0.5 K and 0.05 g kg^{-1} (Table 5.4). An exception is evident at 18 UTC where the coarse-resolution runs display humidity biases of 0.10 and 0.09 g kg^{-1}, compared with 0.14, 0.13 and 0.11 g kg^{-1} for the fine-resolution runs 0200, 0300 and 0400 respectively (Tables D.1 and 5.3). The notably dry area observed above 800 hPa at 18 UTC appears to be better represented by simulations of coarse resolution.

Table D.2: As Table D.1, but for run 0200c and run 0300c (coarse resolution).

| | Bias T (K) | | Bias q (g kg^{-1}) | |
UTC	run 0200c	run 0300c	run 0200c	run 0300c
09	2.0	1.8	0.25	0.18
12	1.6	1.3	0.12	0.09
15	1.0	0.8	0.03	0.01
18	0.3	0.2	0.09	0.09
Avg.	1.2	1.0	0.12	0.09

Cross-sections of temperature- and humidity errors between these four model runs and radiosonde observations are illustrated in Figure D.3–D.6. The vertical structures of the biases are quite similar for all model runs (as Fig. 5.20), but the magnitudes are larger for longer lead times and coarser horizontal resolution.
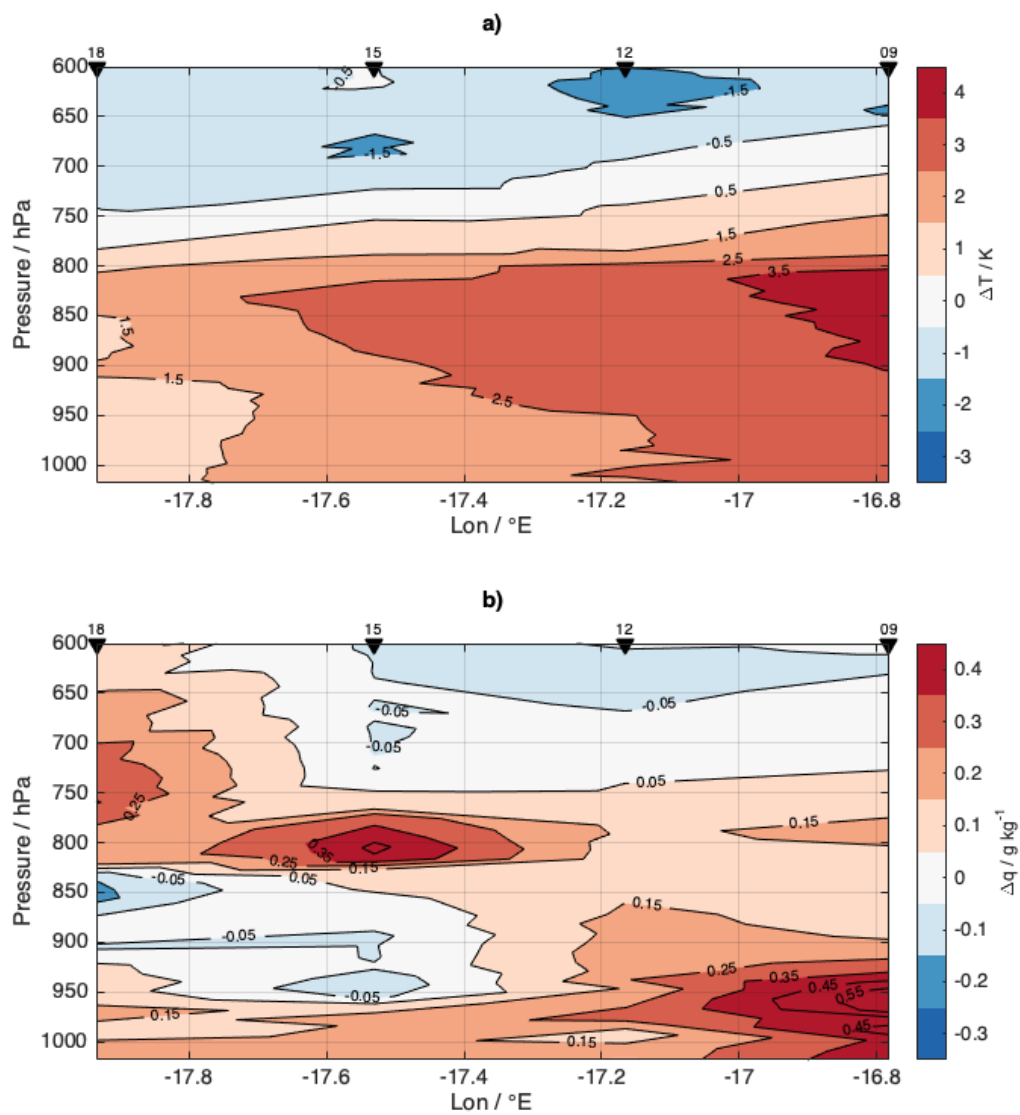
Figure D.3: Cross-section of the a) temperature bias and b) specific humidity bias between model run 0200 (fine resolution) and radiosondes. Positive values are found where the model indicates a warmer/moister field than observed by radiosondes.
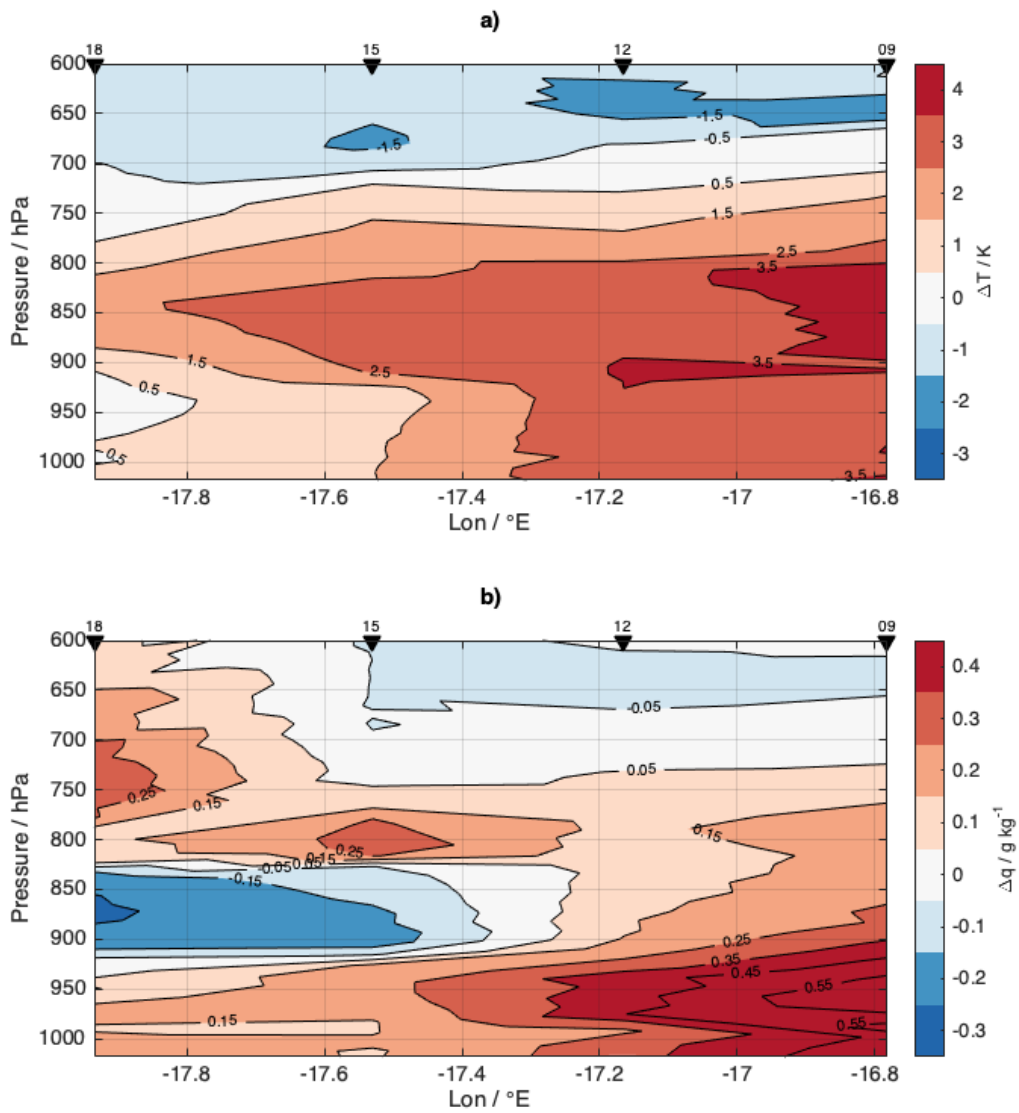
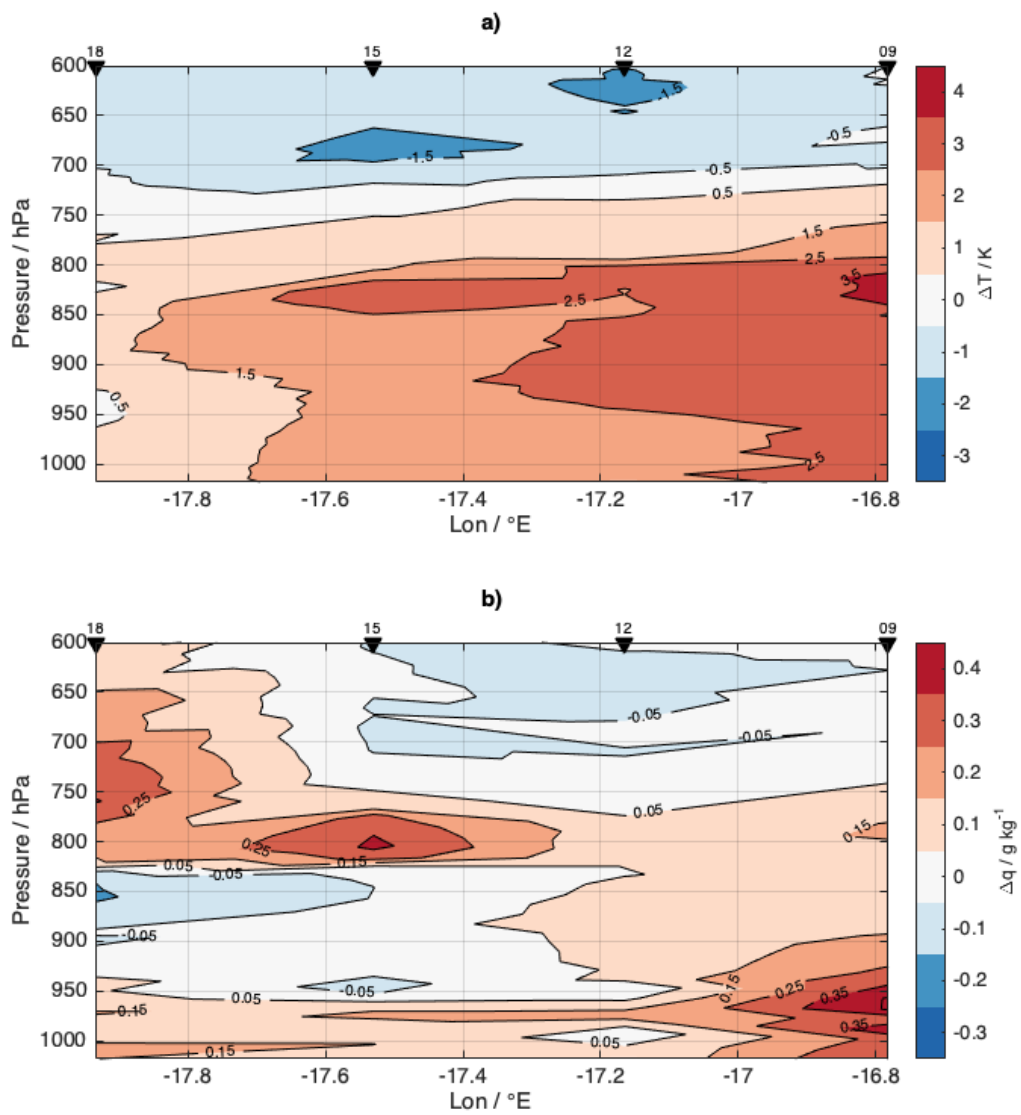Figure D.4: As Figure D.3, but for run 0200c.
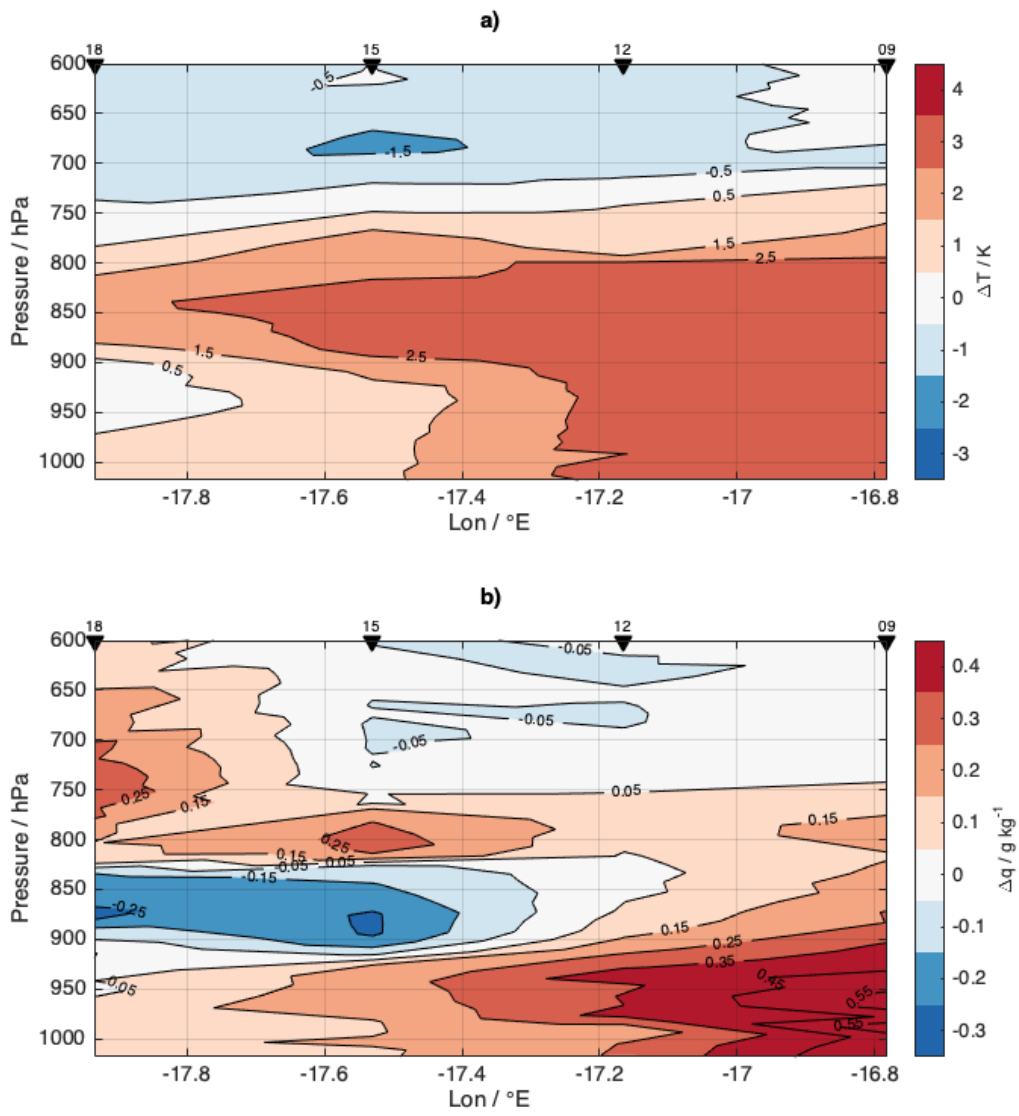
Figure D.5: As Figure D.3, but for run 0300.

Figure D.6: As Figure D.3, but for run 0300c

References

BAS. Airborne Atmospheric Research Capabilities of the British Antarctic Survey Twin Otter Aircraft. Technical report, British Antarctic Survey, Cambridge CB3 0ET, UK, 2015. URL www.antarctica.ac.uk.

David Bolton. The Computation of Equivalent Potential Temperature. *Monthly Weather Review*, 108(7):1046–1053, 1980. doi: 10.1175/1520-0493(1980)108¡1046:TCOEPT¿2.0.CO;2.

Fred V. Brock and Scott J. Richardson. *Meteorological measurement systems*. Oxford Univ. Press, 2001. ISBN 0198030746. URL books.google.no/books?id=Zj4_v7G6ATUC&pg.

Burghard Brümmer. Boundary-layer modification in wintertime cold-air outbreaks from the arctic sea ice. *Boundary-Layer Meteorology*, 80(1-2):109–125, 1996. ISSN 00068314. doi: 10.1007/BF00119014.

Burghard Brümmer. Roll and Cell Convection in Wintertime Arctic Cold-Air Outbreaks. *Journal of the Atmospheric Sciences*, 56(15):2613–2636, 1999. ISSN 0022-4928. doi: 10.1175/1520-0469(1999)056¡2613:RACCIW¿2.0.CO;2.

Burghard Brümmer, Birgit Rump, and Gottfried Kruspe. A cold air outbreak near Spitsbergen in springtime - Boundary-layer modification and cloud development. *Boundary-Layer Meteorology*, 61(1-2):13–46, 1992. ISSN 00068314. doi: 10.1007/BF02033993. URL https://link.springer.com/content/pdf/10.1007%2FBF02033993.pdf.

Martha W Buckley and John Marshall. Observations, inferences, and mechanisms of the Atlantic Meridional Overturning Circulation: A review. *Reviews of Geophysics*, 54:5–63, 2015. doi: 10.1002/2015RG000493.Received.

M. I. Budyko. The heat balance of the earth's surface. *Soviet Geography*, 2(4):3–13, 1961. doi: 10.1080/00385417.1961.10770761. URL https://doi.org/10.1080/00385417.1961.10770761.

Richard Davy and Igor Esau. Surface air temperature variability in global climate models. *Atmospheric Science Letters*, 15(1):13–20, 2014. ISSN 1530261X. doi: 10.1002/asl2.456. URL http://dx.doi.org/10.1088/1748-9326/9/11/114024.

Andrew D. Elvidge, Ian A. Renfrew, John C. King, Andrew Orr, Tom A. Lachlan-Cope, Mark Weeks, and Sue L. Gray. Foehn jets over the Larsen C Ice Shelf, Antarctica. *Quarterly Journal of the Royal Meteorological Society*, 141(688):698–713, 2015. ISSN 1477870X. doi: 10.1002/qj.2382.

D. Etling and R. A. Brown. Roll Vortices in the Planetary Boundary Layer: A review. *Boundary-Layer Meteorology*, pages 215–248, 1993.

Piotr J. Flatau, Robert L. Walko, and William R. Cotton. Polynomial Fits to Saturation Vapor Pressure. *Journal of Applied Meteorology*, 31:1507–1513, 1992. doi: 10.1175/1520-0450(1992)031¡1507:pftsvp¿2.0.co;2. URL https://doi.org/10.1175/1520-0450(1992)031%3C1507:PFTSVP%3E2.0.CO;2.

Jennifer K. Fletcher, Shannon Mason, and Christian Jako. A climatology of clouds in marine cold air outbreaks in both hemispheres. *Journal of Climate*, 29(18):6677–6692, 2016. ISSN 08948755. doi: 10.1175/JCLI-D-15-0783.1.

Jörg Hartmann, Christoph Kottmeier, and Siegfried Raasch. Roll Vortices and Boundary-Layer Development during a Cold Air Outbreak. *Boundary-Layer Meteorology*, 84(1):45–65, 1997. ISSN 0006-8314. doi: 10.1023/A:1000392931768. URL http://link.springer.com/10.1023/A:1000392931768.

Jörg Hartmann, Frank Albers, Stefania Argentini, Axel Bochert, Ubaldo Bonafé, Wolfgang Cohrs, Alessandro Conidi, Dietmar Freese, Teodoro Georgiadis, Alessandro Ippoliti, Lars Kaleschke, Christof Lüpkes, Uwe Maixner, Giangiuseppe Mastrantonio, Fabrizio Ravegnani, Andreas Reuter, Giuliano Trivellone, and Angelo Viola. Reports on Polar Research, Arctic Radiation and

Turbulence Interaction Study (ARTIST). Technical report, Alfred-Wegener Institute for Polar- and ocean science, 1999. URL `https://epic.awi.de/id/eprint/1226/1/Har1999c.pdf`.

IMO. Icelandic Met Office: Index of /kort/harmonie-igb/2018/03, 2018. URL `http://brunnur.vedur.is/kort/harmonie-igb/2018/03/`.

Erik W. Kolstad. Higher ocean wind speeds during marine cold air outbreaks. *Quarterly Journal of the Royal Meteorological Society*, 143(706):2084–2092, 2017. ISSN 1477870X. doi: 10.1002/qj.3068.

Erik W. Kolstad, Thomas J. Bracegirdle, and Ivar A Seierstad. Marine cold-air outbreaks in the North Atlantic: Temporal distribution and associations with large-scale atmospheric circulation. *Climate Dynamics*, 33(2-3):187–197, 2009. ISSN 09307575. doi: 10.1007/s00382-008-0431-5.

A.Q. Liu, G.W.K. Moore, K. Tsuboki, and I.a. Renfrew. A high-resolution simulation of convective roll clouds during a cold-air outbreak. *Geophysical Research Letters*, 31(L03101):1–4, 2004. ISSN 0094-8276. doi: 10.1029/2003GL018530. URL `http://www.agu.org/journals/gl/gl0403/2003GL018530/index.html`.

S. Nagabhushana and L. K. Sudha. *Aircraft instrumentation and systems*. I.K. International Pub. House, 2010. ISBN 9380578350. URL `https://books.google.no/books?id=zwmJI0I3qCMC&pg=PA44&lpg=PA44&dq#v=onepage&q&f=false`.

Lukas Papritz and Thomas Spengler. A Lagrangian climatology of wintertime cold air outbreaks in the Irminger and Nordic Seas and their role in shaping air-sea heat fluxes. *Journal of Climate*, 30(8):2717–2737, 2017. ISSN 08948755. doi: 10.1175/JCLI-D-16-0605.1.

Alexandre Pezza, Katherine Sadler, Petteri Uotila, Timo Vihma, D. S. Michel Mesquita, and Phil Reid. Southern Hemisphere strong polar mesoscale cyclones in high-resolution datasets. *Climate Dynamics*, 47:1647–1660, 2015. doi: 10.1007/s00382-015-2925-2. URL `http://www.mmm.ucar.edu/rt/`.

S Pfahl, H Wernli, and K Yoshimura. The isotopic composition of precipitation from a winter storm-a case study with the limited-area model COSMO iso. *Atmos. Chem. Phys*, 12:1629–1648, 2012. doi: 10.5194/acp-12-1629-2012. URL `www.atmos-chem-phys.net/12/1629/2012/`.

Ian Renfrew, R. S. Pickart, Kjetil Våge, and G.W.K. Moore. The Iceland Greenland Seas Project. *BAMS*, 2019.

Ian A. Renfrew and G. W. K. Moore. An Extreme Cold-Air Outbreak over the Labrador Sea: Roll Vortices and Air–Sea Interaction. *Monthly Weather Review*, 127(10):2379–2394, 1999. ISSN 0027-0644. doi: 10.1175/1520-0493(1999)127¡2379:AECAOO¿2.0.CO;2.

J Steppeler, G Doms, U Schättler, H W Bitzer, A Gassmann, U Damrath, and G Gregoric. Meso-gamma scale forecasts using the nonhydrostatic model LM. *Meteorol Atmos Phys*, 82:75–96, 2003. doi: 10.1007/s00703-001-0592-9.

Roland B Stull. *An Introduction to Boundary Layer Meteorology*. Springer Netherlands, Dordrecht, 1988. ISBN 978-90-277-2769-5. doi: 10.1007/978-94-009-3027-8.

G. J. van Oldenborgh, Magdalena A Balmaseda, Laura Ferranti, Timothy N Stockdale, and David L T Anderson. Evaluation of atmospheric fields from the ECMWF seasonal forecasts over a 15-year period. *Journal of Climate*, 18(23):3250–3269, 2005. ISSN 08948755. doi: 10.1175/J-CLI9008.1. URL `http://climexp.knmi.nl`.

Chris Veness. Calculate distance and bearing between two Latitude/Longitude points using haversine formula, 2019. URL `https://www.movable-type.co.uk/scripts/latlong.html`.

Ulrike Wacker, K. V. Jayaraman Potty, Christof Lüpkes, Jörg Hartmann, and Matthias Raschendorfer. A case study on a polar cold air outbreak over fram strait using a mesoscale weather prediction model. *Boundary-Layer Meteorology*, 117(2):301–336, 2005. ISSN 00068314. doi: 10.1007/s10546-005-2189-1.

Thomas T. Warner. *Numerical weather and climate prediction.* Cambridge University Press, Cambridge, 2011. ISBN 9780511763243. doi: 10.1017/CBO9780511763243.

Manfred. Wendisch and Jean-Louis. Brenguier. *Airborne measurements for environmental research : methods and instruments.* Wiley, 2013. ISBN 3527653236. URL https://books.google.no/books?id=tHdwhn-c5mgC&pg=PT67&lpg=PT67&dq#v=onepage&q&f=false.

Yiongbiao Weng and Harald Sodemann. IGP campaign 2018: Data report for ship measurements. Technical report, University of Bergen, 2019.

Martin Werner, Petra M. Langebroek, Tim Carlsen, Marcus Herold, and Gerrit Lohmann. Stable water isotopes in the ECHAM5 general circulation model: Toward high-resolution isotope modeling on a global scale. *Journal of Geophysical Research Atmospheres*, 116(15):1–14, 2011. ISSN 01480227. doi: 10.1029/2011JD015681.

Giuseppe Zappa, Len Shaffrey, and Kevin Hodges. Can Polar Lows be Objectively Identified and Tracked in the ECMWF Operational Analysis and the ERA-Interim Reanalysis? *Monthly Weather Review*, 142:2596–2608, 2014. doi: 10.1175/MWR-D-14-00064.1. URL http://polarlow.met.no/STARS-DAT/.